Metal Nanostructures : Electrochemical and Photonic Properties

Fabio Munini, B.Sc.

A thesis submitted for the Masters Degree of Sciences

Supervisor: Prof. Robert J. Forster

School of Chemical Sciences
Dublin City University

2006

I hereby certify that this material, which I now submit for assessment on the programme of study leading to the award of the Degree of Master of Science is entirely my own work and has not been taken from the work of others save and to the extent that such work has been cited and acknowledged within the text of my work

Signed _____ ID No 54148847

Date _____

Abstract

The aim of the work is to fabricate nanoporous gold electrodes of controllable structure and texture These nanostructures were created by self-assembling colloidal polystyrene latex nanospheres into closed-packed arrays on a fluorine-doped thin oxide glass surface, followed by electrodeposition of gold within the interstitial voids and finally removing the template The nanospheres diameters were 240, 430, 600 and 820 nm Dip-coating technique was exploited to create ordered arrays Latex polystyrene opals were produced by slowly withdrawing hydrophilic FTO glass slides from a 2-10% (w/w) nanospheres suspensions with feedrate and acceleration ranging from 0 001 to 0 006 mm s^{1} and from 0 003 to 0 018 mm s^{-2}, respectively Electrochemical reduction of metal complex ions, obtained from Techni Gold 25 plating bath and $NaAuCl_4$ solutions, was performed by applying an overpotential between -0 1 and -1 0 V with respect to a Ag/AgCl reference electrode The final material, a photonic crystal with an inverse opal morphology arranged in a multidomain (polycrystalline) structure with the domain size between 10^2 and 10^3 μm^2 The nanoporous gold electrodes were found to have a surface area at least 2 orders of magnitude greater than the flat metal surfaces, corroborating the possibility of being applied for electrocatalysis Furthermore, preliminary investigation using *trans*-1,2-two (4-pyridyl) ethylene (BPE) as test molecule lead to significant SERS response of these nanostructures, confirming their potential use for Raman-based sensing applications

Acknowledgements

I would like to thank my supervisors, Prof Robert Forster and Dr Johan Hjelm for all the help and advice they have given me, Eoin Sheridan for the essential support, Dr Ondrej Stranik for his assistance with dip-coating and Dr Henry Barry for the help he gave with the transmission measurements

This thesis is dedicated to Ylenia

TABLE OF CONTENTS

CHAPTER 1 – LITERATURE SURVEY

CHAPTER 2 – EXPERIMENTAL SECTION

CHAPTER 3 – RESULTS AND CONCLUSIONS

1.1 Introduction

The amazing field of nanotechnology is growing impressively fast.[1] The range of scientific knowledge is increasing dramatically day by day in terms of understanding and gaining control over fundamental building. An enormous amount of structural and functional materials, both inorganic and organic, have been created with potentially useful applications in novel devices.[2-3] Nowadays, mechanical, catalytic, electrical, magnetic, optical, and electronic functions of these structures can be finely tuned.[4-5] There are many nontrivial issues regarding how to skilfully manipulate nanoparticles and assemble periodically ordered particulate materials for application into devices based on the special physical properties that arise due to the nanometre crystallite sizes. The so-called self-assembly method represents a powerful biomimetic approach for achieving self-aggregation and organization of building blocks and involves enthalpy driven processes. The aim is to fit nanometric units together into a useful one-, two- or three-dimensional form. Ordered assemblies of nanometre-sized particles are materials providing exceptional and peculiar potentials to produce one-, two- and three-dimensional structures for a wide variety of applications ranging from photonics to memory devices, two-dimensional arrays of magnetic nanoparticles, or single-electron microelectronic devices, amongst others.[6-7] The core of nanoengeneering consists in identifying and manipulating the main growth and ordering parameters involved both during and after the process of self-assembly in order to minimize distortion and defects presence. The essential challenge is the translation of the theoretical knowledge and modelling into consistent reproducible experiments. The turning point coincides with the discovery and implementation of powerful microscopic techniques like Atomic Force Microscopy (AFM) and Scanning Tunnelling Microscope (STM), among others, and the improvement of the electron microscopy tools. STM allows to scientists to investigate in detail the self-organization processes by visualizing nanoscopic matter at atomic scale. Another essential breakthrough has been achieved by inventing AFM.[8] Because its operation does not require a current between the sample surface and the tip, the AFM can move into potential regions inaccessible to the STM or image fragile samples which would be damaged irreparably by the STM tunnelling current. Insulators, organic materials, biological macromolecules, polymers, ceramics and glasses are some of the many materials which can be imaged in different environments, such as liquids, vacuum, and low temperatures.

Self-assembly methods can be divided into two groups the so-called "top-down" and "bottom-up" approaches [9 10] In the "top down" methods, the pursued features are tailored directly on a substrate, for example, by electron beams, and then by applying appropriate etching protocol and deposition processes According to the "bottom-up" approach, nanoscopic units (molecules or atoms) are obtained from liquid, solid, or gaseous precursors using either chemical or physical deposition processes that are integrated into building blocks within the final material structure The method couples supramolecular chemistry and biomimetic processes to template synthesis

1.2 Scope of the thesis

Photonic crystals[a] can be considered just as a subclass of the group of material systems called metamaterials in which the properties mainly derive from the structure rather than from the material itself. Opals have been regarded as photonic bandgap materials only in the very recent years and have received a strong thrust because of their usefulness as scaffoldings for further templating other materials with photonic applications. The complicated route from materials to devices might be justified by their easy and cheap fabrication.

Photonic crystals are very attractive materials because of their technological application and potentiality in photonics, optoelectronics, data storage, chemical sensors, tissue engineering, etc.

This work exploits the "bottom-up" approach to produce nanoporous gold electrodes by self-assembling of colloidal nanospheres into closed-packed arrays, subsequently electrodepositing gold (electrochemical reduction of metal complex ions) within the interstitial voids and removing the template.

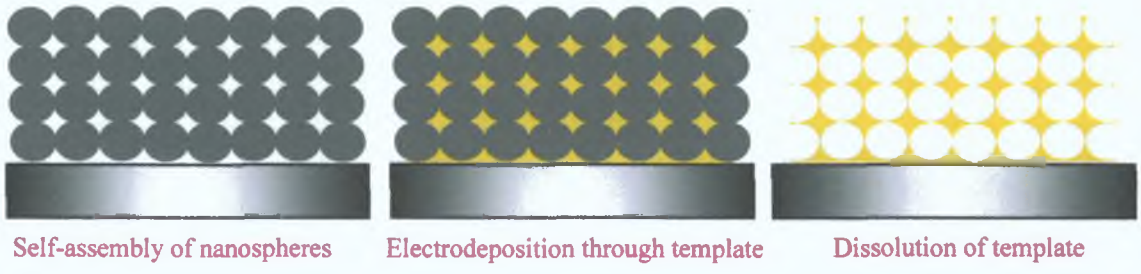

Diagram 1.1 Steps involved in the fabrication of nanoporous gold electrodes

The final material, a photonic crystal with an inverse opal morphology, is a potentially useful substrate since, thanks to the possibility to confine surface plasmons in its cavities, it could be used as platform for biodiagnostics (e.g. single molecule detection) exploiting SERS of adsorbates as well as for electrocatalytic processes. Dip-coating and electrochemical deposition are the techniques chosen for self-assembly and metal deposition processes respectively. Although traditional microfabrication techniques (ion

[a] Opal and photonic crystal are the terms used to define a 3D closed-packed well-ordered structure possessing a periodic dielectric constant with a length scale of the same order as the wavelength of the interacting electromagnetic radiation; an inverse opal is the 3D framework resulting from the dissolution of the template

beam, electron beam and microsphere lithography, photolithography, etc) allow a good control over structured defects, they are very time-consuming, complex, and expensive and have trouble in making 3D structures The self-assembly approach, on contrast, is suitable for creating 3D periodic structures in a controllable, simple and inexpensive way Therefore, in the past few years remarkable advances have been accomplished in using self-assembly methods to create 3D photonic crystals

Electrochemical deposition has a number of significant advantages in this application In fact it is a low cost approach and gives a high density of deposited material with no shrinkage of the material when the template is removed It can also be used to prepare a wide range of materials, and it allows fine control over the thickness of the final macroporous film through control of the total charge passed to deposit the film In this project, templated electrochemical deposition through arrays of polystyrene spheres is utilized to fabricate gold films of controlled structure The optical physico-chemical properties, including SERS phenomena, are then reported

In summary, photonic metal films are prepared in the following way

1 self-assembled by dip-coating onto a glass surface coated with Fluorine-doped thin oxide
2 electrochemical reduction of gold complex ions dissolved in aqueous solution within the interstitial spaces between polystyrene latex spheres
3 removal of the template

This simple and versatile approach can be extended to a wide variety of metals (Au, Pt, Co, Pd) and polymers and can be calibrated so that control of the total charge passed allows deposition to a precise thickness The resulting mesh reflects the order of the self-assembled template, allowing convenient control of the pore diameters and local crystalline order

1.3 Self-organization of nanoparticles into superlattice

Dutta and Hofmann[11] have recently published a detailed review on self-organization of colloidal nanoparticles Polystyrene (PS) nanospheres are commercially available and have been used extensively for a wide variety of applications ranging from applications in fields of photonics, nanotechnology to life science and fundamental studies in the behaviour of colloidal suspensions All of these fields arise from a common principle the adsorption of the particles on a surface, where, depending on the specific purpose, close-packed ordered arrays or less densely packed layers are selectively used The procedures reported so far for patterning PS particles range from physical concepts, such as micro-molding in capillaries (MIMIC) and electrophoresis, to hybrid approaches combining physical interaction mechanisms such as electrostatic or capillary forces with the selectivity of chemically patterned surfaces

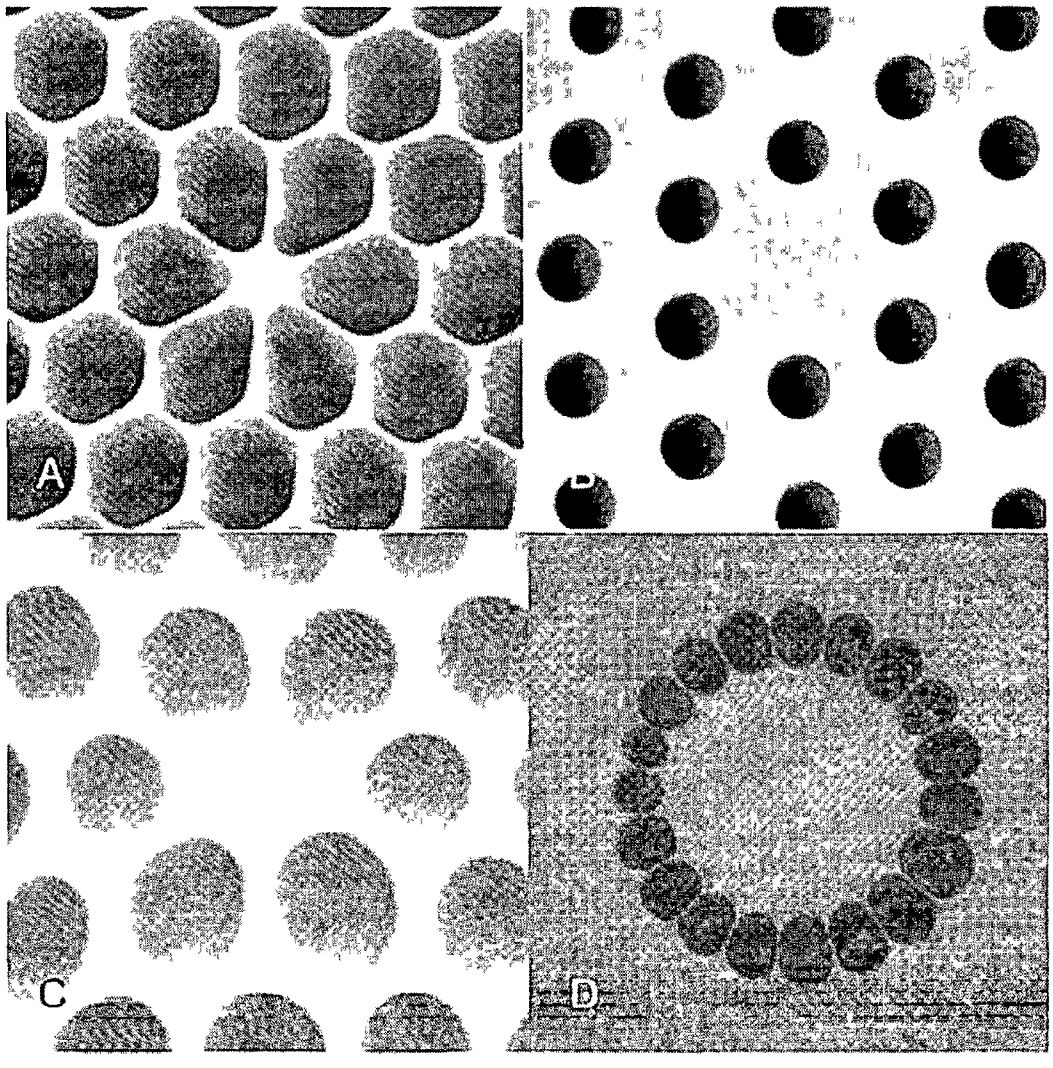

Fig 1 2 Examples of photonic crystals A) hexagonal nanochannels B) cylindric tunnels C) spheric nanocavities D) nanoring of ellipsoids

Up to now, two basic concepts have been reported for building three-dimensional photonic crystals. The first one is based on the traditional techniques that have been applied in the processing of semiconductors while the second approach exploits the self-assembly of nano- or microsized units. A widely used self-assembly technique for fabricating colloidal crystals is the gravity sedimentation of colloids from dispersions. In this way thick opals can be produced, adapted and functionalized in different ways depending on the specific objective. Self-assembly of colloidal nanospheres represents a simple and inexpensive route to three-dimensional photonic crystals. Various methods for the fabrication of colloidal photonic crystals have been reported.[12-18]

The main self-organization techniques that have been used to build two- or three-dimensional ordered structures are schematically represented in the following diagram:

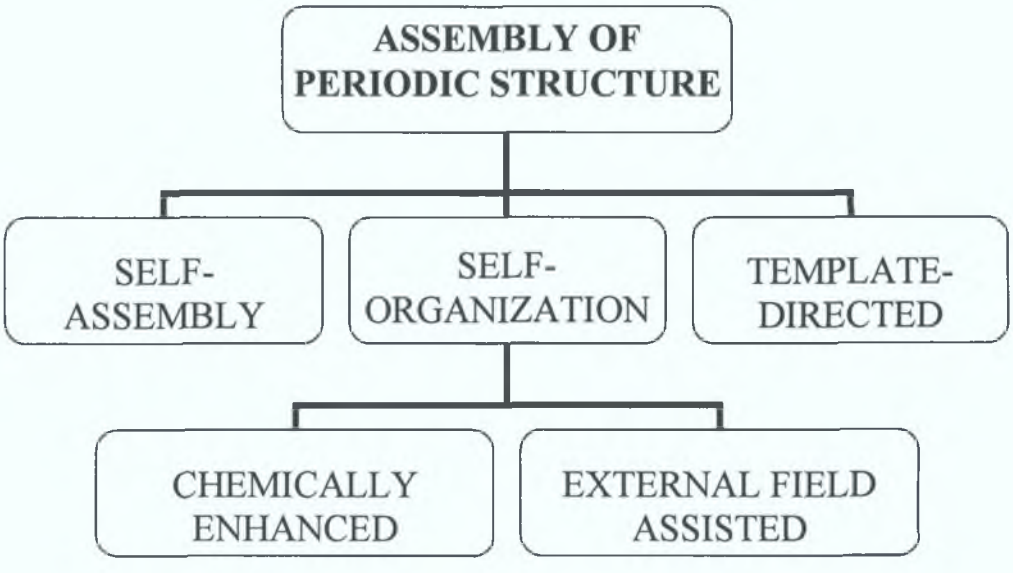

Diagram 1.3 Scheme of various self-organization techniques

Particular efforts have been made to minimize the presence of intrinsic defects such as dislocations and cracks to achieve perfect and large-scale colloidal crystals.

Novel device applications of photonic crystals, such as low-loss waveguides[19-20], optical cavities[21], zero-threshold microlasers[22], light-emitting diodes[23], optical switches[24], all-optical transistors[25], and tunable filters[26] all require an exact placement of well-defined defects in the interior of the photonic crystals. Therefore, defect engineering for self-assembled photonic crystals has been of great research interest in the last few years. In

addition, photonic crystal heterostructures[b] with multiple photonic bandgaps[c] provide the potential of controlling and modulating the flow of light more elaborately Template-directed self-assembly of colloidal spheres has been widely used to produce size-controlled colloidal clusters, oriented colloidal crystals and photonic crystal heterostructures Most of these template patterns are defined on a flat solid substrate using lithography techniques Strong capillary forces at a meniscus between a substrate and a colloidal sol can induce crystallization of spheres into a 3D array of controllable thickness If this meniscus is slowly swept across a vertically placed substrate by solvent evaporation, thin planar opals can be deposited While the normal vertical deposition method (or convective self-assembly) is believed to be limited to spheres with diameters < 0 4 μm because of the competition between the solvent evaporation and the sphere sedimentation, the dip-coating in principle is not size-limited, although the number of intrinsic defects increases with decreasing particle diameter

Several research groups have upgraded the original protocol with important modifications [27 35] Mechanical agitation by controlled gentle stirring was utilized successfully by Ozin and co-workers[36] for crystallization of large silica spheres within surface relief patterns in optical microchips However, it was impossible to fabricate continuous colloidal crystal films since the turbulence created by stirring perturbs the meniscus and impedes successful growth of continuous colloidal arrays Once a convective flow is added to the deposition process, it is possible to obtain colloidal crystals (50-100 μm^2) consisting of large-sized silica spheres (up to 1 μm) The required conditions, such as the temperature control, turned out to be very critical for opal film preparation from unstable suspensions A creative way to growing opal films in a confinement cell has been developed by Xia[37] and co-workers the cell consists of two glass slides separated by a lithographically defined resist in the shape of a rectangular frame with draining channels Figure 1 4 displays the bi-capillary deposition method inventing by Li and co-workers[38], Nagayama and co-workers[39 40] have used a method using capillary forces to assemble monolayer colloidal films

[b] A photonic crystal heterostructure is a pattern fabricated assembling different spherical units, i e spheres of different sizes or made by distinct materials or functions (i e liquid crystals or luminescent guests the resulting materials have been exploited to produce optical filters and mirrors

[c] The concept of photonic bandgap, proposed in 1987 by Yablonovitch, refers to the forbidden range of energies resulting from scattering and interference phenomena caused by photonic propagation trough a periodic dielectric, to the bandgap in a semiconductor yield by Bragg-like diffraction of propagating electrons

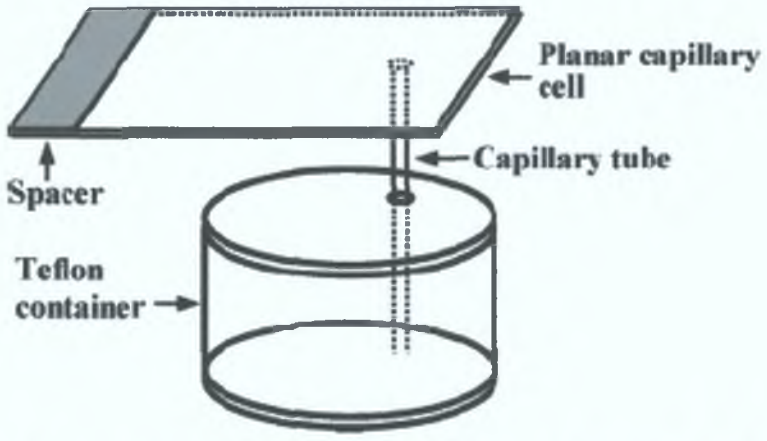

Fig. 1.4 Setup for bi-capillary deposition invented by Li et al.

Figure 1.5 displays an approach re-elaborated by Colvin and co-workers[41] to produce colloidal crystal multi-layers using a vertical deposition technique, demonstrating the applicability of vertical deposition to fabricate high-quality single-crystal colloidal crystals with controlled thickness. Although this is the most common method, nevertheless it is very time-consuming as it is based on decreasing the evaporation rate.

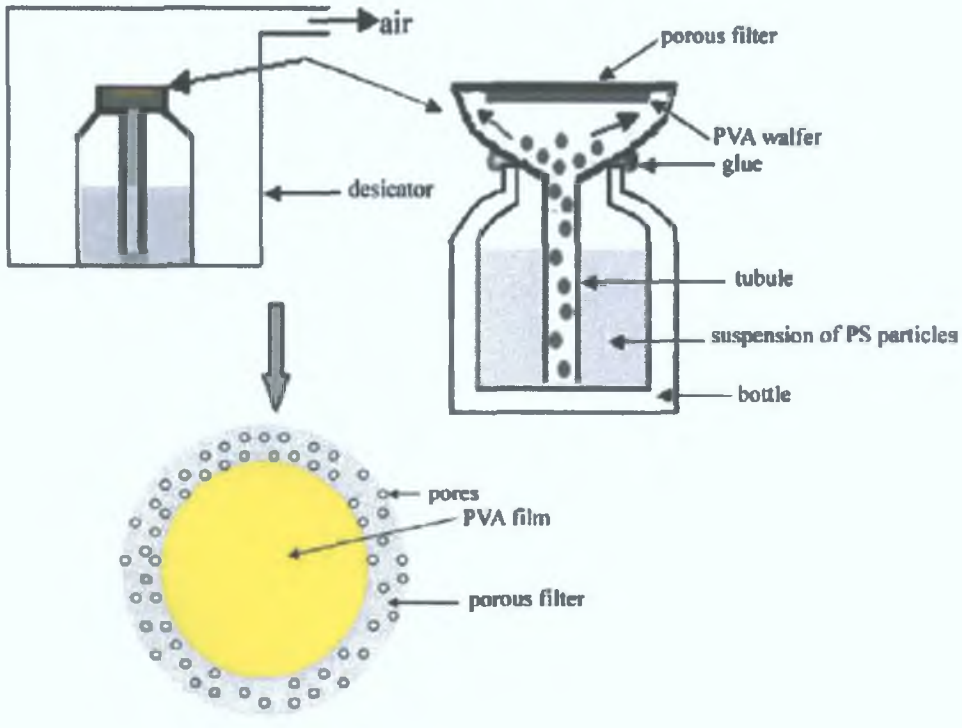

Fig. 1.5 Schematic diagram of the vertical deposition method (usually the setup is placed in a temperature- and humidity-controlled chamber to decrease the solvent evaporation rate)

Ye et al.[42] have deeply analyzed the effects of evaporation temperature on the texture. However, the vertical deposition method for photonic crystals fabrication still needs to be fully optimized and the effect exerted by all the different parameters has to be better understood and controlled. Kuai et al.[43] have grown photonic crystals on glass microslides placed vertically into a vial containing diluted aqueous dispersion of polystyrene spheres in a temperature- and humidity-controlled chamber. Most of these methods, involving planar solvent diffusion and evaporation, are severely influenced by the presence of both linear and curved crack fronts.

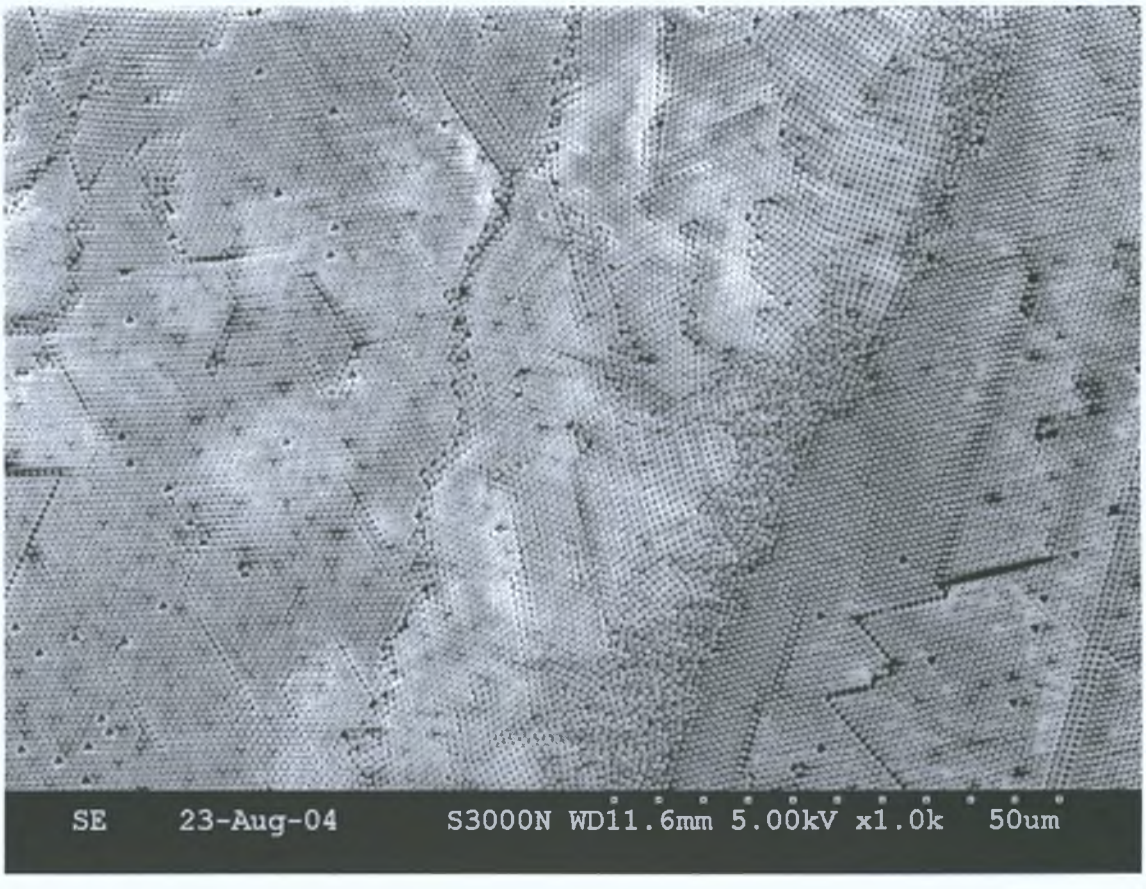

Fig. 1.6 Linear and curved crack fronts

The resulting samples therefore do not exhibit an homogeneous thickness as the drying front of the suspension moves from the inner part of the cell toward the boundaries originating a sedimentation gradient. For this reason a vertical deposition method, in which almost all the cracking fronts propagate linearly, has been chosen for this project as it allows greater control of the film thickness and fabrication of sample with homogeneous texture and morphology.

1.4 Self-Organization Through Capillary Forces

Figure 1 7 summarizes various types of capillary forces acting on particles, reviewed by Kralchevsky and Denkov[39 44] *Normal capillary forces* are orthogonal to the contact line and originated either by liquid-in-gas or by gas-in-liquid capillary bridges, particle-particle and particle-wall interactions are involved Instead the *lateral capillary forces* are parallel to the contact line the interaction arises from the overlap of interfacial deformations created by the separate particles In the case of *flotation force*, originated by the particle weight and buoyancy (including the Archimedes force) the deformations are due to the particle weight In the case of *immersion forces* the deformations are influenced by the wetting properties of the particle surface position and shape of the contact line and magnitude of the contact angle *Capillary charges* must be taken into account when the deformation around an isolated particle is asymmetric, and cases of infinite and finite menisci can be discriminated The forces between particles of irregular contact line can be considered as interactions between *capillary multipoles*, in analogy with electrostatics

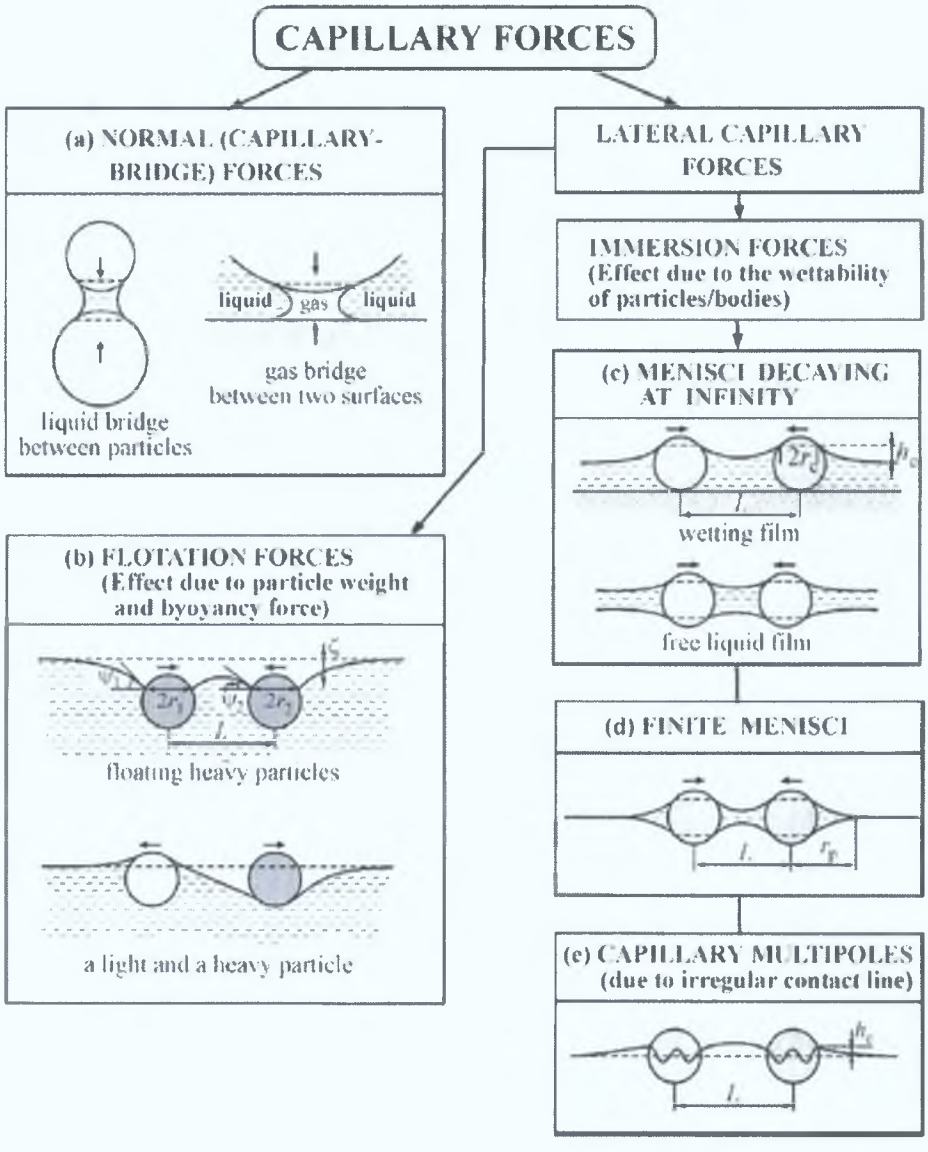

Fig. 1.7 **(a)** The *normal* capillary forces can be due to either liquid-in-gas or gas in-liquid capillary bridges, which lead to particle-particle and particle-wall interactions; the force is directed normally to the contact line. In the case of *lateral* capillary forces **(b,c,d,e)** the force is parallel to the contact line; the interaction is due to the overlap of interfacial deformations created by the separate particles. **(b)** In the case of *flotation* force the deformations are caused by the particle weight and buoyancy. In the case of *immersion* forces **(c,d,e)** the deformations are related to the wetting properties of the particle surface: position and shape of the contact line and magnitude of the contact angle. When the deformation around an isolated particle is axisymmetric, we deal with "*capillary charges*"; one can distinguish cases of infinite **(c)** and finite **(d)** menisci, **(e)** The forces between particles of undulated or irregular contact line can be described as interactions between "*capillary multipoles*", in analogy with electrostatics.

P. A. Kralchevsky and N. D. Denkov, *Curr. Opin. Coll. Inter. Sci.*, 6, 383(2001). © 2001, Elsevier Science.

If a droplet of the colloid suspension is dried slowly on an extremely flat, unpatterned, polar surface (atomic flatness <0.3 nm, such as silica), the particles aggregate at the rim of the droplet because of attractive capillary interparticle forces involved when the water film thickness is in the range of the particle diameter. The particles, electrostatically attached, are immobilized after complete drying, suggesting a three-step mechanism for the particle adsorption: the first stage, governed by charge and polar interactions, consists in the positioning and adhesion of the particles on the surface. The second step involves interparticle capillary forces, which generate lateral displacement of the particles during drying. At last, when the evaporation process is over, an irreversible reorganization of the particle–substrate interface follows, which prevents resuspension or displacement when resubmerging the assembly into the adsorption liquid. Since the Coulomb repulsion of the like-charged particles prevents dense packing in the aqueous medium, a submonolayer coverage of electrostatically adsorbed particles forms on the charged pattern surface in the bulk phase of the suspension. While the suspension evaporates, the liquid front recedes very slowly over the adsorbed particle layer, and a thin liquid meniscus remains over the particle assembly generating interparticle attractive capillary forces. Due to the slow withdrawal of the droplet front, particles from the suspension have enough time to migrate into the thin liquid film at the drying front and aggregate into multilayer over the colloid assembly pattern driven by capillary forces. An accurate explanation should not neglect further factors affecting the size-dependent behaviour of the process, particle–surface interactions, such as surface topography and roughness or even nanoscopic air bubbles in order to completely understand and correctly analyze the ordering phenomena of colloidal nanoparticles through capillary forces. A first questionable, but interesting, attempt to rationalize and quantify the effect of particle size, based on a computer simulation reproducing the aggregation process, was carried out by Yamaki et al.[45] After the modelling stage, experiments were performed using a binary mixture of polystyrene nanospheres with different particle size. The simulated configuration of aggregating nanospheres with different diameters were strongly affected and mislead by the limitations of the model, accounting only for lateral capillary forces and convective flow without considering the remaining forces involved in the process. Figure 1.8 shows one example of predicted conformation: the neglect of all the remaining forces involved in the process originated configurations in which the bigger particles show a trend to aggregate forming a round array in the middle of the sample surrounded by the smaller particles. Very recently Reyes and Duda [46] have proposed a kinetic Monte Carlo simulation study of the

structure of colloid films during solvent evaporation. Their method is versatile and although the model is highly simplified in comparison to the experimental situation, it is able to reproduce some trends of the latex film formation. It is believed that the sophistication of the interactions between particles and the inclusion of further parameters such the effect of an intercolloid soft repulsion, an effective attraction due to a capillary force and a colloid-surface short-range interaction might dramatically improve the fit between simulated and experimental configurations.

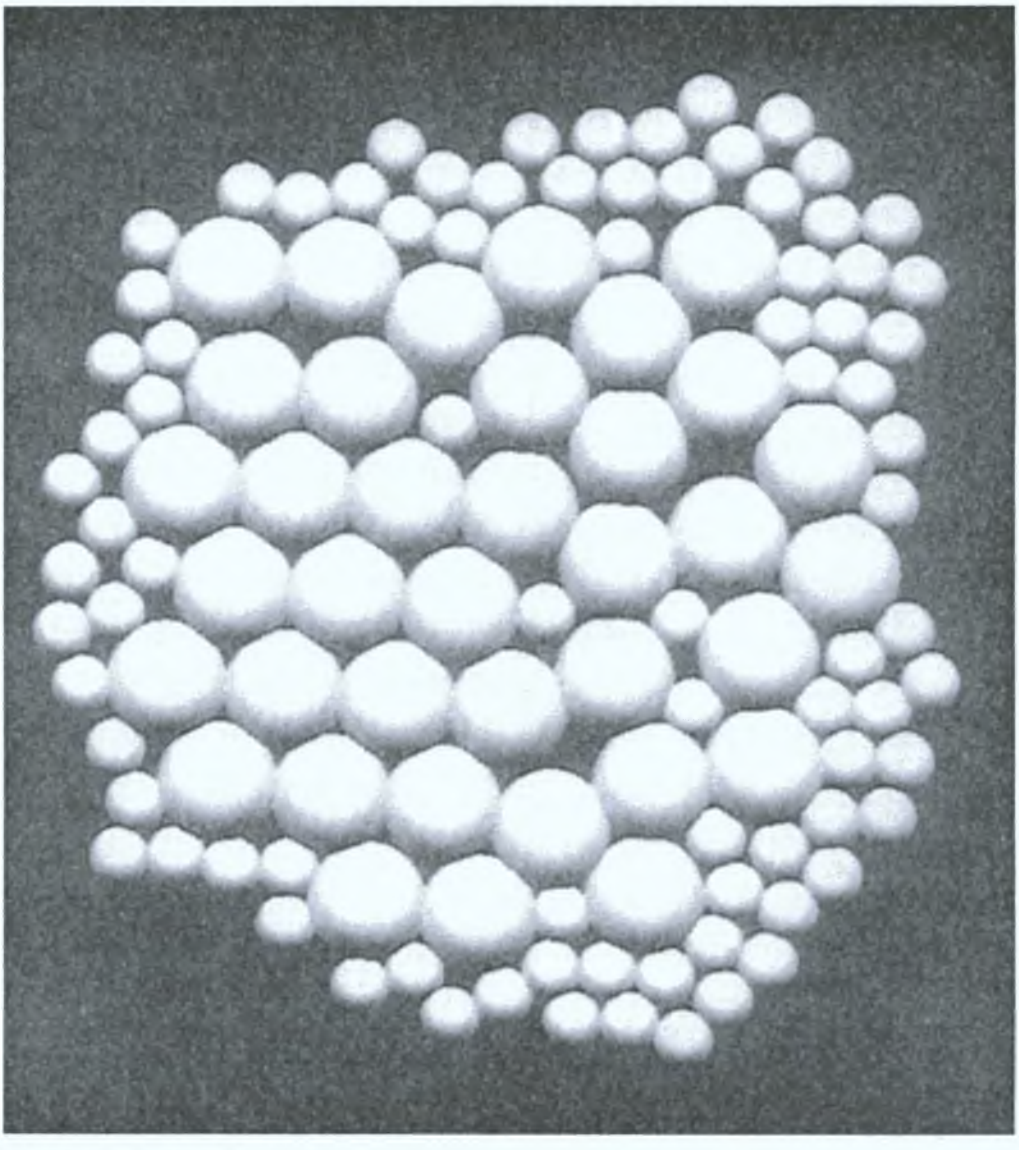

Fig. 1.8 Simulated configuration of aggregation of nanospheres with different diameters

The experimental configurations are in good agreement with the simulated ones. Furthermore, surfactant solutions exhibit a slower evaporation rate than pure water at the same conditions. The increase of the surfactant concentration leads to deposition of

many particles on the glass surface before their incorporation in the array, which causes dislocations and other defects in the crystal Probably, this is due to the adsorption of positively charged surfactant molecules on the negatively charged particle and glass surfaces, which suppresses the electrostatic repulsion between them At even higher surfactant concentrations, the particles coagulate in the bulk suspension and further water evaporation does not lead to crystallization but to random arrays

Another important factor that should be taken into account is that during the drying process, the ionic strength of the colloid changes modifying the double-layer thickness and hence the organization process The ability to form large-sized domains mainly depends on the quality of the suspension, thickness, and the stability of the wetting film on the substrate plate With high quality suspensions, which means those free from impurities with uniform particles (in terms of standard deviation having size uniformity with coefficient of variation $\leq$ 3%) larger or smaller domains can be formed by controlling either the wetting film thickness at the array's leading edge or the rate of evaporation

1.5 Cracking in Drying Latex Films

Cracking plays a key role when dealing with film drying and understanding how to prevent or at least minimize the fractures and fabricate good quality self-assemblies.

For completeness, it is useful to briefly overview the main theories and models explaining and modelling the cracking phenomena respectively. The concept of photonic crystals has become commonly used since Yablonovich[47] and John[48] conceived the idea that these materials could confine and control light and its emission. Tirumkudulu and Russel have recently reviewed the fundamental theories reported in literature concerning cracking in drying films and have then chosen and adapted the most suitable model to mimic the phenomenon specifically for latex particles.[49]

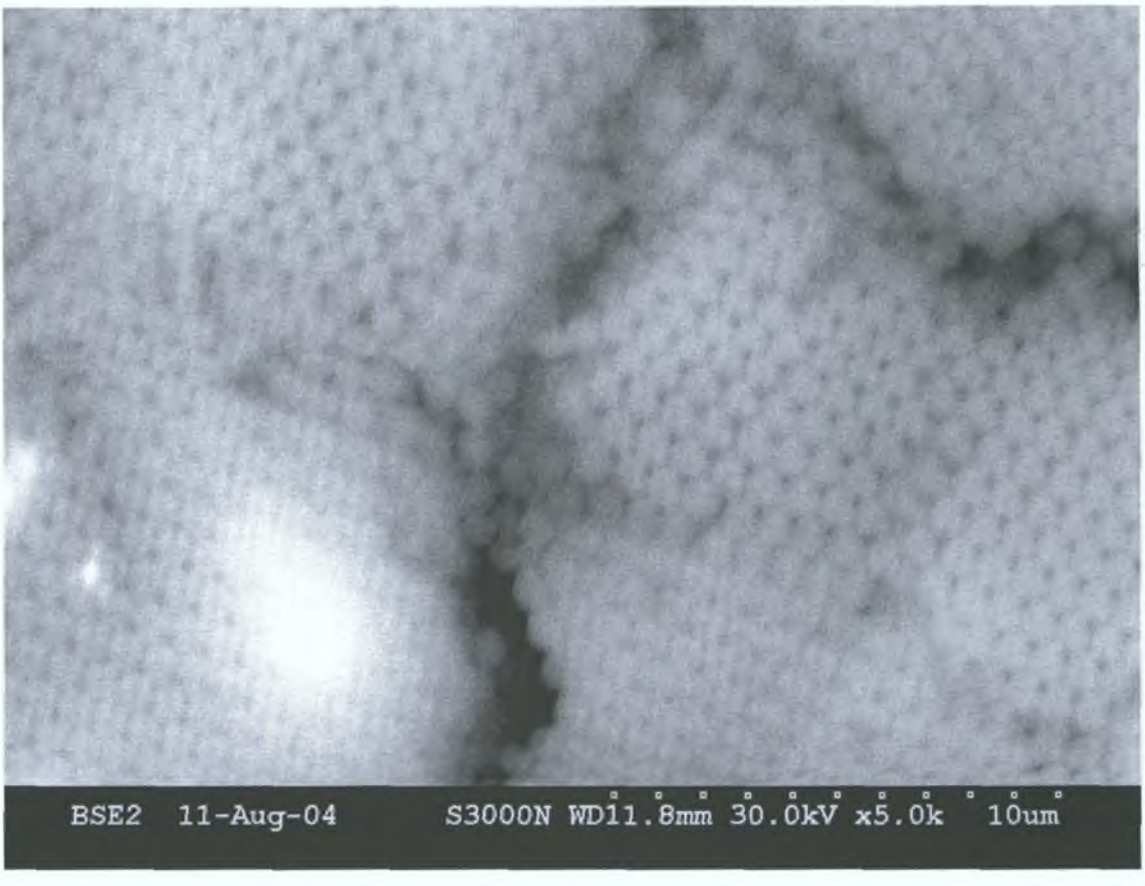

Fig. 1.9 SEM micrograph of polystyrene nanospheres film cracking

Their analysis begins by considering the earliest deformation theory for spheres in contact, proposed by Hertz in 1890,[50] which relates the change in the centre to centre distance between two touching spheres to their elastic modulus and the external force

compressing them together In contrast, the viscous sintering of two spheres, proposed by Frenkel in 1945,[51] balances the interfacial tension, which minimizes the particle surface area, against viscous forces resisting deformation, resulting in a simple relation between rate of strain, the internal viscosity of the particle, and interfacial tension The JKR theory, proposed by Johnson, Kendall and Roberts in 1971, balances the surface energy and elastic response to predict the strain as a function of the interfacial tension and the shear modulus [52] In 1975 Derjaguin, Muller and Toporov generalize the original Derjaguin model of adhesion to include tensile interactions This is the DMT theory [53] Finally, 1984 Maugis and Pollock[54] extended the JKR theory including adhesion-induced plastic deformations

To compare the foregoing models the normalized radius of the contact area $\bar{A}$ (Eq 1) force $\bar{F}$ (Eq 2) and penetration depth $\bar{h}$ (Eq 3) are introduced

$$\bar{A} = \frac{a}{\left(\frac{\pi R^2 \sigma}{K}\right)^{\frac{1}{3}}} \qquad (1)$$

$$\bar{F} = \frac{F}{\pi R \sigma} \qquad (2)$$

$$\bar{h} = \frac{h}{\left(\frac{\pi^2 R \sigma^2}{K^2}\right)^{\frac{1}{3}}} \qquad (3)$$

Where K is the effective Young's modulus, a the contact area radius, σ the work of adhesion R is the curvature radius This work has the following components

$$W_a = W_a^d + W_a^p + W_a^i + W_a^h + W_a^\pi + W_a^{da} + W_a^e \qquad (4)$$

The subscripts denote d – London dispersion interaction, p– dipole-dipole (orientation) interaction,i induction interaction, h– hydrogen bond, π π bond, da – donor-acceptor bond, e – electrostatic interaction

In Table 1 are collected major assumptions and restrictions of every theory while in Table 2 the corresponding normalized equations

Table 1.10 Comparison of quantitative adhesion models

Model	Assumptions	Restrictions
Hertz	No surface forces	Not applied to small loads in the presence of surface forces
DMT	Long-range surface forces act only outside the contact area Model geometry is as in the Hertz model	Contact area can be decreased due to the limited geometry Applied only to small λ
JKR	Short-range surface forces act only within the contact area	Force magnitude can be decreased due to surface forces Applied only to large λ
Maugis	Tip-sample interface is modelled as a ring	The solution is analytical but equations are parametric Applied to all λ values

The parameter λ determines the amount of adhesion and is defined by

$$\lambda = \frac{2.06}{\xi_0}\left(\frac{R\sigma^2}{\pi K}\right)^{\frac{1}{3}} \qquad (5)$$

where ζ_0 is the interatomic distance

Table 1.11 Normalized equations of quantitative adhesion models.

Model	Normalized equations
Hertz	$\overline{F} = \overline{A}^3$ $\overline{h} = \overline{A}^2$
DMT	$\overline{F} = \overline{A}^3 - 2$ $\overline{h} = \overline{A}^2$
JKR	$\overline{F} = \overline{A}^3 - \overline{A}\sqrt{6\overline{A}}$ $\overline{h} = \overline{A}^2 - \frac{2\sqrt{6\overline{A}}}{3}$
Maugis	$1 = \frac{\lambda \overline{A}^2}{2}\left[\sqrt{m^2-1} + \left(m^2-2\right)\arctan\sqrt{m^2-1}\right] + \frac{4\lambda\overline{A}^2}{3}\left[1 - m + \sqrt{m^2-1}\arctan\sqrt{m^2-1}\right]$ $\overline{F} = \overline{A}^3 - \lambda\overline{A}^2\left[\sqrt{m^2-1} + m^2\arctan\sqrt{m^2-1}\right]$ $\overline{h} = \overline{A}^2 - \frac{4\lambda\overline{A}}{3}\sqrt{m^2-1}$

The term m is a correction parameter introduced by Maugis.

Routh and Russel in 1999 consolidated the various theories by considering the viscoelastic deformation of a pair of particles due to both interfacial tension and external forces such as those exerted by neighbours in contact. Averaging the stress within the particles to relate the forces acting on the pair to the deformation and then averaging the force dipoles in the particle pairs they obtained a macroscopic stress-strain relation for a deforming film.[55-56] In 2001 they coupled evaporation with particle deformation and predicted the lateral front propagation in a drying film[57] (Figure 1.12). Although cracking during drying of wet films has been observed for diverse systems such as wet clays, ceramics slips, and model colloidal dispersions, the experiments of

Cima and co-workers[58-59] seem to be the most relevant for understanding the cracking propagation

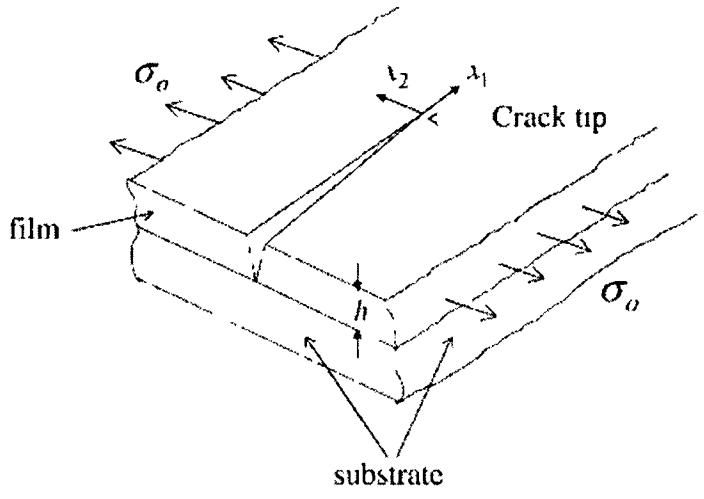

Fig 1 12 Schematic diagram of an isolated crack propagating across the film (σ_0 represents the bulk stress in the plane of the film, the coordinates x_1 and x_2 define the position of the crack tip in the plane on which the fracture is propagating, h is the film thickness)

They have reported drying and cracking phenomena in wet ceramic films prepared from electrostatically stabilized suspensions of alumina particles of 200 and 400 nm diameter in water Micrographs of drying alumina films have revealed the presence of three different domains a central super-saturated region containing the fluid dispersion, an outer dry area, and an intermediate saturated domain containing closed packed particles saturated with water (Figure 1 13A)

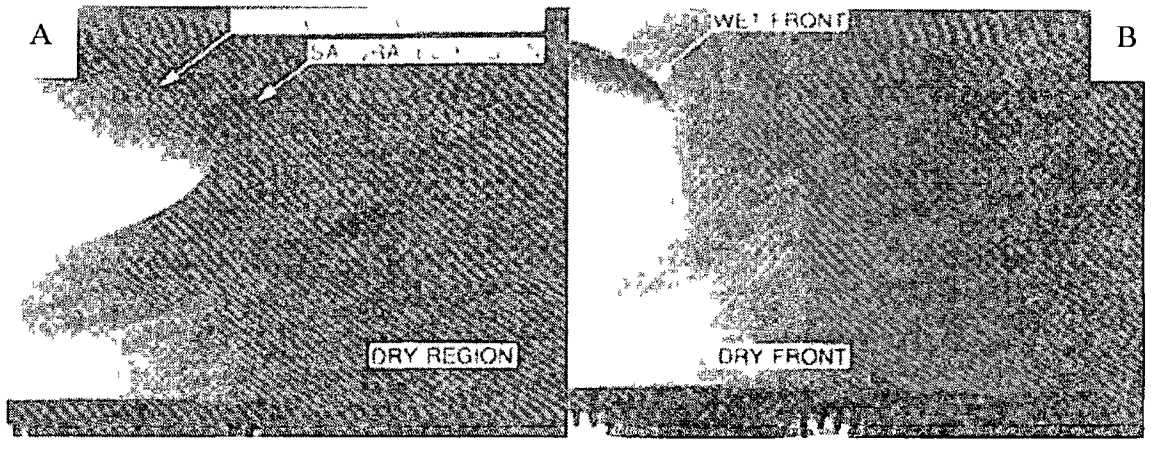

Fig. 1.13 A) domains present on drying alumina films
B) fronts separating supersaturates, saturated and dry domains

As evaporation proceeded, the "wet" and "dry" fronts, referred to the fronts separating the supersaturated and saturated domains and saturated and dry domains, advanced from all sides toward the centre of the film (Figure 1 13B) The cracks were noticed to nucleate at some distance from the edge of the film and were oriented perpendicular to the moving fronts The cracks extended into the saturated region and propagated with the moving fronts toward the centre of the film A critical cracking thickness, above which films would crack spontaneously, was determined from experiments on films of various thicknesses

Tirumkudulu and Russel, applying Griffith's criterion for equilibrium crack propagation coupled with the stress-strain relation developed by Routh and Russel for drying films, have extensively studied the stresses generated during drying and the resulting cracking phenomena for latex dispersions containing particles of varying radii The measured critical stresses and the crack spacing were compared with the predictions of Routh and Russel and a scaling for the critical stresses in good agreement with the experimental values was derived Both the measured and the predicted crack spacing were noticed to vary linearly with film height with the observed slope fitting the predicted values

1.6 Forces operating during film formation from latex dispersion

The mechanism of film formation[60 61] from latex dispersions has received widespread attention over the last years and macroscopic aspects of the drying process were monitored by NMR imaging [62] and studied using EPR techniques [63]

Scientists agree that three main forces are involved in the film formation

1 the surface tensions of polymer and water, and the van der Waals forces promote the film formation
2 a steric or Coulombic barrier of surfactants or polyelectrolytes in the particle surface layer shields the particles from having contact in the first two stages
3 polymer mobility represented in the glass transition temperature, is responsible for successful interdiffusion of polymer chains in the third stage

Dealing with particle deformation, different models have been proposed in order to predict the best conditions under which good film final properties (i e mechanical resistance, texture) could be achieved An overview of the different models has been given by Visschers et al [64], the attention is focussed on the importance each theory has attached to each specific parameter Furthermore, for the mechanical response of the particles different models have been proposed

- viscous
- purely elastic
- visco-elastic

All the authors agree on the main forces governing the film formation and responsible for particles deformation

1 Van der Waals force,
2 repulsion caused by overlap of dielectric of double layers,
3 capillary pressures,

These forces are briefly described in the following section

1.7 The Van der Waals force

Particles brought into few nanometres proximity experience an attractive force, termed Van der Waals force, which originates from fluctuations in the charge distribution of the atoms/molecule/particle. London derived an equation relating the magnitude of the force to the polarizability of the atoms, while Hamaker, assuming pair wise additivity, deduced an equation for the Van der Waals force between macroscopic bodies. Although his theory is not the most sophisticated and is only valid at small distances (<20 nm), it provides a useful approach and can be adapted taking into account the 'retardation' of interaction at larger distances.

The Van der Waals attraction force F_{attr} between two identical spheres with radius r_p is defined as:

$$F_{attr} = -\frac{A}{6r_p}\left[\frac{-4s}{(s^2-4)^2} - \frac{4}{s^3} + \frac{8}{s(s^2-4)}\right] \qquad (6)$$

where A is the so-called Hamaker constant, r_p is the radius of the spheres and s is the dimensionless distance defined as the ratio of the distance between the centres and the particle radius r_p; i.e. at contact $s = 2$.

1.8 The capillarity pressure caused by the bulk water/air interface

The drying process of a latex film consists in the partial evaporation of water from the latex dispersion first, resulting in a decrease in the average interparticle distance until the evaporation has proceeded to such an extent that the particles are constrained into a random packing. The evaporation phenomenon continues in the second stage forcing the water/air interface to recede from the surface of the film towards the particles closed-packed array front. Because of the relatively good wettability of the particle this interface becomes curved with the air on the inner side of the curvature resulting in a liquid pressure drop. The pressure difference across the water/air interface is the so-called capillary pressure. According to Brown[66], the capillarity pressure provides the main driving force for particle deformation.

This concept was developed by Mason[67] who proposed the following explanation for the capillary mechanism the capillary force exerted on the particles at the water/air interface squeezes the underlying layers of closed packed particles An expression has been derived for the resulting force, both in absence and in presence of deformation, implying more realistic assumptions than those of Mason's model The downward force experienced on the particles at the water/air interface is balanced exerting an upward force by the underlying particles on the particles at the water/air interface Assuming face centred cubic packing, each particle at the water/air interface experiences the upward net forces of three underlying particles In the absence of deformation, assuming that the meniscus remains on the particle's equatorial plane, the force balance equation for a top particle is given by the following form

$$\pi r_p^2 (P_l - P_A) - 2\pi r_p \gamma_{w/a} \cos\theta - \frac{4}{3}\pi r_p^3 (\rho_S - \rho_L) g + \sum_{i=1}^{3} F_{vertical\ i} = 0 \qquad (7)$$

where P_L is the pressure in the water phase, P_A is the ambient pressure, r_p is the particle radius, $\gamma_{w/a}$ is the water/air surface tension, θ the contact angle, ρ_s is the particles density, ρ_l is the liquid phase density and g is the gravitational acceleration

Several equations relating the interparticle distance a to the particle radius r_p have been elaborated in the last years assuming different mechanical behaviour The Johnson-Kendall-Roberts theory (JKR), derived by Hertz's equation, proposed a powerful and accurate model capable to predicted the deformation undergone by adjoining particles

In the absence of surface forces, under an applied load W the spheres deform to make contact over a circle of radius a given by Hertz's equation

$$a^3 = \frac{3}{4}\frac{WR}{E^*} \qquad (8)$$

where E^* is the *contact modulus* given by

$$1/E^* = (1-\nu_1^2)/E_1 + (1-\nu_2^2)/E_2 \qquad (9)$$

and R is the so called *equivalent radius* defined in terms of the particles radii R_1 and R_2 as $R = R_1R_2/(R_1+R_2)$

Indeed, the real film formation process is consistent with a mechanism in which both capillary and surface forces (polymer/water or polymer/air interfacial tension) are involved to promote coalescence

Johnson et al , assuming that contact over a circle of radius a introduces a surface energy $-\pi a^2 \Delta\gamma$ ($\Delta\gamma$ is the surface energy or *work of adhesion*, a function of the particles surface tension), showed that the effect of surface energy is to modify the Hertz result to

$$\frac{4E^*}{3R} = W + 3\pi R\Delta\gamma + \sqrt{6\pi R\Delta\gamma W + (3\pi R\Delta\gamma)^2} \qquad (10)$$

The majority of the models and simulations reported in literature have implemented this theory

1.9 The capillarity pressure caused by liquid bridges between particles

As shown in Figure 1 14, after the water/air interface has reached the substrate surface, some residual water will remain at the contact points between adjoining particles forming structures which will be denoted as liquid bridges

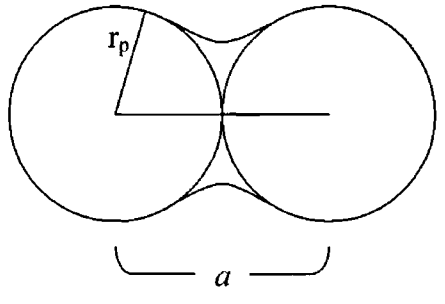

Fig 1 14 *Liquid bridge* between two particles, the interparticle distance a is a dimensionless distance defined as the ratio of the distance between the centres and the particle radius r_p of two adjoining particles

Rabinovich et al [68] have recently overviewed the theoretical formulas reported for the estimation of the capillary force due to a liquid bridge and elaborated an alternative protocol for the theoretical estimation of the capillary force between two spheres The

distant dependent capillary force can be derived theoretically on the basis of two approaches:

1. the total liquid bridge energy
2. the pressure difference across the liquid bridge

Experimental measurements of the capillary force using AFM were performed in order to validate the theoretical assumptions and estimates, leading to the implementation of the two different methods. The experimental and theoretical results were in good agreement. Most of the theoretical expressions for capillary forces that have been reported are based on the sphere/plate geometry for the interaction of the two surfaces. The prediction of the distance-dependent capillary force of adhesion is essential in estimating the total adhesion energy required to control and modify the flow behaviour of powder systems and in preventing segregation in key industrial processes, such as mixing.

1.10 Template-Assisted Self-Assembly

The approaches combining templating with attractive capillary forces represent powerful methods to assemble particles into complex aggregates with well-controlled sizes, shapes, and internal structures.[69-70]

Surface confinement provided by liquid droplets has been widely applied to assemble colloidal particles or microfabricated building blocks into 3-D structures. Patterned arrays of templates are realized in thin films of photoresists (for example, spin-coated on glass, silicon wafer, or quartz substrates), using conventional photolithography techniques belonging to microelectronics or printing processes. Templating against opaline arrays of colloidal spheres has also been successfully extended to the fabrication of 3D macroporous structures from a wide variety of materials, including organic polymers, ceramic materials, inorganic semiconductors, and metals.[71-72-73]

Peculiar remarkable features of this approach include its simplicity and fidelity in transferring the structure from the template to the replica.

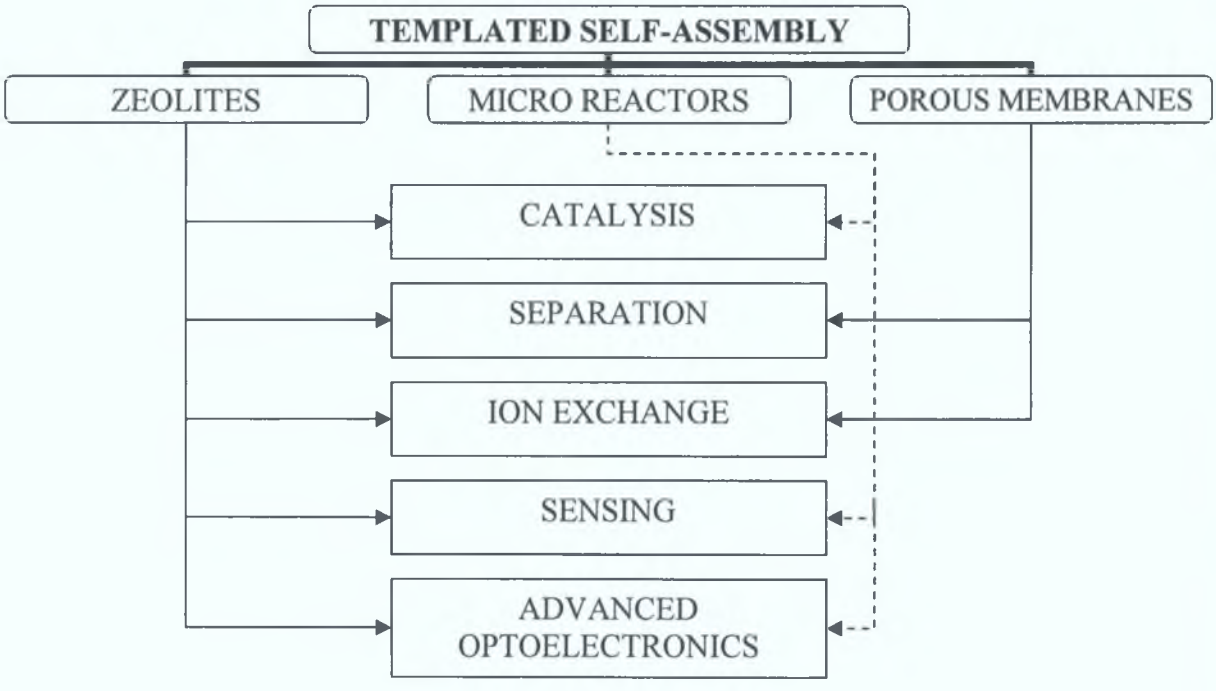

Diagram 1.15 Applications of templated self-assembly

The pores size and the periodicity of the porous structures can be precisely selected and precisely modified by changing the size of the colloidal spheres. A similar approach is extendible to other materials, the only requirement being the availability of a precursor that can infiltrate through the void interstitial spaces without significantly swelling or dissolving the template (usually made of self-organization of colloidal nanoparticles, polystyrene beads or silica spheres). Gaseous precursors have also been used in this approach as well, although their flow might be blocked by the initial product deposited on the surfaces.[74]

The smallest colloidal spheres that have been successfully utilized in this method are ~35 nm in diameter[75]. The success of this approach depends on the control of a variety of parameters like the meniscus of the curvature of the rear edge of the liquid slug, concentration, and surface charges on the colloidal particles and the templates. However, though it has not been conclusively proved yet, this method may be limited to a few tens of nanometre regions due to the interaction of the Brownian motion and the capillary forces. When an aqueous dispersion of colloidal particles is left to dry from a patterned solid surface with appropriate relief structures, the particles get trapped and aggregate forming clusters whose structures are determined by the geometric

confinement provided by the templates Using this approach, the capability and feasibility of assembling polystyrene beads and silica colloids into complex aggregates, polygonal or polyhedral, linear or branched, and circular rings, have been documented Immobilization of metal colloid particles on a suitable structured matrix using a self-assembly technique is one of the promising strategies for the construction of colloidal nanostructures Assembling a homogeneous dispersion in a well-defined 3D nanostructure offers an alternative route to these 3D structure formations Zeolites and porous membranes (like porous silicon[75], anodized alumina[77], etc) have also been used as templates for the growth of nanoparticles inside the pores

1.11 Dip-coating technique

The dip-coating is the low-cost powerful technique used in this project to transfer the nanospheres from the suspension to the substrate surface in order to fabricate opaline structures. The method consists in the slow mechanical withdrawal of a planar smooth substrate from a colloidal suspension, with rate and acceleration optimized in order to obtain an opaline structure of controlled thickness and good texture. Obviously, the substrate must be highly hydrophilic in order to attract the acqueous suspensions containing the polystyrene nanospheres.

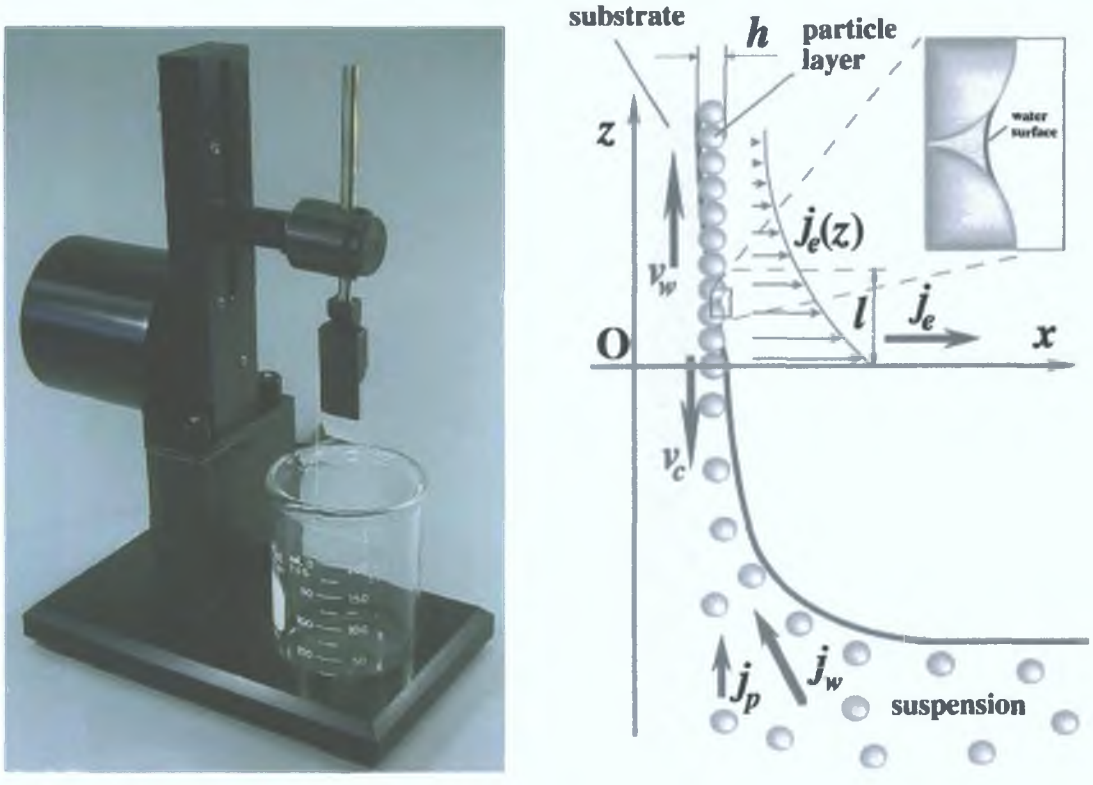

Fig. 1.16 Left. Dip-coater

Right. Scheme of the particle and water fluxes in the vicinity of monolayer particle arrays growing on a substrate plate that is being withdrawn from a suspension. The inset shows the menisci shape between neighbouring particles. Several factors must be taken into account: the substrate withdrawal rate v_w, the array growth rate v_c (different from v_w), the water influx, j_w, the respective particle influx j_p, the water evaporation flux j_e, and s the thickness of the array h.

1.12 Requirements for the Array Formation Process

The requirements for producing regular particle monolayers on solid substrates can be summarized as follows:

1. the substrate must be well wettable by the suspension, and a wetting film with relatively parallel surfaces and thickness on the order of but less than the particle diameter must be formed
2. for the formation of densely packed structures, the particles must be able to slide on the substrate before the film dries, in the case of adsorbing particles, an amorphous layer is expected to be formed

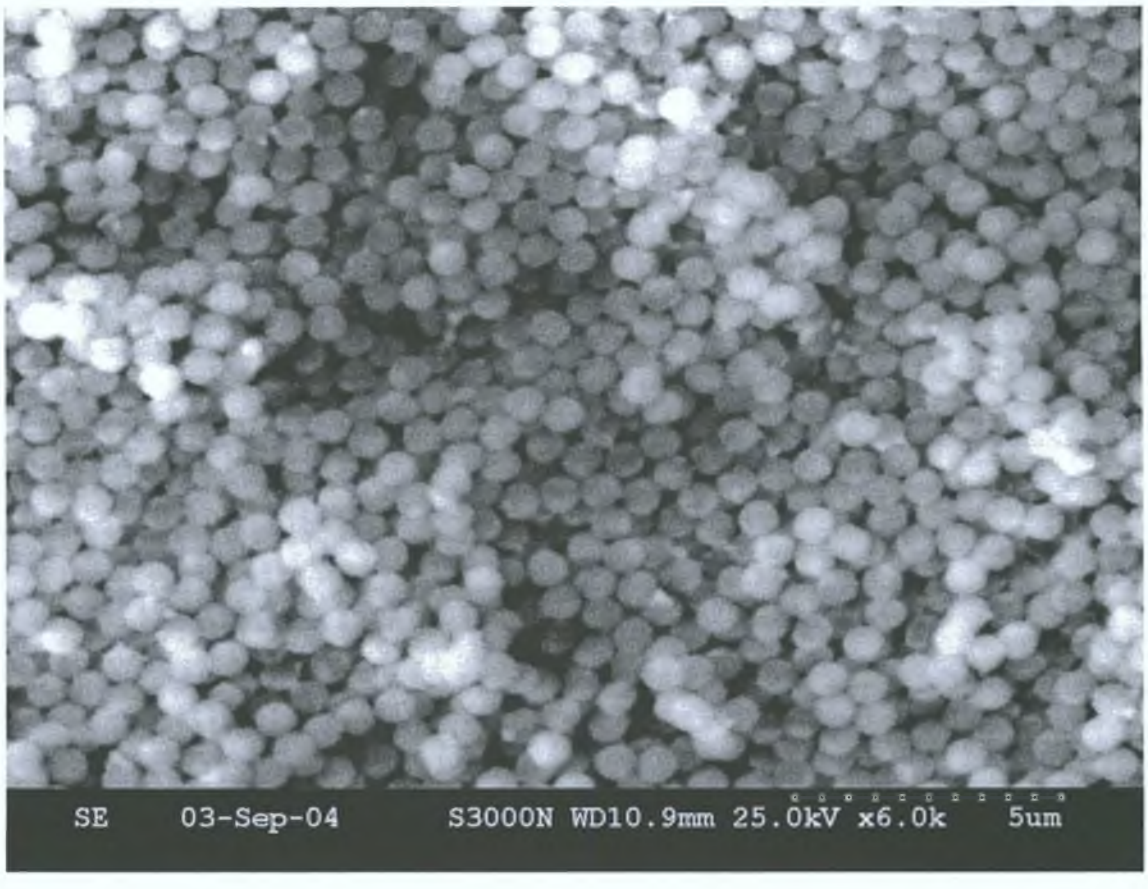

Fig. 1.17 SEM micrograph of an amorphous layer; its formation is caused by an evaporation rate too high to allow particles rearrangements into close-packed arrays

3. the suspension must be stable, and in the case of larger particles (~1 μm and above), sinking of the particle must be prevented

4 to prevent the aggregation of particles at the suspension surface, the evaporation must be restricted near the particle film, that is, the atmosphere at the suspension meniscus as well as at the suspension surface far from the film must be saturated with water vapour and the water evaporation from the particle arrays must be slow enough At high evaporation rates instabilities in the array growth may arise as, for example, rupturing or stripping of the array film

1.13 Cyclic Voltammetry

Cyclic voltammetry is used in this project for three main objectives

- understanding and monitoring the electrochemical processes at the surface
- surface area determination of the electrodes
- electrochemical cleaning

Among all the methods available for studying electrode process, potential sweep methods are probably the most widely used They consist in the application of a continuously time-varying potential to the working electrode This results in oxidation or reduction reactions of electroactive species in solution (Faradaic reactions, involving charge transfer across the solid/liquid interface), possibly adsorption of species depending on the potential and a capacitive current due to double layer charging Rapid-voltage scan techniques in which the direction of voltage scan is reversed are called cyclic techniques A ramp is applied over the full voltage-scan range and then reversed so that a descending ramp returns, almost invariably to the original potential The scan rate in the forward and reverse directions is normally the same, so that the excitation waveform has the shape of an isosceles triangle

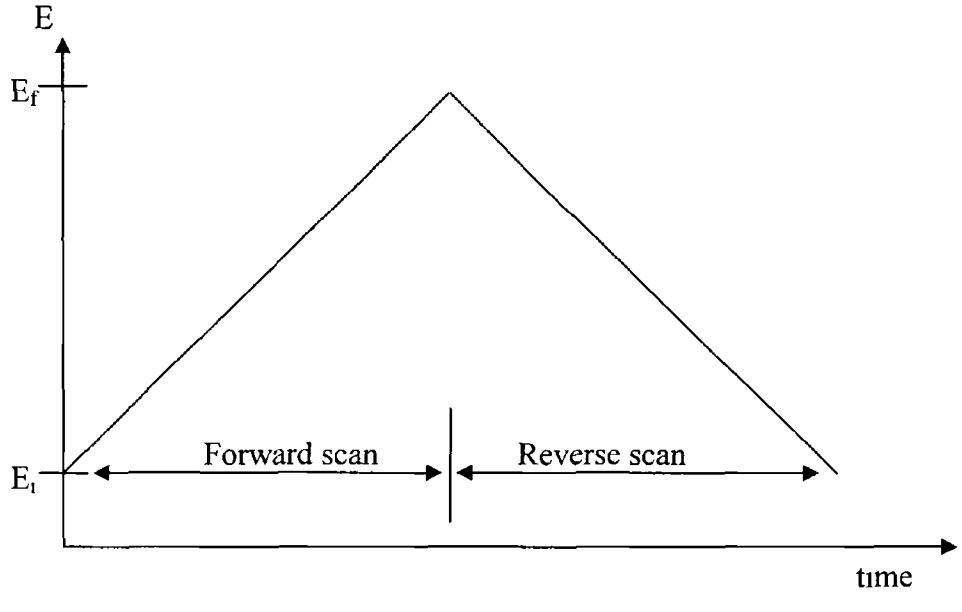

Fig 1 18 A typical potential excitation waveform used in cyclic voltammetry

Cyclic voltammetry is that voltammetric technique in which the current that flows in a system is measured as a function of time and in which the excitation signal is a triangular potential. The measured parameters are the anodic and cathodic peak potentials parameters, the anodic and cathodic peak currents and the half-peak potentials, which are the potentials at which the cathodic and anodic currents reach half of their peak values. A faradaic current, I_f, due to the electrode reaction, is registered in the relevant zone of of applied potential where electrode reaction occurs. There is a capacitive contribution also: on sweeping the potential the double layer charge changes; this contribution increases with increasing sweep rate. The total current is

$$I = I_C + I_f = C_d \frac{dE}{dt} + I_t \qquad (11)$$

The peak current density j_p in a cyclic voltammogram for a reversible system relates the peak current, ip, with the scan rate, according to the Randles-Sevcik equation:

$$i_p = 0.4463nFAC(nFvD/RT)^{1/2} \qquad (12)$$

In this equation, n is the number of electrons appearing in half-reaction for the redox couple, v is the rate at which the potential is swept (V s^{-1}), F is Faraday's constant (96485 C mol^{-1}), A is geometric the electrode area (cm^2), R is the universal gas constant (8.314 J / mol K), T is the absolute temperature (K), and D is the analyte's diffusion coefficient (cm^2/sec). If the temperature is assumed to be 25°C (298.15 K), the Randles-Sevcik equation can be written in a more concise form,

$$i_p = (2.687 \times 10^5) n^{3/2} v^{1/2} D^{1/2} AC \qquad (13)$$

In a typical CV study, series of experiments are run varying selectively the potential scan rate, the experiment temperature, the species concentration or the ionic strength of the supporting electrolyte. The diffusion coefficient of a species can be determined by modifying the scan rate in a series of experiments. For a reversible system, the peak height will increase linearly with the square root of the scan rate. The slope of the resulting line will be proportional to the diffusion coefficient, as shown in the Randles-Sevcik equation.

The independent variables are the voltage scan rate and the window in which the scan is performed This powerful technique allows to identify adsorption/desorption processes and to monitor electrodeposition reactions It is useful to run multiple CV experiments as it allows time dependent phenomena to be noticed

All electrochemical experiments were carried out in a standard three-electrode cell at room temperature using CH electrochemical workstations (potentiostats) A potentiostat is an electronic device that controls the voltage difference between a working electrode and a reference electrode Both electrodes are contained in an electrochemical cell The potentiostat implements this control by injecting current into the cell through an auxiliary, or counter, electrode In almost all applications, the potentiostat measures the current flow between the working and auxiliary electrodes

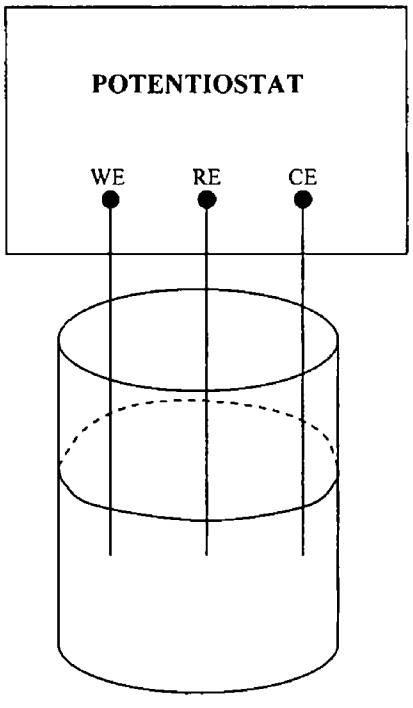

Fig 1 19 3-electrode cell

WE working electrode (where the potential is controlled and where the current is measured, "inert" material such as gold, platinum, or glassy carbon the WE serves as a surface on which the electrochemical reaction takes place)

RE reference electrode, used in measuring the WE potential It should have a constant electrochemical potential as long as no current flows through it The most common lab reference electrodes are the Saturated Calomel Electrode (SCE) and Ag/AgCl electrodes

CE counter electrode, a conductor that completes the cell circuit The counter (auxiliary) electrode in lab cells is generally an inert conductor like platinum or graphite

1.14 Electrodeposition

The majority of the fundamental electrode reactions involve the formation of a deposit, either as a result of the reduction of ions in solution, as in the case of metal deposition, or by oxidation of the electrode and subsequent reaction with anions to form an anodic film All the electrode process of this kind can be included in a single term electrocrystallisation Several distinct stages are implied in this concept

1 diffusion of ions in solution to the electrode surface
2 electron transfer
3 partial or complete loss of the solvation sheath, resulting in the formation of ad-atoms
4 surface diffusion of ad-atoms
5 clustering of ad atoms to form critical nuclei on a perfectly smooth surface or on a foreign substrate
6 incorporation of ad-atoms at lattice sites
7 development of crystallographic and morphological features of the deposit

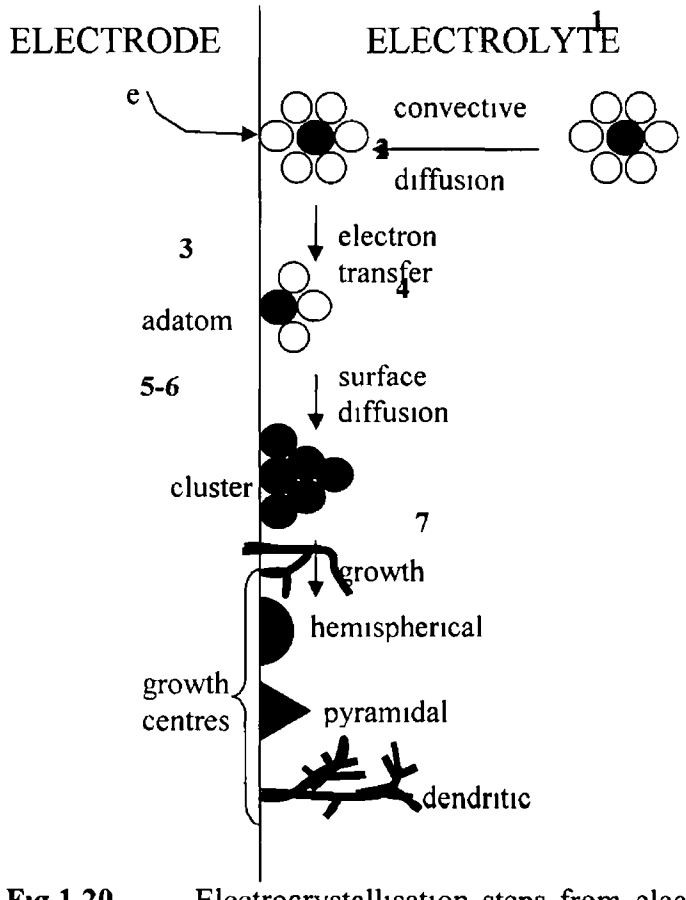

Fig 1 20 Electrocrystallisation steps from electrolyte diffusion to nucleation and growth

The dynamic equilibrium of a generic electrode process can be written as:

$M^{z+}+ze^- \rightleftharpoons M$

The electrode potential E is given by the Nernst equation as a function of the ionic activities:

$$E = E_0 - \frac{RT}{zF}\ln\left[\frac{a(M)}{a(M^{z+})}\right] \qquad (14)$$

where E is the reduction potential, E_0 is the standard potential for the reaction, R is the gas constant, T is the temperature, F is the Faraday's constant, z is the number of electrons transferred and $a(M)$ and $a(M^{z+})$ are the activities of M and M^{z+} respectively.

A challenging objective of the electrodeposition efforts of this project concerns fabricating substrates with novel morphologies aiming to enhance new and interesting properties on the electrode compared to the bare metal (flat) surface. Two routes have been investigated to pursue this aim:

- templated electrodeposition (used for growing nano-clusters and single-particle structures)
- non-templated electrodeposition (utilized to obtain cavities and nanoporous networks)

1.15 Non-Templated Electrodeposition

Non-templated electrodeposition has been investigated in this project as certain gold electrodeposits, especially after electrochemical roughening, were found to exhibit strong SERS enhancements and hence considered potentially suitable for SERS (Surface Enhanced Raman Scattering) based sensors.

Although non-templated electrodeposition allows less control over the final structure and morphology of the electrodeposit compared with templated electrodeposition, the nanoscopic size of electrodeposits obtained in this way can be easily controlled, yielding interesting materials such as metal blacks. These are electrodeposits of metals such as platinum and gold where the deposited particles are small enough (10-20nm)

and at such high densities that they appear black in colour instead of the shiny metallic colour normally found Imamura et al [78] exploited the properties of these materials to fabricate porous gold-black electrodes potentially suitable for biosensing devices, while platinum blacks were first produced by electrodeposition over a century ago as reported by Lummer, Kurlbaum and Sitzungsber (1894) [79]

Electrodeposition is usually carried out from a readily available salt of the metal of interest, for example gold is commonly deposited from a $HAuCl_4$ precursor while platinum is mainly electrodeposited from solutions of H_2PtCl_6 or $Pt(NH_3)_4Cl_2$ Electrodeposition occurs when the electrode is held at a sufficiently negative potential to lead to the reduction of the metal ion at the electrode This results in nucleation and growth of deposits of the metal on the surface, which can eventually overlap to completely cover the electrode surface Metals at the nanometre scale exhibit unusual physico-chemical behaviours in comparison with their corresponding bulky structures Furthermore, the properties of the deposited metal can be controlled by varying several parameters such deposition applied potential, deposition time and presence or absence of growth inhibitors and additives Scharifker and Hills[80] (1983) have shown that nucleation can occur either instantaneously or progressively depending on the electrodeposit and the substrate When the instantaneous mechanism is observed all of the nuclei form instantaneously and subsequently increase in size depending on the time of deposition making this a relatively predictable mechanism Whilst in progressive nucleation the number of nuclei is a function of nucleation time therefore their size and distribution is less uniform

1.16 Nucleation and growth

The electrocrystallisation of a new phase involves one of two kinds of nucleation, namely instantaneous or progressive, with the electrodeposited material growing on the substrate according to one of two types of growth mode, either two-dimensional (2-D) or three-dimensional (3-D), which subsequently overlap to give a continuous deposit The number of nuclei in the instantaneous nucleation is constant, and they grow on their former positions on the bare substrate without the formation of new nuclei Hence, the radii of nuclei are larger and the surface morphology is rougher

In the 2-D growth the nuclei grow more quickly in the parallel direction than the perpendicular direction until they overlap and coalesce However, in the 3-D growth, the growth rates of nuclei are basically equal or comparable in the directions parallel or perpendicular to the electrode surface The geometry of growth centre is sensitive to the interaction between the deposit and substrate material A number of different theoretical growth models and fit-methods are documented in literature, allowing to devise informations about the kinetics and extract nucleation rates from current-time transients [81 84] The shape of solid metal growth centres is complex Abyaneh[85] has reviewed the existing electrocrystallisation models responsible for the growth of thick deposits They can be divided in three categories

1 models of growth leading to shape preserving tophographies in this category only the model of right-circular cones (Figure 1 21) has been fully analysed [86]

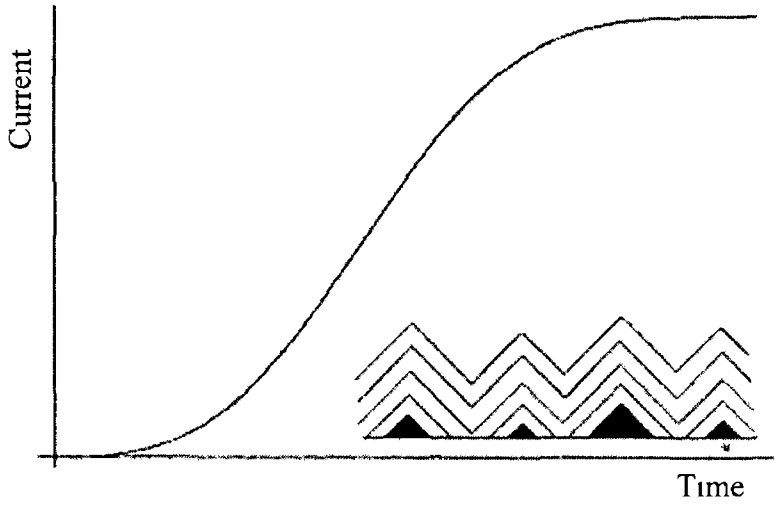

Fig 1 21 The form of CTT derived for the model of growth of right-circular cones

2 models of growth leading to shape-changing topographies in this category the growth of hemispheres[87] (Figure 1 22) or more generally of spherical caps[88] or hemi-spheroids[89,90] has been investigated

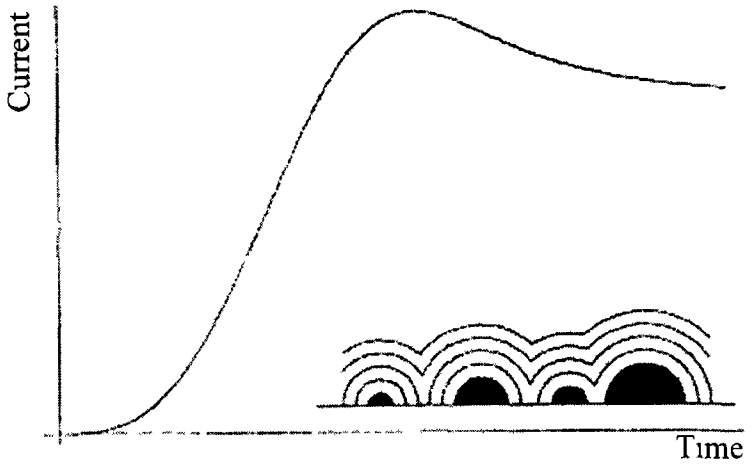

Fig 1 22 The form of CTT derived for the model of growth of hemispheres

3 One-dimensional needle-like growth

The development of the latter growth model and the analysis of the competition between these growth forms represent challenging topics of the current modelling and simulation efforts However, for the purpose of the present work it is instructive to consider geometries which simplify the complex stochastic theoretical treatment and lead to analytical expressions for the current time transients If for example the growth centre is represented as a right-circular cone, growth parallel to the surface occurs with one rate constant and that perpendicular to the surface with a different rate constant The units of these constant are mol $cm^{2}s^{1}$ The total current into the growing cone can be obtained by integration of the contributions of a stack of discs

Scharifker and Hills devised formulae to represent current transients representative of each of the four nucleation types and growth modes The dimensionless forms of 3-D growths for instantaneous and progressive nucleation are given by

- 3-D progressive

$$(I/I_{MAX})^2 = \frac{1\ 2254}{(t/t_{MAX})}\{1-\exp[-2\ 3367(t/t_{MAX})^2]\} \qquad (15)$$

- 3-D instantaneous

$$(I/I_{MAX})^2 = \frac{1\ 9542}{(t/t_{MAX})}\{1-\exp[-1\ 2564(t/t_{MAX})]\}^2 \qquad (16)$$

where the parameters t_{MAX} and I_{MAX} represent the coordinates of the current maximum The theoretical curves for nucleation and growth obtained from these equation can be fitted with the experimental data of the current transients

1.17 Effects of additives and growth inhibitors

In the literature several additives and growth inhibitors have been used to gain control over nucleation and growth In particular, in the case of gold, silver and platinum lead acetate, iodide and sulfide ions, alkane thiols have shown to affect significantly these two processes, resulting in a remarkable reduction in average nanoparticle size and increased deposition density Layson et al [91], extending the studies reported in literature for defect-driven deposition for lead[92] and silver [93], have suggested a thermodynamically reasonable mechanism for the action of lead acetate on platinum electrodeposition to yield platinum blacks STM and SEM have been exploited to probe the morphology of these deposits They analyzed the adsorption of lead ions on highly oriented pyrolytic graphite (HOPG) surface and suggested that lead ions acted as electron transfer sites between the electrode surface and the platinum ions in solution resulting in a greater number of nucleation sites Pb ions could be considered pseudo-defects acting as nucleation centers for Pt islands on the flat areas of the HOPG surface El-Deab et al [94] have investigated the effect of electrodeposition of gold on glassy carbon from $Na[AuCl_4]$ in 0 5M H_2SO_4 in the presence and absence of Iodide ions and alkane thiols (cysteine) acting as inhibitors They found that the presence of iodide ions in the electroplating bath yielded a significant reduction in average nanoparticle size from 20-200nm in the absence of iodide to 10-40nm when present Also a four-fold increase in particle density was observed in SEM micrographs from 72 to 300 particles per μm in the presence of iodide (Figure 1 23) This behaviour was explained with the fact that the iodide ions adsorbed onto the surface of the gold nuclei upon formation preventing growth, and that a negative charge on the iodide ions prevented the coalescence of neighbouring gold nanoparticles through repulsion

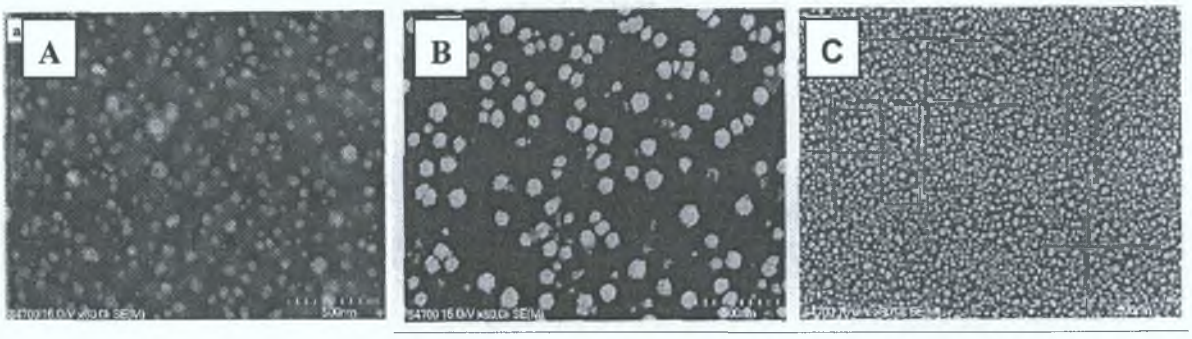

Fig.1.23 SEM micrographs of gold nanoparticles electrodeposited on glassy-carbon in presence of (A) no additive, (B) cysteine and (C) potassium iodide – El Deab et al. (2005)

The presence of cysteine was found to result in a small net increase in the average particle size, which could be reasonably explained taking into account the interaction between carboxylic acid and amino groups on the adsorbed cysteine through hydrogen bonding: this driving force leads to preferential coalescence of neighbouring gold nanoparticles, resulting in a subsequent reduction in particle density.

Cyclic voltammetry of the reductive desorption of the cysteine self assembled monolayer (SAM) on the gold nanoparticles was also performed by El-Deab[94] et al. and this revealed that when electrodeposition was performed under conditions of high cysteine concentration (100μM) the relative amount of Au(111) formed increased compared to Au(100) and Au(110). Thus, the presence of alkane thiols was shown to effect the crystallisation of the deposits. The authors suggested that this effect could be as a result of cysteine having a weaker bond strength with Au(111) than with Au(110) and Au(100) as shown by Arihara et al.[95] and El-Deab et al.[96] Formation of a cysteine SAM on the gold nuclei retarded further growth of the nanoparticle but the weak nature of the bond at the Au(111) sites meant that further growth of Au(111) was possible at these sites resulting in an increase in the relative Au(111) content of the nanoparticles.

Bonroy et al.[97], aiming to maximise the electrode surface area for protein (antibody) biosensor applications, have reported that gold electrodeposition, using hydrogen tetrachloro-aurate as precursor in presence of lead (II) acetate as an additive, can be utilised for a "gold black" on a titanium/gold vapour deposited quartz crystal electrode. Through their optimised technique they reported an impressive increase in the adsorption of both thiol (11.4-fold) and protein (3.3-fold) adsorptions onto a gold: such a surface could potentially lead to a significant increase in sensitivity for any biosensor applications it is used with. Zweifel and Wei[98] documented that the growth of gold

nanorods can be arrested at intermediate stages by treatment with Na_2S, providing greater control over their optical resonances the quenching can be easily achieved by adding sulfide at millimolar concentrations, resulting in chemically and optically stable species with specific NIR resonances The stabilizing effect of sulfide can be attributed to two processes

1 the reduction or quenching of unreacted metal salts
2 the adsorption of sulphide onto the nanorod surfaces

The latter has the added benefit of shifting the plasmon resonance further into the NIR spectral region The structural and optical stability of the sulfide-treated nanorods make them attractive candidates as contrast agents for optical coherence tomography and other biophotonic applications

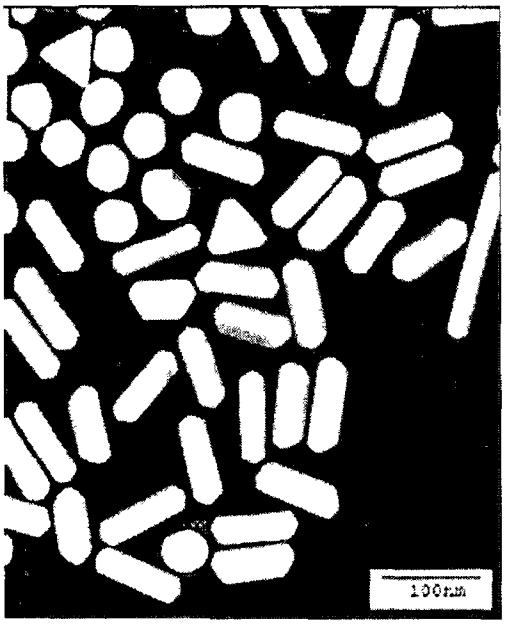

Fig 1 24 TEM image (Philips CM-10, 80 kV) of anisotropic Au nanoparticles prepared in the absence of AgNO3, followed by quenching with Na_2S - Zweifel and Wei (2005)

1.18 Templated Electrodeposition

Templated electrodeposition is a very popular way of obtaining surfaces with electrodeposits of controlled size, controlled morphology and controlled position There have been many ways applied to obtain control over these parameters of the electrodeposit, however there exists two broad categories in the area of templated electrodeposition, restrictive template-based electrodeposition and active template assisted deposition Restrictive template-based electrodeposition involves limiting access of the electrolyte to the electrode during the electrodeposition process, so that the specific location and morphology of the electrodeposit is controlled

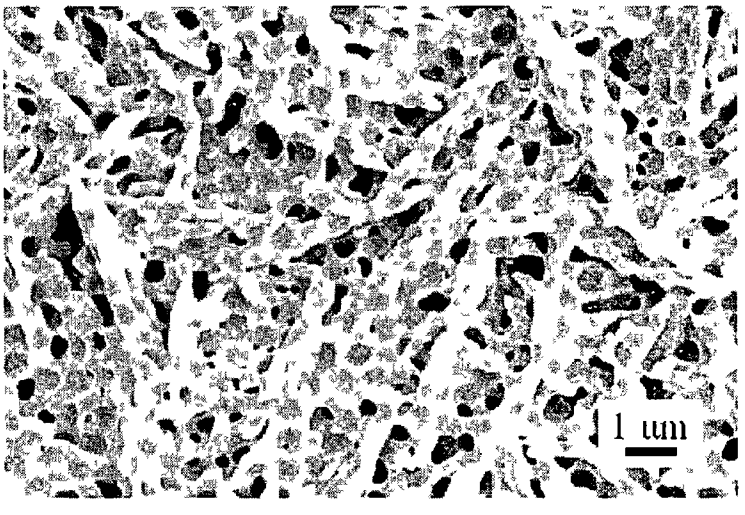

Fig 1 25 SEM Micrograph of pores (radius 322nm) in gold made with polystyrene latex template

Bartlett, Ghanem, Abdelsalam et al [99 108] have extensively studied templated electrodeposition utilizing polystyrene nanospheres of several sizes and they have developed a similar method for the deposition of macroporous platinum, palladium and cobalt using polystyrene latex spheres as a template on a gold electrode substrate As with Wijnhoven[109] et al (Figure 1 25) the template and deposit can be grown up over several layers to obtain a multilayer array of interconnected spherical voids

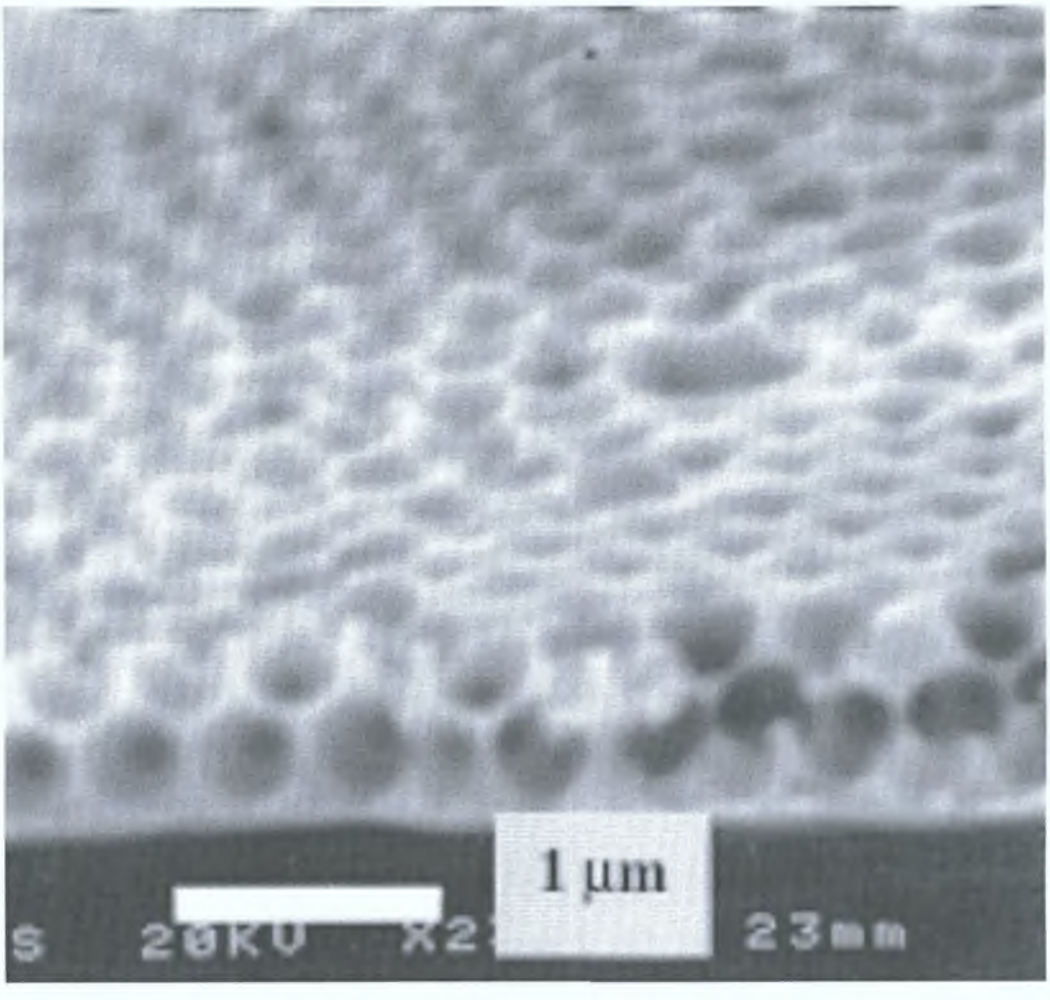

Fig. 1.26 Scanning electron micrograph of cross sectional view of macroporous platinum

Ghanem et al. and Zhukov et al.have investigated an interesting double-templated method for electrodeposition. They have shown that polystyrene spheres formed into a self-assembled monolayer on a gold substrate could be dissolved following the electrodeposition of a conducting polypyrrole polymer onto that gold surface. The resulting electrodeposited polypyrrole would contain cavities where the polystyrene had blocked its electrodeposition in a similar way to the examples discussed above. Then the polypyrrole can be converted to an insulator by potential cycling so that the metal of interest (e.g. Gold, Platinum, Nickel) would deposit only into the cavities left by the polystyrene. Finally the polypyrrole can be dissolved to leave arrays of metal nanodots. They showed that the size, separation and degree of connectivity (if any) between these nanodots could be controlled by the diameter of the polystyrene spheres used and by controlling the height of deposition in the template cavity.

1.19 Optical diffraction

Figure 1 27 displays a the effect of the viewing angle variation on the colour of opaline surfaces Photonic crystals are strongly coloured, the precise colour depending on the viewing angle, void diameter and film thickness Since the diffraction colour depends on the photonic crystal lattice constant, changing the distance between the nanospheres changes the colour

Bragg's law and Snell's law can be employed to describe the position of angle-resolved diffraction peaks In general, the Bragg equation is useful in providing information on the relation between the diffraction-peak position and the lattice constant when the incidence angle is given

An approximation of the reflection stop band gap position is expressed by a modification of Bragg's law taking into account Snell's law of refraction[110]

$$\lambda = 2d_{hkl} n_{eff} \sin\theta \qquad (17)$$

For the (111) plane, lattice constant d_{hkl} coincides with d_{111}, which is the interplanar spacing of fcc (111) planes, and n_{eff} is the effective refractive index of the PC crystal film, θ is the angle between the incident beam and the normal to the (111) plane, λ is the free-space wavelength of the light The effective refractive index is also calculated from the equation for fcc structures

$$n_{eff}^2 = n_a^2 f + n_b^2 (1 - f) \qquad (18)$$

where n_a and n_b are the refractive indices of the PS nanospheres and the surrounding medium, respectively, f is the volume fraction of the PS nanospheres in the film and is approximately 74%, based on a perfect hexangular packing geometry of identical spheres, n_a = 1 59 (PS nanospheres) and n_b = 1 0 (air in the voids) As the surface of our samples is predominated by (111) face, the lattice constant can be calculated according to the following equation

$$d_{111} = (2/3)^{1/2} D \qquad (19)$$

where D is the diameter of the PS spheres

In general, the m^{th}-order position of the Bragg diffraction peak λ_m can be calculated, once the fcc lattice is identified with the (111) face parallel to the substrate with the lattice constant D, incidence angle θ, volume fraction f, and effective refractive index n_{eff}, from the modified Bragg equation

$$m\lambda_m = 2d_{111}(n_{eff}^2 - \sin\ \theta)^{1/2} \tag{20}$$

1.20 Raman Spectroscopy

Raman spectroscopy is a powerful non-destructive technique. The vibrational Raman spectrum provides a fingerprint which characterises chemical and molecular structure. The spectroscopic information can be regarded as similar in content but superior to that provided by Infra-red spectroscopy. Raman scattering is an inelastic light scattering process in which a laser photon is scattered by a sample molecule or crystal and loses energy during the process. The amount of energy loss is characteristic of the molecule and peculiar of the chemical bonding. It enables highly specific identification without ambiguity, in gas, liquid or solid phase. It can also provide informations on samples which may otherwise be difficult to analyse such highly coloured or fluorescent samples.

Since the observation of Raman spectra for pyridine adsorbed on roughened silver electrodes[111] and the subsequent realisation that there was a very significant ($\sim 10^6$) surface enhancement of the Raman intensity at the roughened silver surface[112,113] the technique of surface enhanced Raman spectroscopy has been widely applied to study molecules at electrochemically roughened metal electrode surfaces. SERS is a very attractive in situ technique for the study of electrode surfaces and electrochemical processes since, being the surface enhancement extremely surface-selective, the technique is sensitive to molecules adsorbed at, or very close to, the electrode surface and its response differentiates from molecules in the bulk solution. Furthermore, SERS provides information about the molecular structure of the adsorbate, its orientation at the surface and the dependence of orientation and coverage on applied potential. Another generally interesting aspect of SERS is attributed to its spatial resolution. About 20 years after the discovery of the effect, new methods for determining cross sections effective in SERS resulted in unexpectedly large cross sections on the order of at least 10^{-16} cm^2/molecule corresponding to enhancement factors of about 14 orders of magnitude compared with normal non-resonant Raman Scattering.[114]

The Raman cross section for water is low, therefore SERS can be easily used to study electrodes in aqueous solution. Besides its remarkable advantages, SERS is effected by two main limitations. Firstly, although the electrochemical roughening process allows to fabricate SERS active surfaces for metals such as Cu, Ag, and Au the surface

enhancement is not reproducible, its intensity varies from place to place across the electrode surface and is not stable Such effective Raman cross sections, on the same order of magnitude as fluorescence cross sections of good laser dyes, corroborated the possible use of Raman Scattering systems as single-molecule detectors

Secondly, the roughened surfaces undergo irreversible loss of enhancement at negative potentials

Using regular arrays of gold nanoparticles deposited by a lithographic technique on indium tin oxide (ITO) coated glass, Tessier et al [115] firstly and Felidj et al [116 117] later have observed a SERS effect for the *trans*-1,2-two (4-pyridyl) ethylene (BPE) molecule adsorbed on such arrays with a gain per molecule ranging from 10^4 to 10^5 Very recently Abdelsalam et al [118], using benzene thiol as test-molecule, have shown that structured gold surfaces formed by template electrodeposition can give strong surface enhanced Raman scattering, demonstrating the first use of these surfaces for in situ electrochemical SERS This enhancement is quite reproducible from place to place on the sample surface (unlike conventional roughened electrode surfaces) is stable and the surfaces can be cleaned and reused The order of magnitude of this enhancement is significantly weaker than that usually obtained on electrochemically roughened electrodes for which it can rise 10^7–10^8 the challenging problem of optimising the parameters for maximising the enhancement for these novel platforms (choice of the Raman-active molecule, radiation wavelength, nanopores size) is still far from being solved

Furthermore, gold has been chosen to base this project on due to some peculiar properties related to its strong surface plasmon resonance (SPR) photonic excitation of gold nanoparticles in the 10-200 nm size range generates localized SPR (L-SPR) while smooth thin films of gold with thickness in the 10-200 nm range yield propagating plasmons, commonly named surface plasmon polaritons (SPPs) In the 10–200 nm size range generating an enhancement of the incident electric field E near the particle surfaces such that $|E|^2$ can be 10^2-10^5 times greater in intensity than the incident field The field has a spatial range on the order of 10–50 nm and is strongly dependent on nanoparticle size, shape and local dielectric environment Propagating plasmons, which are often called surface plasmon polaritons (SPPs), are associated with smooth, thin films of silver and gold with thicknesses in the 10–200 nm range Propagating plasmons lead to smaller field enhancements (10–100 times) and a larger spatial range (~1000 nm) Target molecules may bind indirectly to gold surfaces via self-assembled monolayers (SAMs) of suitable linker molecules on the gold surface (Figure 1 28)

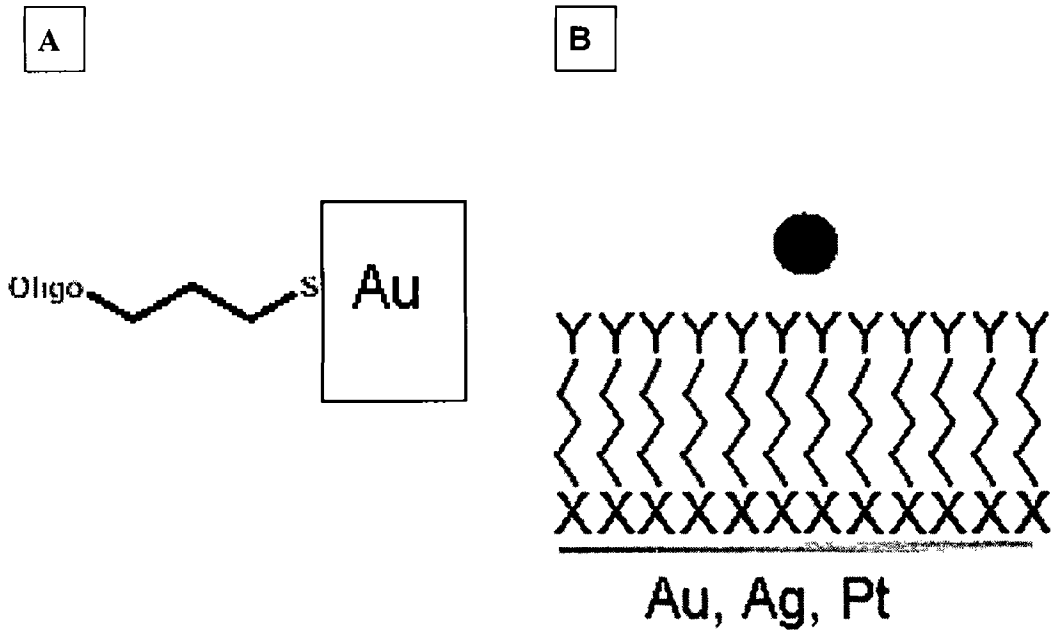

Fig 1 28 A)Biomolecule (DNA) linked to gold surface via thiol functionality
B) Self-Assembled Monolayer of linker molecules interacting with protein – Armstrong and Wilson (2000)

These factors make gold a suitable, however if successful it will be possible to extend much of the advances accomplished with gold to other metals such as platinum, silver and copper among others

REFERENCES

[1] Whitesides, G M *Small* **2005**, *1*, No 2, 172

[2] Rotello, V *Nanoparticles building blocks for nanotechnology* New York Springer Science+Business Media, Inc, **2004**

[3] Kaifer, A E , Gomez-Kaifer, M *Supramolecular electrochemistry* Wiley-VCH, **1999**

[4] Peidong, Y *The chemistry of nanostructured materials* Singapore World Scientific, **2003**

[5] Park, S -E et al *Nanotechnology in mesostructured materials Proceedings of the 3rd International International Mesostructured Materials Symposium*, Amsterdam Elsevier, **2003**

[6] Balzani, V Credi, A Venturi, M *Molecular devices and machines a journey into the nano world* Weinheim Wiley-VCH, **2003**

[7] Pavesi, L Buzaneva, E *Frontiers of nano-optoelectronic systems* Boston, MA, Dordrecht, Netherlands Kluwer Academic Publishers, **2000**

[8] Binnig, G Quate, C F Gerber, C *Phys Rev Lett* **1986**, *56*, 930

[9] Ulman, A *Chem Rev* **1996,** *96*, 1533

[10] Lawrence, D S Jiang, T Levett, M *Chem Rev* **1995**, *95*, 2229

[11] Dutta J , Hoffmann H *Encyclopedia of Nanoscience and Nanotechnology* Edited by H S Nalwa Vol X, pp 1-23

[12] Prasadet, T *Optical Materials* **2005**, *27*, 1250

[13] Reculusa, S Ravaine, S *Applied Surface Science* **2005**, *246*, 409

[14] Li, H Meng, B Di, Y Li, X *Synthetic Metals* **2005**, *149*, 225

[15] Deng, J Tao, X Li, P Xue, P Zhang, Y Sun , X Kwan K C *Journal of Colloid and Interface Science* **2005**, *286*, 573

[16] Rogach, A L Kotov, N A Koktysh, D S Ostrander, J W Ragoisha, G A *Chem Mater* **2000,** *12*, 2721

[17] Kuai, S -L Hub, X -F Hache, A Truong, V -V *Journal of Crystal Growth* **2004**, *267*, 317

[18] Ng, V Lee, Y V Chen B T Adeyeye, A O *Nanotechnology* **2002**, *13*, 554

[19] Qiu, M *Optics Letters* **2005**, *30*, 1476

[20] Kuang, W Kim, C Stapleton, A Kim, W J O'Brien, J D *Optics Letters* **2003**, *28*, 1781

[21] Yoshie, T Vučkovic, J Scherer A Chen H Deppe D *Applied Physics Letters* **2001**, *79*, 4289

[22] Foresi, J S Villeneuve, P R Ferrera, J Thoen, E R Steinmeyer, G Fan, S Joannopoulos, J D Kimerling, L C Smith, H I Ippen, E P *Nature* **1997**, *390*, 143

[23] Lodahl, P van Driel, A F Nikolaev, I S Irman, A Overgaag, K Vanmaekelbergh, D Vos, W L *Nature* **2004**, *430*, 654

[24] Tanabe, T Notomi, M Mitsugi, S Shinya, A Kuramochi E *Appl Phys Lett* **2005**, *87*, 151112

[25] Jeong, U Kim, J -U Xia, Y Li, Z -Y *Nano Lett* **2005**, *5*, 937

[26] Centeno E Cassagne, D *Optics Lett* **2005**, *30*, 2278

[27] Zhou, J Zhou, Y Ng, S L *Appl Phys Lett* **2000**, *76*, 3337

[28] Wong, S Kitael, V Ozin, G V *J Am Soc* **2003**, *125*, 589

[29] Wijnhoven, J E G J Vos, W L *Science* **1998**, *281*, 802

[30] Trau, M Yao, N Kim, E Xia, Y Whitesides, G M Aksay, I A *Nature* **1997**, *390*, 674

[31] Holland, B T Blanford, C F Stein, A *Science* **1998**, *281*, 538

[32] Gu, Z Z Fujishima, A Sato, O *Chem Mater* **2002**, *14*, 760

[33] Sawada, T Suzuki, Y Toyotama, A Iyi, N *Jpn J Appl Phys Lett* **2001**, *40*, L1226

[34] Park, S H Qin, D Xia, Y *Adv Mater* **1998**, *10*, 1028

[35] Griesebock, B Egen, M Zentel, R *Chem Mater* **2002**, *14*, 4023

[36] Yang, S M , Miguez, H , Ozin, G A *Adv Funct Mater* **2002**, *12*, 425

[37] Park, S H , Qin, D Xia, Y N *AdV Mater* **1998**, *10*, 1028

[38] Li, H -L , Dong, W , Bongard, H -J , Marlow, F *J Phys Chem B* **2005**, *109*, 9939-9945

[39] Denkov, N D , Velev, O D , Kralchevsky, P A , Ivanov, I B , Yoshimura, H , Nagayama, K *Nature* **1993**, *361*, 26

[40] Dimitrov, A S Nagayama, K *Langmuir* **1996**, *12*, 1303

[41] Jiang, P Bertone, J F Hwang, K S Colvin, V L *Chem Mater* **1999**, *11*, 2132

[42] Ye, Y H LeBlanc, F Truong, V -V *Appl Phys Lett* **2000**, *78*, 52

[43] Kuai, S -L Hub, X -F Hache, A Truong V -V *Journal of Crystal Growth* **2004**, *267*, 317

[44] Kralchevsky P A and Denkov, N D *Curr Opin Coll Interf Sci* **2001**, *6*, 383

[45] Yamaki, M Higo, J Nagayama, K *Langmuir* **1995**, *11*, 2975

[46] Reyes, Y Duda, Y *Langmuir* **2005**, *21*, 7057

[47] Yablonovich, E *Phys Rev Lett* **1987**, *58*, 2059

[48] John, S *Phys Rev Lett* **1987**, *58*, 2486

[49] Tirumkudulu, M S , Russel, B W *Langmuir* **2005**, *21*, 4938

[50] Hertz, H *J Reine Angew Math* **1881**, *92*, 156

[51] Frenkel, J *J Phys* **1945**, *9*, 385

[52] Johnson, K , Kendall, K , Roberts, A *Proc R Soc London, Ser A* **1971**, *324*, 301

[53] Derjaguin, B V , Muller, V M , Toporov, Yu P *J Colloid Interface Sci* **1975**, *53*, 314

[54] Maugis, D *J Colloid Interface Sci* **1992**, *150*, 243

[55] Bharat, B *Handbook of Micro/Nanotribology* / Ed by - 2d ed - Boca Raton etc CRC press, **1999**

[56] Routh, A F , Russel, W B *Langmuir* **1999**, *15*, 7762

[57] Routh, A , Russel, W , Tang, J , El-Aassser, M S *J Coat Technol* **2001**, *73* (916), 41

[58] Chiu, R , Garino, T , Cima, M *J Am Ceram Soc* **1993**, *76* (9), 2257

[59] Chiu, R , Cima, M *J Am Ceram Soc* **1993**, *76* (11), 2769

[60] Keddie, J L *Mater Sci Eng R* **1997**, *21* 101

[61] Steward, P A Hearn, J Wilkinson, M C *Adv Colloid Interface Sci* **2000**, *86*, 195

[62] Rottstegge, J Haub, B Wilhelm M Landfester, K Heldmann, C Spiess H W *Macromol Chem Phys* **2003**, *204*, 787

[63] Cramer, S E Jeschke G Spiess, H W *Macromol Chem Phys* **2002**, *203*, 182

[64] Visschers, M , Laven J , German A L *Progress Org Coating* 1997, **31**, 311

[65] Hiemenz, P C , Rajagopalan, R *Principles of Colloids and Surface Chemistry* 2nd ed , Marcel Dekker, Inc New York, **1997**

[66] Brown, G L *J Polym Sci* **1956**, *22*, 423

[67] Mason, G Morrow, N *J Colloid Interface Sci* **1986**, *109*, 46

[68] Rabinovich, Y I Esayanur, M S Moudgil B M *Langmuir* **2005**, *21*, 10992

[69] Lu, Y Yin, Y Xia, Y *Adv Mater* **2001**, *13*, 34

[70] Yin, Y Lu, Y Xia, Y *J Am Chem Soc* **2000**, *123*, 771

[71] Park S H Xia, Y *Adv Mater* **1998**, *10*, 1045

[73] Valtchev V *Chem Mater* **2002**, *14*, 956

[74] Zakhidov, A A Baughman, R H Iqbal, Z Cui, C Khayrullin, I Dantas, S O Marti, J Ralchenko, V G *Science* **1998**, *282*, 897

[75] Johnson, S A Ollivier, P J Mallouk, T E *Science* **1999**, *283*, 963

[76] Di Francia, G. Castaldo, A. Massera, E. Nasti, I. Quercia, L. Rea, I. *Sensors and Actuators B* **2005**, *111*, 135.

[77] Ganley, J.C. Seebauer, E.G. Masel, R.I. *Journal of Power Sources* **2004**, *137*, 53.

[78] Imamura, M. Haruyama, T. Kobatake, E. Ikariyama, Y. Aizawa, M. *Sensors and Actuators B* **1995,** *24*, 113.

[79] Lummer, O. Kurlbaum, F. Sitzungsber, K. *Preuss. Akad. Wiss.* **1894**, 229.

[80] Scharifker, B. Hills, G. *Electrochimica Acta* **1983**, *28*, 879.

[81] Fleischmann, M. Thirsk, H.R. *Trans. Faraday Soc.* **1955**, *51*, 71.

[82] Fleischmann, M. Liler, M. *Trans. Faraday Soc.* **1958**, *54*, 1370.

[83] Abyaneh, M.Y. Fleischmann, M. *Trans. Inst. Met. Fin.* **1980**, *58*, 91.

[84] Abyaneh, M.Y. Fleischmann, M. *J. Electroanal. Chem.* **1981**, *119*, 197.

[85] Abyaneh, M.Y. *Journal of Electroanalytical Chemistry* **2002**, *530*, 82.

[86] Armstrong, R.D. Fleischmann, M. Thirsk, H.R. *J. Electroanal. Chem.* **1966**, *11*, 208.

[87] Abyaneh, M.Y. *Electrochim. Acta* **1982,** *27*, 1329.

[88] Abyaneh, M.Y. *J Electroanal. Chem.* **1986,** *209*, 1.

[89] Abyaneh, M.Y. *Electrochim. Acta* **1991**, *36*, 727.

[90] Abyaneh, M.Y. *J. Electroanal. Chem.* **1995**, *387*, 29.

[91] Layson, A. Columbia, M. *Microchemical Journal*, **1997**, *56*, 103.

[92] Hendricks, S. A. Kim, Y.-T. Bard, A. J. *J. Electrochem. Soc.,* **1992**, *139*, 2818.

[93] Vazquez, L. Hernandez Creus, A. Carra, P.; Ocon, P. Herrasti, P. Palacio, C. Vara, J. M. Salvarezza, R. C.;Arvia, A. J. *J. Phys. Chem.,* **1992**, *96*, 454.

[94] El-Deab, M. Sotomura, T. and Ohsaka, T. *Journal of the Electrochemical society*, **2005,** *152* (1), c1.

[95] Arihara, K. Ariga, T. Takashima, N. Okajima, T. Kitamura, F. Tokuda, K. Ohsaka, T. *Physical Chemistry Chemical Physics* **2003,** *5* (17) 3758.

[96] El-Deab, M. Arihara, K. and Ohsaka, T. *Journal of the Electrochemical Society* **2004,** *151* (6), E213.

[97] Bonroy, K. Friedt, J. Frederix, F. Laureyn, W. Langerock, S. Campitelli, A. Sára, M. Borghs, G. Goddeeris, B. Declerck, P. *Analytical Chemistry* **2004,** *76*, 4299.

[98] Zweifel, D.A. Wei, A. *Chem. Mater.* **2005,** *17,* 4256.

[99] Bartlett, P.N. Birkin, P. and Ghanem, M. *Chemical Communications*, **2000**, 1671.

[100] Bartlett, P.N. Birkin, P.R. Ghanem, M.A. Toh, C.S. *J. Mater. Chem.* **2001**, *11*, 849.

[101] Ghanem, M A Bartlett, P N Bırkın, P R Nettı, M C Baumberg, J J *Chem Mater* **2002,** *14*, 2199

[102] Bartlett, P N Dunford, T Ghanem, M A *J Mater Chem* , **2002,** *12*, 3130

[103] Bartlett, P N Ghanem, M A El Hallag, I S de Groot, P A J Zhukov, A *J Mater Chem* **2003**, *13*, 2596

[104] Nettı, M C Coyle, S Baumberg, J J Ghanem, M A Bırkın, P R Bartlett, P N Whıttaker, D M *Adv Mater* **2001**, *13*, 1368

[105] Zhukov, A A Goncharov, A V de Groot, P A J Bartlett, P N Ghanem, M A *J Appl Phys* **2003**, *93*, 7322

[106] Ben-Alı, S Cook, D A , Bartlett, P N Kuhn, A *Journal of Electroanalytical Chemıstry*, **2005**, *579*, 181

[107] Ben-Alı, S Cook, D A Evans, S A G Thıenpont, A Bartlett, P N Kuhn, A *Electrochem Commun* **2003**, *5*, 747

[108] Coyle, S , Nettı, M C , Baumberg, J J , Ghanem, M A , Bırkın, P R , Bartlett, P N , Whıtaker, D M *Phys Rev Lett* **2001**, *87*, 176801

[109] Wıjnhoven, J Zevenhuızen, S Hendrıks, M Vanmaekelbergh, D Kelly, J Vos, W *Advanced Materıals*, **2000**, *12*, 888

[110] Rıchel, A Johnson, N P McComb, D W *Appl Phys Lett* **2000**, *76*, 1816

[111] Fleıschmann, M Hendra, P J Mcquıllan, A J *Chem Phys Lett* **1974**, *16*, 163

[112] Jeanmarıe, D L Van Duyne, R P *J Electroanal Chem* **1977**, *84*, 1

[113] Albrecht, M G Creighton, J A *J Am Chem Soc* **1977**, *99*, 5215

[114] Kneıpp, K Wang, Y Kneıpp, H Itzkan, I Dasarı, R R Feld, M S *Phys Rev Lett* **1996**, *76*, 2444

[115] Tessıer, P M Velev, O D Kalambur, A T Rabolt, J F Lenhoff, A M Kaler E W *J Am Chem Soc* **2000,** *122,* 9554

[116] Felıdj, N Aubard, J Levı, G Krenn, J R Schıder, G Leıtner, A and Aussenegg, F R *Phys Rev B* **2002,** *66*, 245407

[117] Felıdj, N Aubard, J Levı, G Krenn, J R Hohenau, A Schıder, G Leıtner, A Aussenegg, F R *Appl Phys Lett* **2003**, *82*, 3095

[118] Abdelsalam , M E Bartlett, P N Baumberg , J J Cıntra, S Kelf , T A Russell A E *Electrochemıstry Communıcatıons* **2005**, *7*, 740

2.1 Introduction

The aim of the work is to fabricate nanoporous gold electrodes of controllable structure and texture Two routes have been followed to accomplish this result

- production of porous electrodes
- deposition of gold black electrodes

From an experimental point of view, several issues are essential to deal with

1 the selection of an appropriate protocol for making the substrate sufficiently hydrophilic to prevent detachment of the template from the substrate before deposition within the interstitial voids
2 the electrodeposition conditions

2.2 Apparatus

All electrochemical experiments were carried out in a standard three-electrode cell at room temperature using CH electrochemical workstations (potentiostats) A potentiostat requires an electrochemical cell with three electrodes a working electrode, a counter electrode (platinum net or spiral immersed in electrolyte) and a Ag/AgCl (sat) reference electrode Fluorine-doped tin oxide (FTO) coated glass (Hartford Glass Inc), a gold disk (3mm diameter) or gold bead electrodes were utilized as working electrodes Scanning electron microscopy was carried out using a the Hitachi S-3000N scanning electron microscope Optical measurements were obtained using a UV/VIS spectrometer Raman spectroscopy measurements were performed on a Horiba-Jobin YVON HR800 UV Raman spectrometer

2.3 Reagents and Solutions

Milli-Q water was used throughout in all solutions and rinsings The FTO etching solution was Hydrogen peroxide (Sigma Aldrich) Sulphuric acid (Sigma Aldrich) (20 80) Cyanide free gold plating bath Techni Gold 25 containing gold sulfite (Technic Inc) and solutions of 0 01M $NaAuCl_4 \cdot 3H_2O$ (Sigma Aldrich) in 0 5M H_2SO_4 (99 999%, Sigma Aldrich), 0 01M $NaAuCl_4 \cdot 3H2O$ (Sigma Aldrich) in 0 1M KCl (Sigma Aldrich) were used for electrochemical depositions Techni Gold 25 was chosen for performing templated electrodeposition due to its stability (presence of additives and stabilizing agents) and relatively low cost while tetrachloro-aurate was preferred as precursor for investigating the effect of additives on nucleation and growth in order to avoid any interference between stabilizing agents and growth inhibitors The additives 0 5mM KI (Sigma Aldrich), 0 5mM Mercapto-ethanol (C_2H_4SHOH, Sigma Aldrich) and 0 5mM Lead Acetate [$Pb(C_2H_3O_2)_4$, Sigma Aldrich] were added to the tetrachloro-aurate solution as required 5mM 11-Mercapto-Undecanol ($C_{11}H_{24}OS$, Sigma Aldrich) in ethanol was used as the marker molecule (stock solution) for Transmission-Surface Plasmon Resonance (T-SPR) measurements The SERS probe was Trans-1,2-bis(4-pyridyl)ethylene ($C_{12}H_{10}N_2$, Sigma Aldrich) in methanol Methanol, ethanol and acetonitrile (all spectroscopic grade) were obtained from Sigma Aldrich

2.4 The substrate: Fluorine-doped Tin Oxide (FTO) on glass slide

Transparent Conducting Oxide thin films of semiconducting materials, such as Tin oxide TO (SnO_2), Indium-doped Tin oxide (ITO), Fluorine-doped Tin oxide (FTO, SnO_2 F) and Antimomum-doped Tin oxide (ATO, SnO_2 Sb) are finding wide range of device applications, thanks to their useful electrical, optical and chemical properties The Fluorine-doped Tin Oxide (FTO) is an n-type and wide band gap semiconductor and has the following properties

1 high transmittance in the visible
2 high reflectivity in the infrared region
3 excellent electrical conductivity

4 good carrier mobility

5 good mechanical and thermal stability

FTO glass slides, purchased from Hartford Glass Co Inc , have been used in the present project as substrates and thus utilized in dip-coating and electrochemical techniques Beyond the properties of the conducting film, the substrate itself presents some noteworthy features that have been taken into account and have supported it In fact, the choice of FTO on glass slides is motivated by the following reasons

- the low cost, roughly 0 09€ per electrode
- the flatness of the substrate and the possibility to fabricate easily samples whatever the required size and shape is these features are useful and essential for materials to be characterized with SEM, optical and Raman techniques since they can be easily and safely placed in SEM microscopes and optical instruments stages, cuvettes, dip-coating probes where most commonly used commercial electrodes would not fit
- the relatively good smoothness of the FTO layer on the glass slides the average size of the grainy FTO crystallites, being much smaller compared with the polystyrene latex beads nanospheres diameter, does not significantly affect the quality of the closed-packed array achieved by self-assembly process of the template

FTO glass electrodes were prepared by rinsing in water, then in acetone Next they were heated to 400° C for 10 minutes to remove all the contaminants from the surface, then dipped in etching solution (piranha bath, a 3 1 or 4 1 mixture of H_2SO_4 conc and H_2O_2) to make them hydrophilic Finally, they were rinsed in water then kept FTO side up in Petri dishes to minimise their exposure to the environment and to avoid contamination

2.5 Preparation of latex polystyrene opals

The first step in the fabrication of a nanoporous electrodes is self-assembling the template nanospheres into close-packed arrays The options for fabricating opaline structures with accessible instrumentation are

1 sedimentation or substrate dipping
2 dip-coating technique

In spite of its simplicity, the first approach require a humidity-controlled chamber for slowing and maintaining constant the evaporation rate Moreover, the preparation of a sample is very time-consuming as it takes roughly 12-24 hours

The dip-coating method on the contrary allows to be produced samples in much shorter time (20-60 minutes) and to control the film thickness by setting properly withdrawal speed and acceleration

Therefore, latex polystyrene opals were fabricated using the dip-coating technique by slowly withdrawing hydrophilic FTO glass slides from a 2-10% (w/w) nanospheres suspensions with feedrate and acceleration ranging from 0 001 to 0 006 mm s^{-1} and from 0 003 to 0 018 mm s^{2} respectively

2.6 Preparation of Au-Nanostructure Modified FTO Electrodes

Gold electrodeposition plays a key role since the quality and the texture of the materials depend on this technique The objectives are maximising the density of nuclei and minimizing the crystallites size, aiming to fabricate gold blacks

The electrodes were modified by electrodeposition of gold onto the FTO surface One half of the FTO electrode was covered using Teflon tape to control the area of the working electrode in the electrolyte The exposed half of the FTO electrode was immersed in the electrolyte solution The deposition conditions applied to the electrodes are summarised in Table 3 6 All electrolyte solutions were degassed by bubbling with nitrogen for at least 10 minutes before deposition began

Table 2 1 Summary of Electrodeposition Conditions on FTO Electrodes

Electrolyte Solution	Additive	Deposition Potential Programme	Charged passed
0 01M $NaAuCl_4 \cdot 3H_2O$ + 0 5M H_2SO_4	None	amperometric I vs t at -0 4V and -0 5V	250mC cm^{-2}
0 01M $NaAuCl_4 \cdot 3H_2O$ + 0 5M H_2SO_4	5mM KI	amperometric I vs t at -0 1V, -0 3V, -0 4V and -0 5V	250–500 mC cm^{2}
0 01M $NaAuCl_4 \cdot 3H_2O$ + 0 5M H_2SO_4	5mM KI	multipulse +0 9V (5s), -0 4V (5s) and +0 9V (5s), -0 4V (2 5s)	10 cycles
0 01M $NaAuCl_4 \cdot 3H_2O$ + 0 5M H_2SO_4	5mM Lead Acetate	amperometric I vs t at -0 4V and -0 5V	250–500 mC cm^{2}
0 01M $NaAuCl_4 \cdot 3H_2O$ + 0 5M H_2SO_4	5mM Mercapto-ethanol	amperometric I vs t at -0 1V, -0 2V, -0 3V, -0 4V and -0 5V	250–500 mC cm^{2}

Following deposition, the electrodes were rinsed with water to prevent further deposition from the electrolyte solution and the electrodes were stored in Petri dishes until they were characterised

2.7 Preparation of Au-Nanostructure Modified Gold Bead Electrodes

Gold bead electrodes were flame annealed in a highly refined butane flame until they were seen to melt, then they were allowed to solidify again This process, which forces all the impurities to migrate towards the surface of the gold bead, was repeated until the bead surface appeared clean to a mirror finish and uniform Next the beads were electropolished twice in 0 5 M H_2SO_4 by applying a +3 0 V potential difference between a Pt spiral counter electrode and the gold bead until the gold bead turned red (indicating a gold-oxide layer had formed) The red oxide layer was then dissolved in 1M HCl to reveal the clean gold underneath The beads were then electrochemically cleaned by cycling them between 0 0V and +1 45V in 0 5M H_2SO_4 solution (degassed by bubbling with argon for 10 minutes) In this case the Ag/AgCl (sat) electrode was protected by a salt bridge from the electrolyte solution as any chloride ions in the electrolyte would have contaminated the bead surface

Finally, the gold bead electrodes were modified according to the protocol listed in the table below For comparison purposes a gold disk electrode was also electrochemically roughened The gold disk electrode was mechanically polished using a slurry of 0 3μm Al_2O_3 particles and ultrasonically cleaned in water before being electrochemically cleaned in 0 5M H_2SO_4 using the same method as that performed on the gold beads The gold disk electrode was not flame annealed All electrolyte solutions were degassed by bubbling with argon for at least 10 minutes before performing deposition

Table 2 2 Summary of Modification Conditions for Gold Bead Electrodes

Electrode	Modification	Electrolyte	Potential Programme	Charged passed
Bead 1	Electrodeposition	0 01M $NaAuCl_4$ $3H_2O$ + 0 1M KCl	Amperometric I vs t at -0 4V	250mC cm^{-2}
Bead 2	Electrodeposition	0 01M $NaAuCl_4 \cdot 3H_2O$ + 0 1M KCl	Amperometric I vs t at -0 4V	500mC cm^{-2}
Bead 3	Electrodeposition	0 01M $NaAuCl_4 \cdot 3H_2O$ + 0 5M H_2SO_4 + 0 5mM KI	Amperometric I vs t at -0 4V	250mC cm^{-2}
Bead 4	Electrodeposition	0 01M $NaAuCl_4 \cdot 3H_2O$ + 0 5M H_2SO_4 + 0 5mM KI	Amperometric I vs t at -0 4V	500mC cm^{-2}
Bead 5	None	-	-	-
Bead 6	Roughening	0 1M KCl	750mV s^{-1} between -0 3V & +1 2V	20 cycles
Disk 1	Roughening	0 1 M KCl	750mV s^{-1} between -0 3V & +1 2V	20 cycles

2.8 Preparation of Gold nanoporous electrodes

Gold nanoporous electrodes were prepared by electrodepositing gold within the interstitial voids using overpotentials ranging from -0 9 to -1 0 V vs Ag/AgCl sat reference electrode and removing the template Electrodeposition time was adjusted in a range between 50 and 100 s, depending on the electrode surface area, for producing both mono- and multilayer nanostructures The electrodes were then rinsed with MilliQ water, dried, dipped for 10-20 seconds in tetrahydrofuran (THF) to dissolve and remove the template and stored in Petri dishes

Latex polystyrene opals

3.1 Characterisation using Scanning Electron Microscopy (SEM)

Scanning Electron Microscopy was utilized for the investigation of the morphology of the opaline structures, the size of gold crystallites and nanostructures The objectives are

1 probe the packing of the nanospheres and, after electrodeposition, of the nanoporous structure
2 compare the features of samples obtained by systematically varying electrodeposition conditions (potential, time, additives, etc)
3 discover the optimal conditions for fabricating gold blacks

Opals are characterised using scanning electron microscopy This technique allows the quality of the close-packed arrays to be investigated Electrodes for imaging in the scanning electron microscope were imaged at an accelerating voltage of 20-25kV The working distance was 13mm and the beam current was varied between 25-50 amps Images were captured using magnifications ranging from 500 to 70,000 Although the dip-coating approach represents a powerful method to prepare good quality opals, the presence of defects might not be completely avoided The SEM characterization was particularly useful to study the morphology of the coated substrates and identify point, line and plane defects The photonic crystalline structures obtained were stable and only in the case of 240nm diameter nanospheres evidence of detachment of the of the opaline layer from the FTO electrode was noticed the re-suspension of the latex beads occurred as the coated FTO glass slides were dipped in the electroplating bath The reasons of the instability are related to the inverse proportionality between the number of defects and microsphere diameter the small the diameter, the higher the number of defects Figure 3 1 displays the presence of point, line and plane defects in 240nm diameter photonic crystals

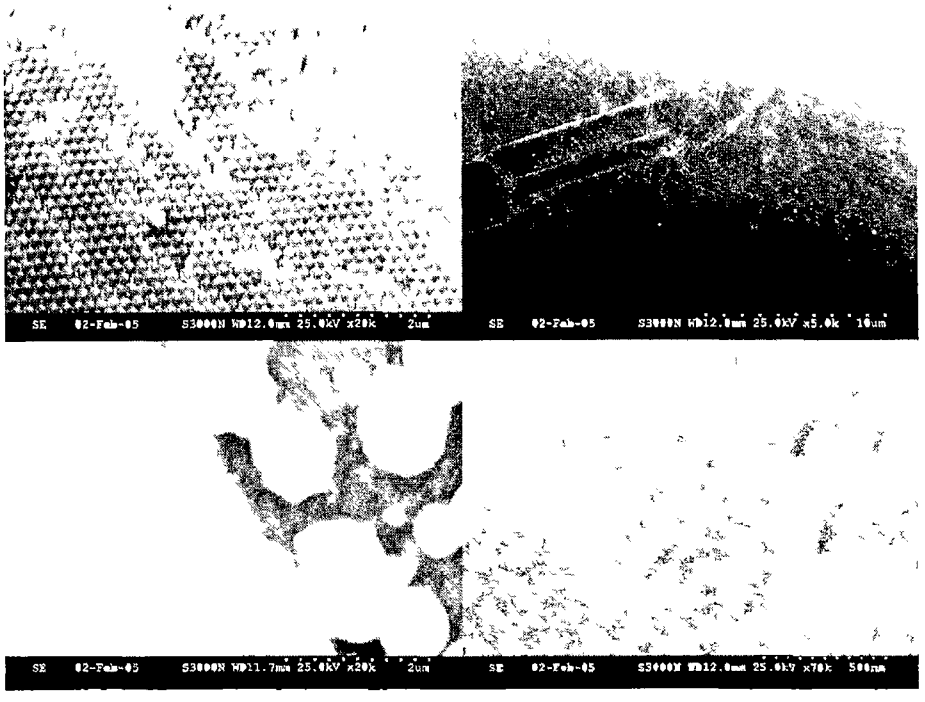

Fig 3 1 SEM micrographs of 240 nm latex polystyrene opals at different magnifications (dip-coating settings feedrate= 0 03 mm s^{1}, acceleration= 0 09 mm s^{2}, SEM settings working distance=12 0 mm, accelerating voltage=25 kV)

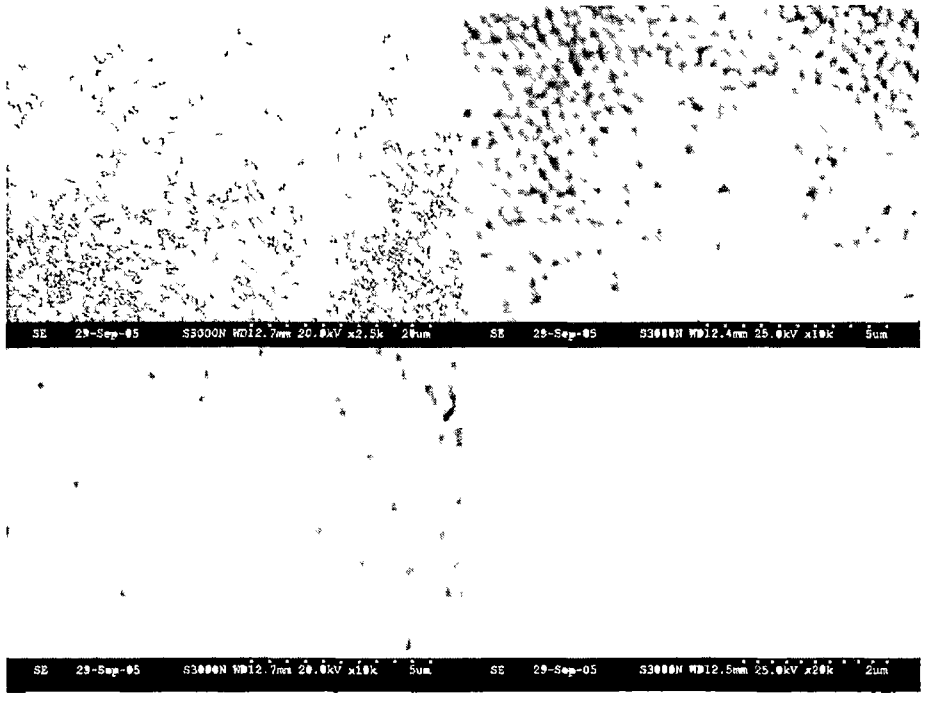

Fig 3 2 SEM micrographs of 430 nm latex polystyrene opals at different magnifications (dip-coating settings feedrate= 0 03 mm s^{1}, acceleration= 0 09 mm s^{-2}, SEM settings working distance=12 0 mm, accelerating voltage=25 kV))

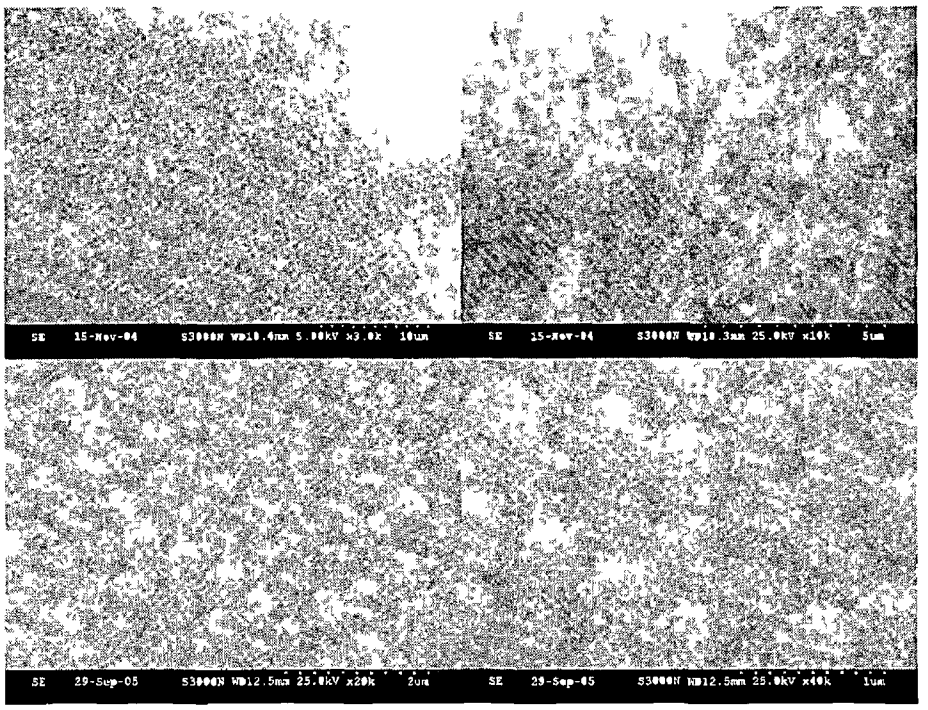

Fig 3 3 SEM micrographs of 600 nm latex polystyrene opals at different magnifications (dip-coating settings feedrate= 0 03 mm s^{-1}, acceleration= 0 09 mm s^{2}, SEM settings working distance=12 0 mm, accelerating voltage=25 kV))

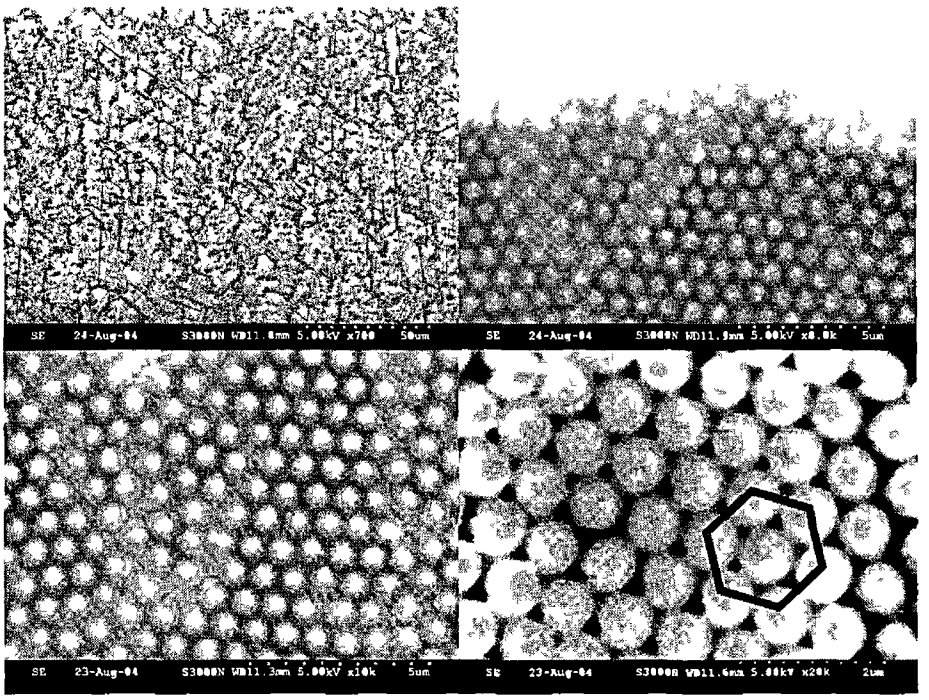

Fig 3 4 SEM micrographs of 820 nm latex polystyrene opals at different magnifications (dip-coating settings feedrate= 0 03 mm s^{1}, acceleration= 0 09 mm s^{2}, SEM settings working distance=12 0 mm, accelerating voltage=25 kV))

Figures 3 1, 3 2, 3 3 and 3 4 show hexagonally (hcp) and tetragonal close packed (square symmetry, which is analogous to the (1 0 0) plane of a fcc lattice) domains as well point and line defects Chung et al [1], using a capillary enhanced sedimentation method, confirmed the theoretical prediction that the face-centered cubic (FCC) structure is favoured over the hexagonal close packed (HCP) structure [2,3] Figures 3 1, 3 2, 3 3 and 3 4 confirm the higher thermodynamic stable and thus slightly favoured with respect to the fcc array this is corroborated by experimental evidence The presence of either hcp or fcc domains however is not relevant for the aim of the present work since for both the lattice structures the packing factor is the same (0 74), hence the density of nanospheres and nanocavities is maximised

3.2 Optical diffraction

The opaline surfaces are strongly coloured, the precise colour depending on the viewing angle, void diameter and film thickness. Since the diffraction colour depends on the photonic crystal lattice constant, changing the distance between the nanospheres changes the colour. The following photographs display the optical response of a photonic crystal to transmittance and light scattering respectively.

Fig. 3.5 Photographs of the same sample of photonic crystal (hcp array confirmed by SEM Micrographs - Left: transmitted light, Right: light scattering)

For the (111) plane, lattice constant d_{hkl} coincides with d_{111}, which is the interplanar spacing of fcc (111) planes, and n_{eff} is the effective refractive index of the photonic crystal film, θ is the angle between the incident beam and the normal to the (111) plane, λ is the free-space wavelength of the light. The effective refractive index is also calculated from the equation for fcc structures:

$$n_{eff}^2 = n_a^2 f + n_b^2 (1 - f)$$

where n_a and n_b are the refractive indices of the PS nanospheres and the surrounding medium, respectively, f is the volume fraction of the PS nanospheres in the film and is approximately 74%, based on a perfect hexangular packing geometry of identical spheres, $n_a = 1.59$ (PS nanospheres) and $n_b = 1.0$ (air in the voids).

As the surface of our samples is predominated by (111) face, the lattice constant can be calculated according to the following equation

$$d_{111} = (2/3)^{1/2} D$$

where D is the diameter of the PS spheres

Accordingly, the reflection peak position calculated for each microsphere diameter is reported in the following Table

Nanospheres diameter (nm)	d_{111} (nm)	Peak wavelength (nm)
240	196	572
430	351	1025
600	490	1431
820	670	1956

In general, the m^{th}-order position of the Bragg diffraction peak λ_m can be calculated, once the fcc lattice is identified with the (111) face parallel to the substrate with the lattice constant D, incidence angle θ, volume fraction f, and effective refractive index n_{eff}, from the modified Bragg equation

$$m\lambda_m = 2d_{111}(n_{eff}^2 - \sin\ \theta)^{1/2}$$

From the modified Bragg equation the peak wavelength is expected to increase as the sphere diameter gets larger Unfortunately, the optical characterisation of the samples requires an instrument with beamspot size of few μm^2 in order to radiate a single domain and be able to obtain reasonably good spectra (i e ellispometer) which was unavailable Transmission measurement attempts using conventional UV-VIS spectrometers lead to complete absence of remarkable peaks or features since the domain size is smaller than the beamspot, the resulting signal is averaged on several different domains with different packing (hexagonal and tetragonal close packed arrays and few small random domains) and orientation, resulting in single domain bands overlapping

3.3 Determination of Electrode Surface Area

Another essential topic concerns the determination of the electrode surface area Electrodes with huge surface area such as roughened substrates or porous materials are extensively exploited for electrocatalysis and SERS Some of the substrates produced that are unsuitable for producing defect-free photonic crystals using small templates and maximising particle density may still have uses in producing substrates of large surface area for sensor (Liu et al [4]) or catalytic based applications (Pasquato et al [5])

The geometric surface area and the real surface area were determined in order to obtain informations on the roughness of the electrodes The so-called *geometric surface area* of the electrodes is defined as the projection of the real surface on a plane parallel to the macroscopic, visible phase boundary, that is, the electrode surface For the determination of the geometric surface area of the FTO glass electrodes a transparent ruler and an overhead projector were used The ruler was focused onto a sheet of A4 sized paper on the wall using the projector The area of the A4 sheet was measured using the projected scale of the ruler and this was noted Then without shifting the focus of the projector a FTO electrode was placed on the projector, and at the same position on the wall the projection of the deposited gold on the FTO electrode was traced onto a sheet of A4 paper Finally this shape was cut out and weighed, and its weight compared to the weight of a full sheet of A4 paper The relative weight of the cut-out compared to the A4 sheet was assumed to be equal to the relative area of that electrode compared to the projected area of the A4 sheet (on the wall) This process was repeated for all FTO electrodes and was found to be accurate within a 5% margin for error

Unlike the geometric surface area, the real surface area of an electrode takes into account the morphology of the surface of the electrode The meaning of real surface area depends on the method of measurement, on the theory of this method, and on the conditions of application of the method Hence, for a given system, various "real surface areas" can in principle be defined, although phenomena of surface reconstruction, relaxation and faceting, which often occur during adsorption or electrochemical measurements, should not be taken into account The most appropriate is the one

estimated using a method which best approaches the experimental situation to which the area determined is to be applied.

Besides the concept of real surface area, other aspects should be taken into consideration when dealing with solid electrodes:

1. surface topography (macro- and microroughness);
2. homogeneity/heterogeneity of the surface;
3. dispersion of the active material, including distribution law of the dispersed active material.

In conclusion, the simple concept of real surface area may be misleading if not related to the numerous other parameters which depend on the surface structure and determines the reactivity of an electrode surface.

The real surface area of gold bead electrodes, FTO electrodes and disk electrodes was determined using cyclic voltammetry by integrating the reduction peaks.

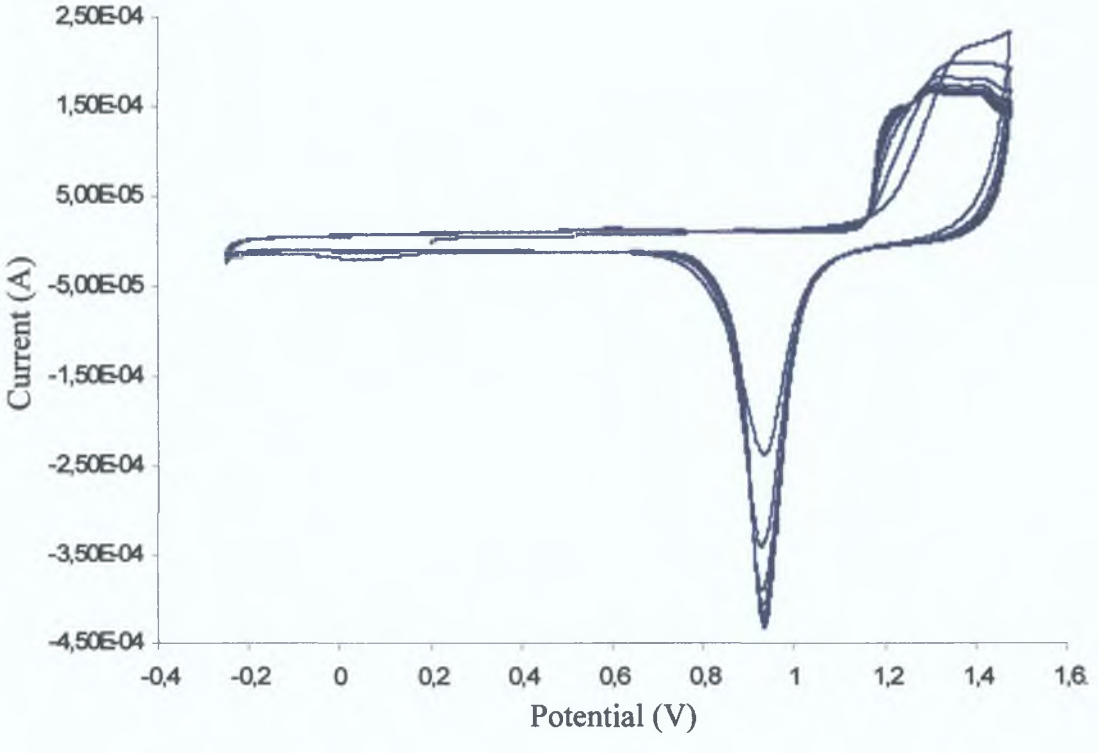

Fig. 3.6 Typical Cyclic voltammogram of a gold electrode in 0.5 M H_2SO_4 vs Ag/AgCl

Using the method described above for the cleaning of gold bead electrodes in 0.5M H_2SO_4 (degassed by bubbling with argon for 10 minutes) a metal-oxide monolayer forms and is subsequently reduced as a negative potential sweep is applied. The charge

passed during the reduction of this monolayer can be used to calculate the real surface area of the electrode using the specific charge density value reported in literature of 390 cm^2 This method was applied to each type of electrode The specific surface area was determined by dividing the real surface area by the mass of gold deposited during the electrochemical deposition (obtained by using Faraday's law Q = nFN to obtain the mass deposited from the charge passed during the deposition)

Determination of real surface area might be influenced by various factors Porous materials and oxide electrodes typically exhibit a current dependence on sweep rate due to exclusion of some less accessible surface at the highest rate The mechanism of charging of oxide electrodes is more complex than that of metals since it is also governed by pH through surface proton exchange The state of charge of a surface is thus dependent on the solution pH Therefore, the determinations should at least be normalized to a reference pH However, the method has no universal and no comparison is quantitatively possible between different oxides since the physical meaning of the charge may change in the different cases The comparison of capacitance values between different oxides is also partially affected by the fraction of surface sites being oxidised or reduced in a given potential range, which may differ for different systems On the contrary, this method is useful for an internal comparison for a given material, being the technique normalized to reproducible experimental conditions (i e pH, electrodeposition settings, apparatus) and hence all these effects can be reasonably neglected

A parameter for establishing the efficiency of the deposition method is represented by the so-called specific surface area This is a measure of the real surface area per gram of electrodeposited gold Current efficiency is a measure of the relative amount of charge consumed that actually results in deposition of gold atoms A process involving the transfer of one mole of electrons has a 100 % current efficiency if it results n the formation of one mole of electrodeposited atoms

Dealing with the precursors used for electrodeposition, $AuCl_4$ can undergo the following reactions at the electrode

$AuCl_4 + 2e \rightarrow AuCl_2 + 2Cl$ (side reaction)

$AuCl_4 + 3e \rightarrow Au(s) + 4Cl_4$ (electrodeposition)

This side reaction (as well as others that may occur at the electrode depending on the electrolyte make-up) consumes charge and therefore affects the current efficiency In

order for specific surface area measurements to be comparable it must be assumed that current efficiency for each deposition is approximately equal so this is a likely source of error

Using gold sulfite as precursor (Techni Gold 25 plating bath TG-25 RTU), the following reaction takes place

$$[Au(SO_3)_2]^3 + e \rightarrow Au(s) + 2SO_3^2$$

However, both in the case of $AuCl_4^-$ and $[Au(SO_3)_2]^3$ there are side reactions involved and therefore it is not possible to determine the current efficiency

The main advantage of using the Techni Gold 25 plating bath (TG-25 RTU) regards the presence of several additives which allow gold to be electrodeposited at significantly lower potentials than those found for simple salts

3.4 Electrode kinetics and Growth rates

As previously mentioned at page 44, the Current-time transients (CTT), obtained in Chronoamperometry by stepping the potential, are particularly useful to understand the kinetics of nucleation and growth. Figure 3.7 illustrates the CTT curves obtained at different potentials ranging from -0.90 to -0.98V vs Ag/AgCl reference electrode.

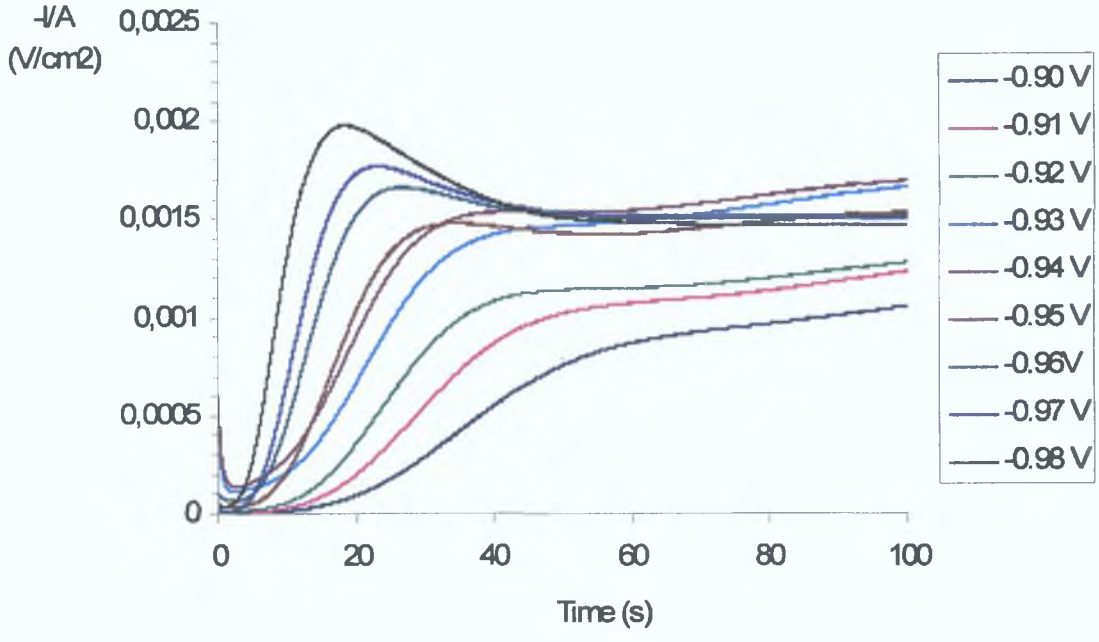

Fig. 3.7 Current-time transient obtained at potential ranging from -0.90 to -0.98 V vs Ag/AgCl reference electrode

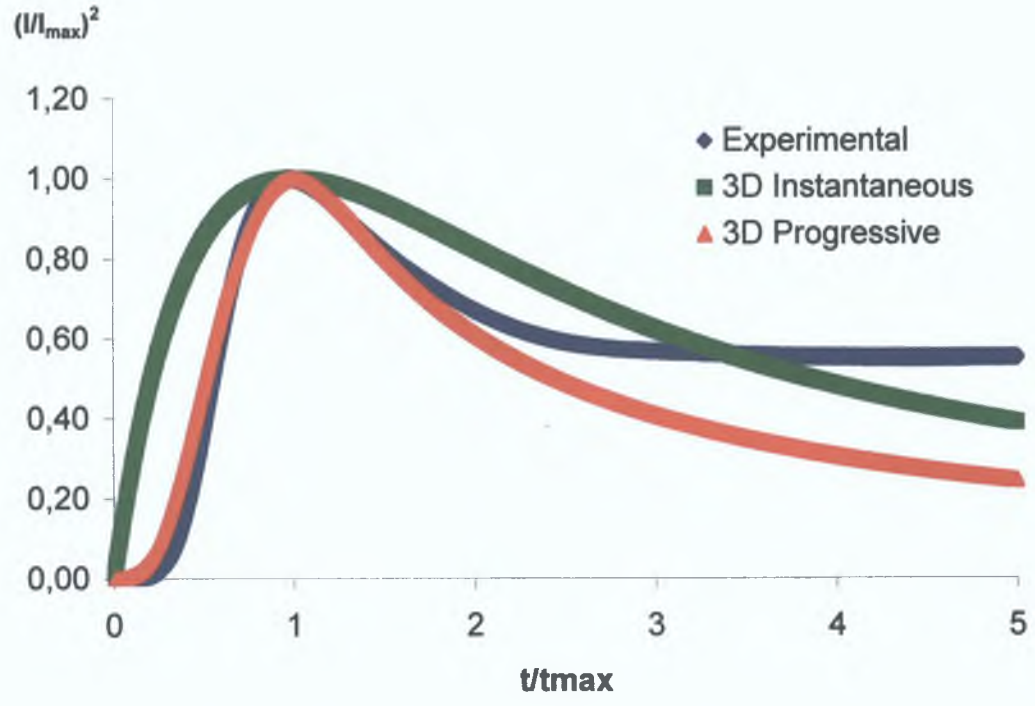

Fig. 3.8 Dimensionless plot displaying experimental, 3D instantaneous and 3D progressive nucleation

By comparing the experimental curve at highest overpotential (-0.98 V) with the plots of the models proposed by Scharifker and Hills[6], the nucleation process in its early stages clearly follows the progressive mechanism: in fact, while t_{MAX} is in good agreement with the experimental value (18±1s range) both for instantaneous and progressive nucleation, the shape of the dimensionless plot, in particular in the t/t_{MAX} range between 0 and 2, is fit only by the theoretical curve predicted for progressive nucleation (Eq. 15):

$$(I/I_{MAX})^2 = \frac{1.2254}{(t/t_{MAX})}\left\{1-\exp[-2.3367(t/t_{MAX})^2]\right\}$$

However, the plateau observed at higher values of t/t_{MAX} indicates that either all nucleation sites have been occupied or that remaining nucleation sites have been screened by the expanding diffusion fields around existing nuclei.

3.5 Characterisation Using Scanning Electron Microscopy

Electrodes were imaged in the scanning electron microscope at an accelerating voltage of 20-25kV The working distance was 10mm-13mm and the beam current was varied between 25-50 amps Images were captured using magnifications ranging from 500 to 70,000 Elemental analysis was also performed on some samples using the energy dispersive x-ray analysis (EDX) accessory on the scanning electron microscope For this a working distance of ~15mm was used and a beam current of 60 amps When comparing SEM images the deposition time is often used as a measure of the extent of a deposition for comparison purposes Charge consumed could equally be used instead of deposition time, however it was decided to use deposition time as this is more easily measured

3.6 Investigation of the Effect of Additives

Mercapto ethanol, potassium iodide and lead acetate were tested as inhibitors, aiming to quench the growth of the crystallites, minimize their size and therefore create gold blacks Assuming 100% efficiency, the charge passed (per unit geometric area of FTO electrode) was taken as an indication of the deposition rate during each deposition The charge density was plotted against time for each of the deposition experiments

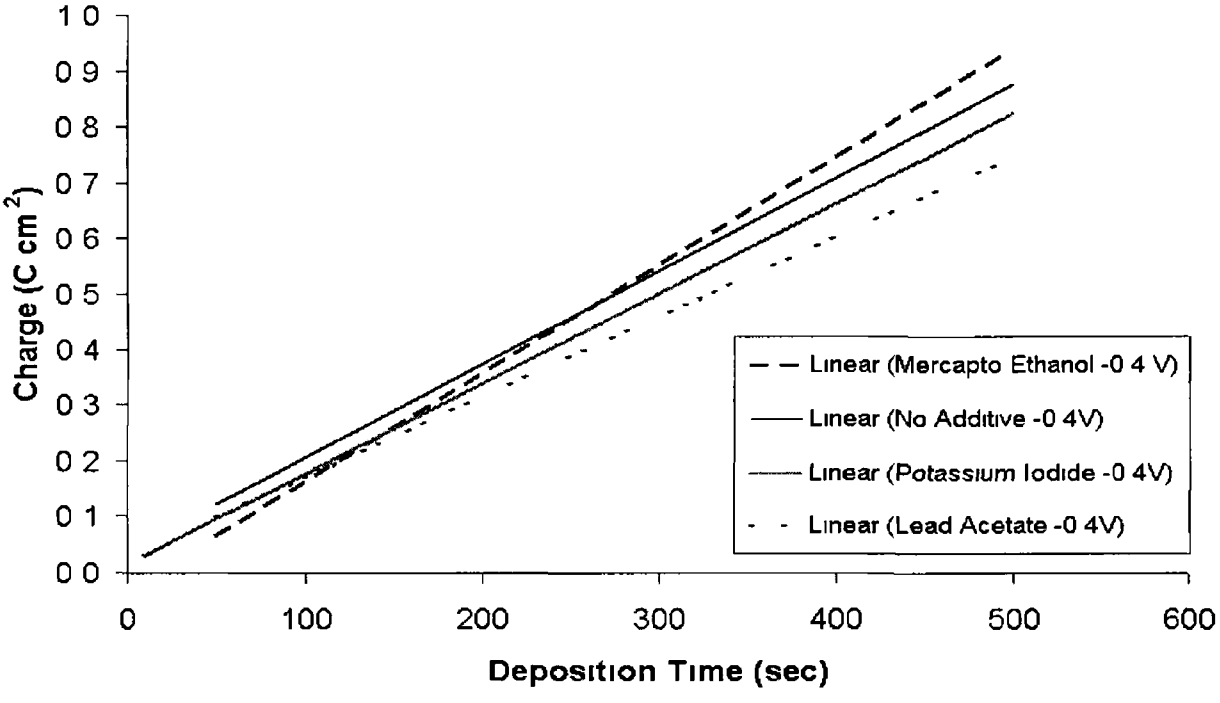

Fig 3 9 Charge Vs Time for gold deposition from $AuCl_4$ in the presence of different additives at overpotential –0 4V vs Ag/AgCl

It seems reasonable that by slowing the growth rate, an increased number of smaller nuclei can be obtained hence decreasing particle sizes and increasing particle density Thus an inhibitor capable of quenching the deposition rate is particularly suitable for this purpose The experimental data show that there is less charge consumed within the same time frame when potassium iodide and lead acetate are added to the electrolyte compared to when there is no additive present, indicating that there is less gold deposited in the presence of these additives when the same overpotential is applied

This proves that potassium iodide and lead acetate act as inhibitors to the deposition of gold from $NaAuCl_4$ solution Although the results are consistent with the expectation, the reagents do not inhibit significantly the growth of the crystallites This is possibly explicable because FTO is relatively rough with respect to substrates such as highly oriented pyrolytic graphite (HOPG) or mechanically end electrochemically polished flat metal surfaces used for model electrodeposition systems

Mercapto-ethanol is clearly not an inhibitor however as the data-points for it fall either side of the "No additive" trendline therefore from this data it is unclear what effect mercapto-ethanol has on the deposition of gold from $NaAuCl_4$ solution

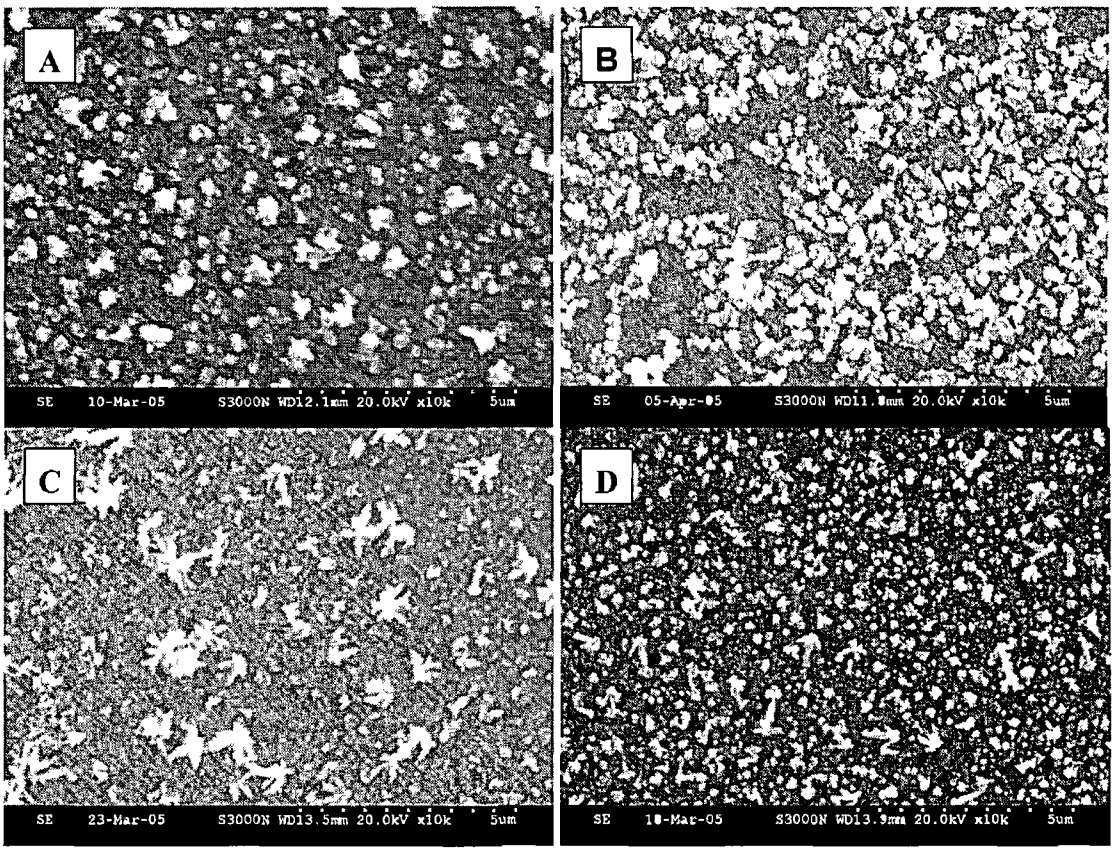

Fig 3 10 SEM Micrographs of Au deposited on FTO electrode from $NaAuCl_4$ solution for 50 seconds at –0 4V (10k magnification) (A) no additive, (B) Potassium Iodide 0 5mM additive, (C) Lead acetate 0 5mM additive, (D) Mercapto-ethanol 0 5mM additive

Analysis of the FTO electrodes under the scanning electron microscope allowed a more direct understanding of the effect of the additives on the deposition process Figure 3 10

and Figure 3 11 are typical SEM images obtained from this analysis Comparing Figure 3 10A and Figure 3 11A as expected increasing the deposition time results in an increase in particle density and also an increase in average particle size when all other conditions are kept constant When potassium iodide is added to the electrolyte (Figure 3 10B and Figure 3 11B) there is a significant increase in the particle density without a significant change in average particle size This is a very promising result as it suggests a significant increase in surface area per loading of gold which is one of the aims of this project Additionally the average particle size of 75-200nm found in the images is close to the size of particles quoted by Kalyuzhny et al [7] of 25nm-200nm gold particles for SPR and by Schwartzberg et al [8] of 5nm-50nm as the optimal conditions for SERS effects Therefore, it seems likely that these substrates, obtained at shorter deposition times, could be potentially suitable for SPR-based platforms (Type-A films) At much greater deposition times (>300 sec) multilayer gold coverage was seen (Type-B films)

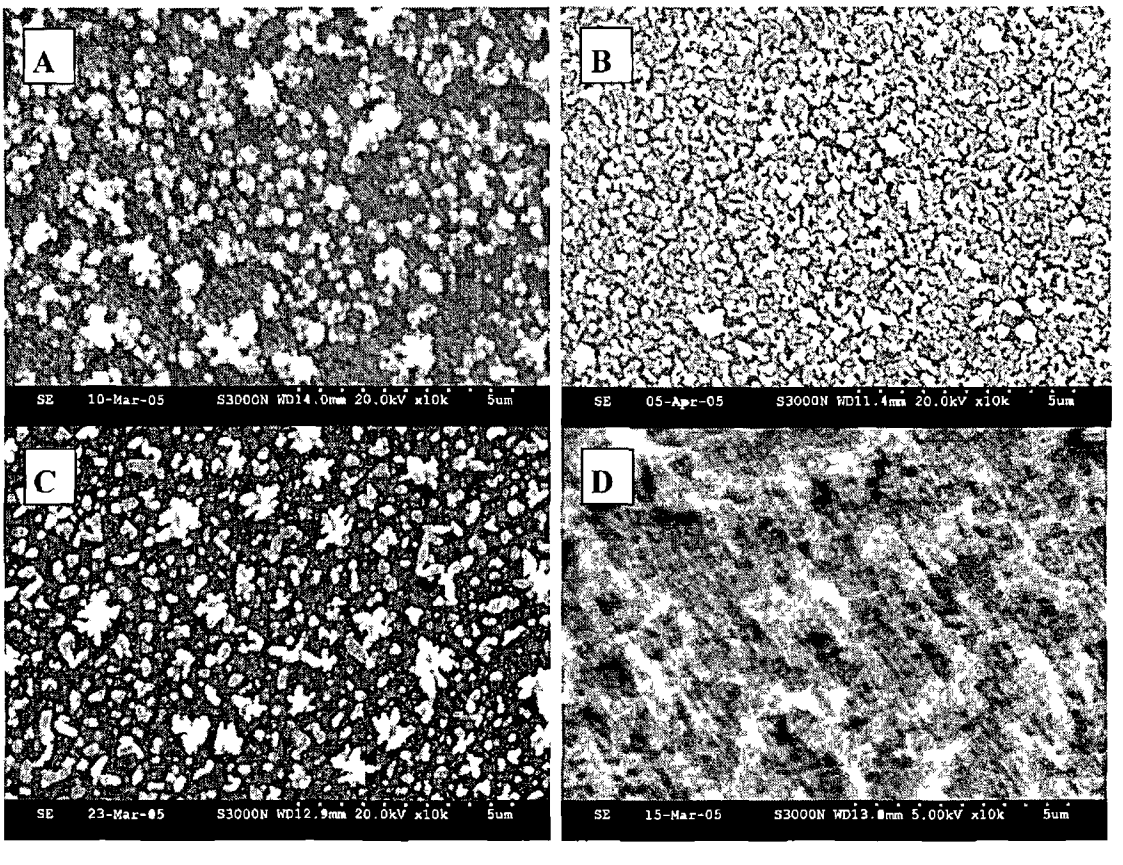

Fig 3 11 SEM Micrographs of AU deposited on FTO electrode from $NaAuCl_4$ solution for 100 seconds at –0 4V (10k magnification) (A) no additive, (B) KI additive (C) Lead acetate additive, (D) Mercapto-ethanol additive

The presence of lead acetate in the electrolyte appears to encourage aggregation of nuclei with a net effect of increasing the average particle size and decreasing the particle density (Figure 3 11C) This effect is less evident at the longer deposition time of 100 seconds and it appears that surrounding these larger aggregates there are many much smaller particles within the same size range as found when using iodide additive The non-uniformity and relatively low density of the particles produced in the presence of lead acetate make these substrates less ideal candidates for producing SERS and SPR type substrates However, the large aggregates may have increased surface area compared to deposition without additives making the substrates suitable for other applications such as catalysis and sensor development When the additive present was mercapto-ethanol the particle size was very small (50nm-100nm) with the exception of a few larger aggregates This only applied at low deposition times (<100 sec) and the particle density on these substrates wasn't significantly improved compared to those prepared with no additive Perhaps if a similar additive was used with a charged terminal group (e g COOH), the negative charge on the terminal group might encourage increased nucleation thus retaining the low particle size and increasing the particle density as found by El-Deab et al [9] Therefore, the use of a similar thiol linked additive could potentially produce substrates ideal for use in SERS and SPR applications particularly at lower deposition times At greater deposition times the gold particles aggregated to such an extent that there were no longer individual particles evident, this type of substrate may not be best suited to SERS and SPR applications but its increased surface area may prove useful for other applications

So far all substrates looked at have been type-A substrates, thin irregular gold films However, all of the observations made for this type of film have been shown to apply equally for the deposition of type-B irregular thick films This is demonstrated by Figure 3 12 where SEM images are displayed of FTO substrates produced by a longer deposition time (500 seconds) in the same deposition solutions as previous examples

SEM micrographs (Fig 3 10, 3 11 and 3 12) reveal with good reproducibility some dendritic crystallites in presence of $Pb(CH_3COO)_2$ independently of any deposition time while using the additives potassium iodide and Mercapto-ethanol these structures formed only at longer deposition times (500 s)

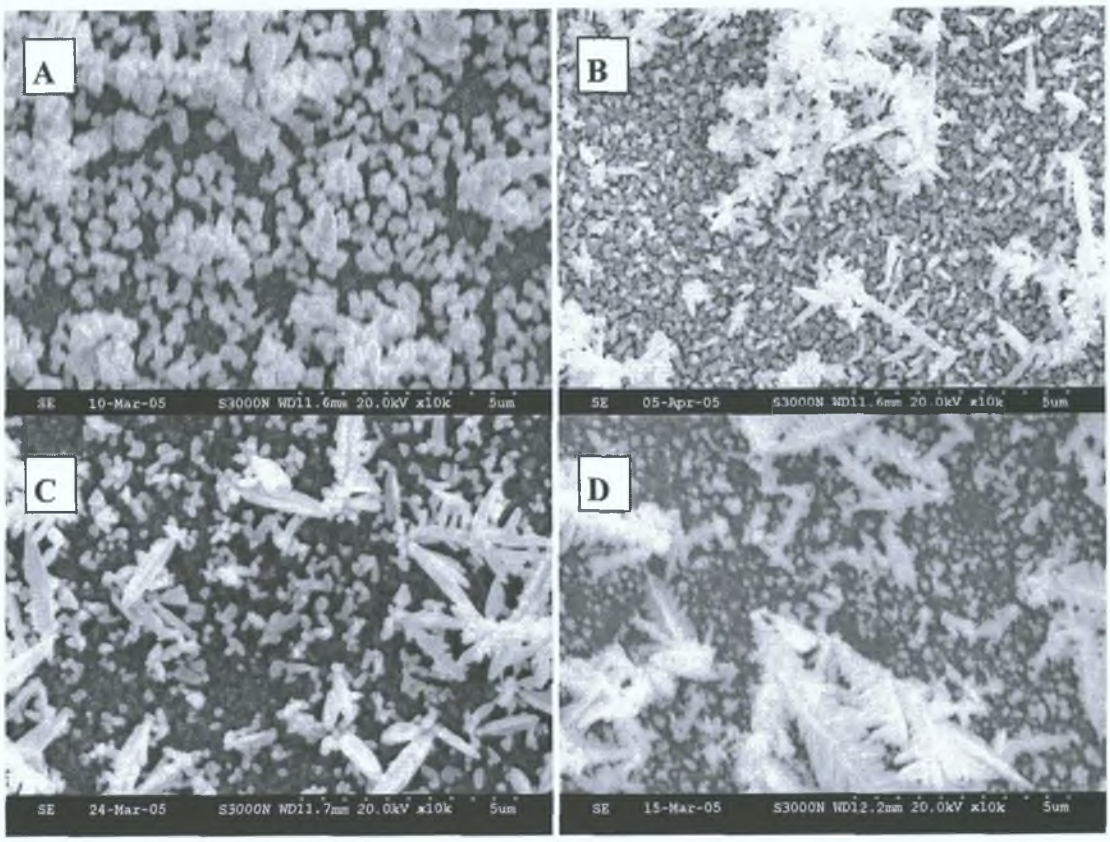

Fig. 3.12 SEM Micrographs of Au deposited on FTO electrode from $NaAuCl_4$ solution for 500 seconds at –0.4V (10k magnification) (A) no additive, (B) KI additive, (C) Lead acetate additive, (D) Mercapto-ethanol additive

3.7 Investigation of the Effect of Deposition Potential

The effect of deposition potential also plays an essential role on the quality of substrate obtained from the electrochemical deposition process. At potentials more negative than -0.5V Vs. Ag/AgCl sat) gas bubbles were observed coming from the working electrode, suggesting that side reactions were occurring at the electrode to remove the gases from solution. This would result in large amounts of charge being consumed that was intended to be used for the deposition of gold atoms and in much less stable gold films formation. Films fabricated in these conditions were more fragile and easily damaged during the post-deposition rinsing process suggesting that the evolving bubbles destabilised the gold nanoparticles on the FTO surface. The effect of using less negative potentials for the deposition was investigated when KI and mercapto-ethanol were the additives. Figure 3.13 shows the results obtained.

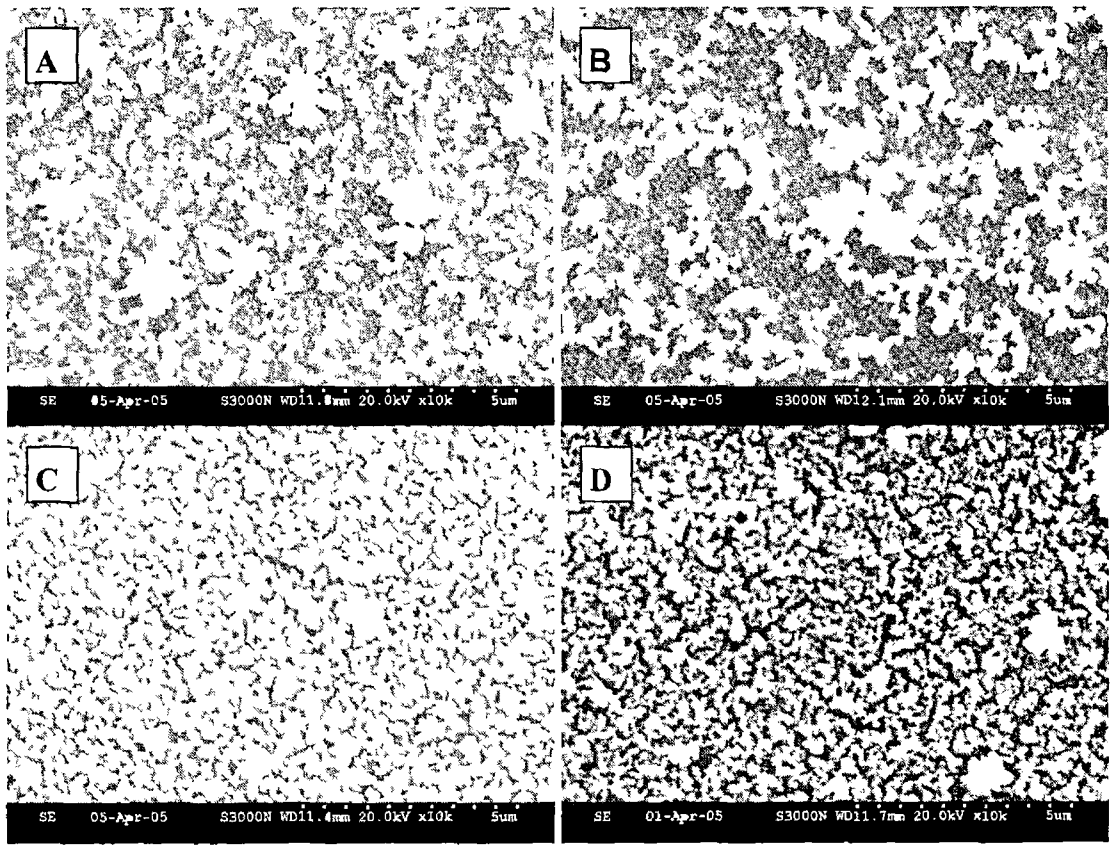

Fig 3 13 SEM Micrographs of AU deposited on FTO electrode from $NaAuCl_4$ solution for 100 seconds with KI additive (10k magnification) (A) at –0 1V, (B) –0 3V, (C) –0 4V, (D) –0 5V

The deposition potential does not significantly affect the average particle size of the deposits as the particle sizes in images A-D remains relatively constant, while the particle density depends on the deposition potential Figures A and B are significantly less dense than Figure C where the deposition potential was–0 4V Figure D appears less dense compared to Figure C suggesting that at –0 5V the deposition potential may be too negative and result in side reactions and less gold deposition This trend was confirmed when mercapto-ethanol was the additive On this base it appears the optimum deposition potential for the production of high density, low particle size, high surface area Au-nanostructures is approximately –0 4V (Vs Ag/AgCl sat)

3.8 Investigation of the Effect of Deposition Programme

In order to gain control over the electrodeposition process a multipulse deposition was performed. This involved applying a short pulse at –0.4V (for 2.5-5 sec) followed by a pulse at +0.9V, a potential at which no deposition is expected to occur: this procedure was repeated 10 times. The reasons behind this is that the "rest time" between growth pulses would allow time for the depleted $AuCl_4^-$ ions near the electrode to return to equilibrium concentrations, and it is believed that if the deposition process is limited to small pulses, then the nucleation process may be favoured with respect to the growth process as nucleation is the dominant process in the early stages of deposition.

Figure 3.14 shows the SEM micrographs obtained from this experiment. The multipulse deposition experiments are shown in Figure 3.14B and 3.14D and the equivalent single pulse deposition experiments (i.e. the same "deposition pulse" length keeping all other conditions the same) are shown in Figure 3.14A and 3.14C.

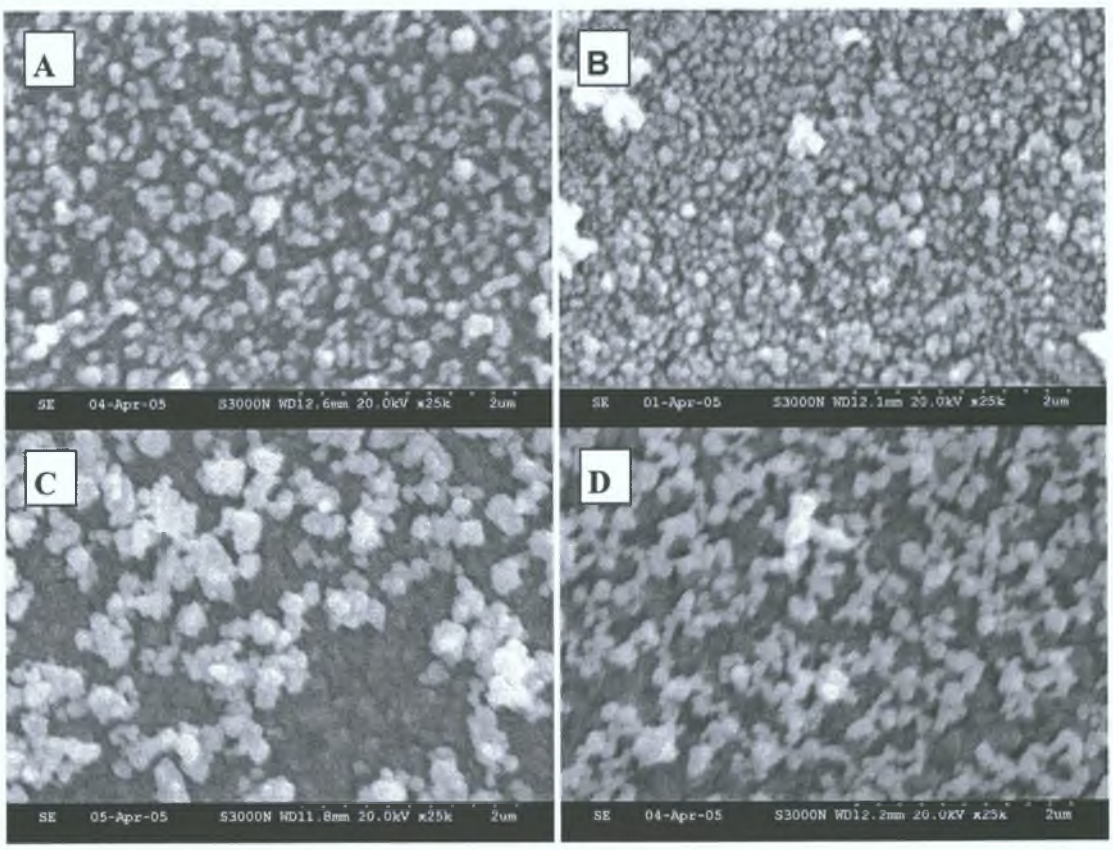

Fig. 3.14 SEM Micrographs of gold deposited on FTO electrode from $NaAuCl_4$ solution at –0.4V with KI additive (25k magnification) (A) following for 25 sec at –0.4V, (B) [2.5 sec at -0.4V, 5 sec at +0.9V] x 10 cycles (C) following for 50 sec at –0.4V, (D) [5 sec at -0.4V, 5 sec at +0.9V] x 10 cycles

From these images it can be seen that the multipulse experiments were a success as the particle size of the multipulse Au-nanoparticles are smaller and the particle density is greater. Most significant is the multipulse experiment at –0.4V for 2.5 seconds and +0.9V for 5 seconds x 10 cycles (see Micrographs above) where the average particle size was 50-150nm (which was the smallest particle size range achieved during the course of the project, with difference in results of one order of magnitude with respect to single pulse deposition). The fact that the length of this "deposition" pulse has such a clear reproducible effect on the resultant film morphology indicates that this technique could be further optimised to yield smaller, more dense particles. The results of SEM analysis indicate that multipulse deposition favours growth of smaller, more dense particles due to repeated nucleation.

3.9 Characterisation of Type-A Substrates

Preliminary tests have been performed in order to find the optimal conditions for the production of high density, low particle size, high surface area type-A (irregular thin film) Au-nanostructures from $NaAuCl_4$ on FTO have been determined. These substrates, which could be suitable for T-SPR applications due to their optical transparency and should yield strong SPR signals, are best produced using low deposition times (<100 sec), at a deposition potential of approximately –0.4V in a multipulse experiment and using the additive potassium iodide.

3.10 Determination of Electrode Surface Area

Data from the determination of surface area of FTO electrodes are collected in the Table below. Consistently with the expectations, deposits in the absence of additives had the lowest real surface area, specific area and ratio of real surface area to geometric surface area. This indicated that all of the additives used were successful in increasing the real surface area of the subsequent substrate. The substrates produced in the presence of the additive mercapto-ethanol had significantly increased specific surface area and ratio of real surface area to geometric surface area compared to those produced with no additive

in the electrolyte It is believed that a charged alkane-thiol group as the additive would be more successful at reducing the particle size and increasing the particle density and surface area of the deposited films as has been shown by El-Deab et al [9] who used cysteine as an additive

Table 3 15 Summary of Surface Areas of substrates produced by deposition at –0 4V for 50 seconds using $NaAuCl_4$

Additive	Au Load[a] (µg)	Real Surface Area (cm^2)	Specific Surface Area (10^3 cm^2 g^{-1})	Real Surface Area/Geometric Surface Area
None	39 98	0 40	9 96	0 77
Mercapto-ethanol	38 11	0 50	13 16	0 84
Potassium Iodide	40 06	0 65	16 26	1 03
Lead Acetate	37 09	0 61	16 35	1 12

The additives potassium iodide and lead acetate both yielded a significant increase in specific surface area and ratio of real surface area to geometric surface area In the case of potassium iodide, this was expected as it had already been observed that substrates deposited in the presence of potassium iodide had the smallest particle sizes and the highest particle density The substrates prepared in the presence of lead acetate additive were much less successful in achieving low particle size and high particle density therefore they would not necessarily have been expected to have high surface areas However, as suggested from the SEM images obtained of these substrates it was thought that the large aggregates of gold particles seemed to have quite complex shapes and therefore could have quite large surface areas This was confirmed through the surface area analysis It seems that these substrates could potentially be used for applications other than SERS and SPR based sensors such as a quartz crystal microbalance based sensor or catalysis

[a] Gold Load estimation assumes 100% current efficiency This is a likely source of error as 100% current efficiency is unlikely to occur

3.11 Characterisation Using Cyclic Voltammetry

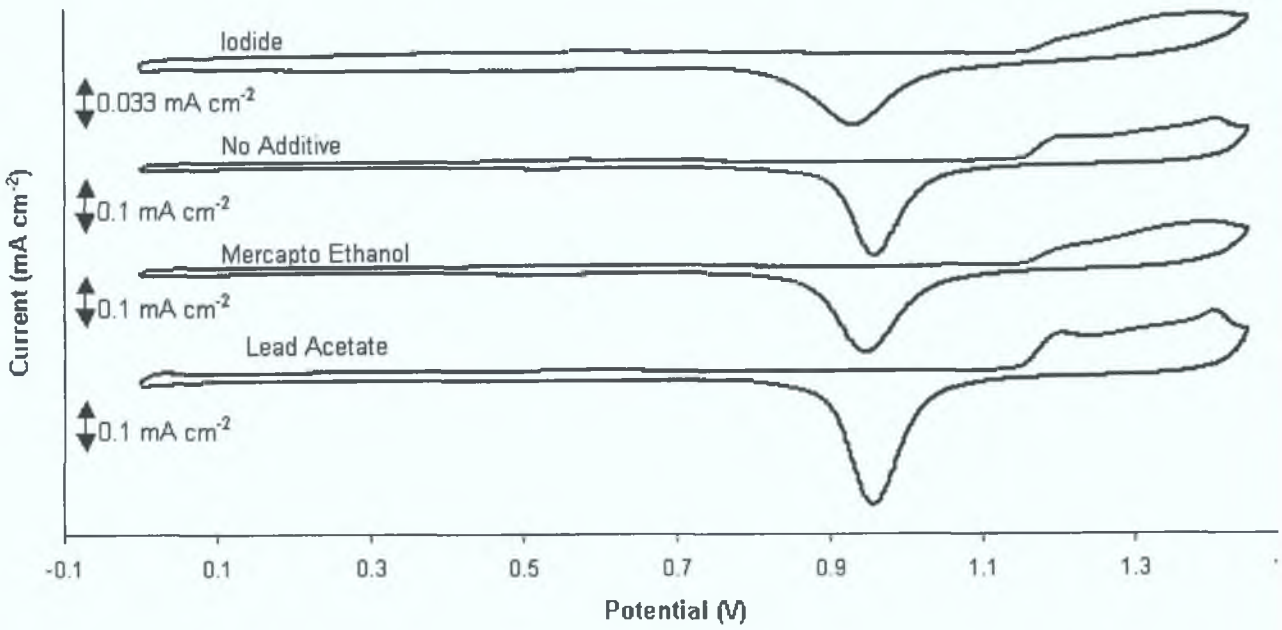

Fig. 3.16 Current potential curves of nano-Au FTO electrodes in a deoxygenated 0.5M H_2SO_4 solution at a scan rate of 50 mV s^{-1} deposited at –0.4V (Vs. Ag/AgCl sat) for 50 seconds

The cyclic voltammograms obtained from the cleaning and surface area determinations described above provide useful informations about the substrates. Analysing the shape of the peaks obtained for the gold oxide monolayer formation (+1.1V to +1.45V), two peaks are observed for the gold oxide monolayer. An explanation may be found in the possible presence of different crystallographic orientations of Au (Au(111). Au(100) and Au(110)) which exhibit different oxidation potentials and therefore give rise to peaks at different potentials or in the formation of various gold oxides of undefined stoichiometry.

The fact that the gold oxidation peaks has a different shape for the electrodes prepared using different additives suggests that the presences of these additives alters the crystallographic orientation of the deposits. As a comparison a CV of polycrystalline gold run under similar conditions is shown in the figure below.

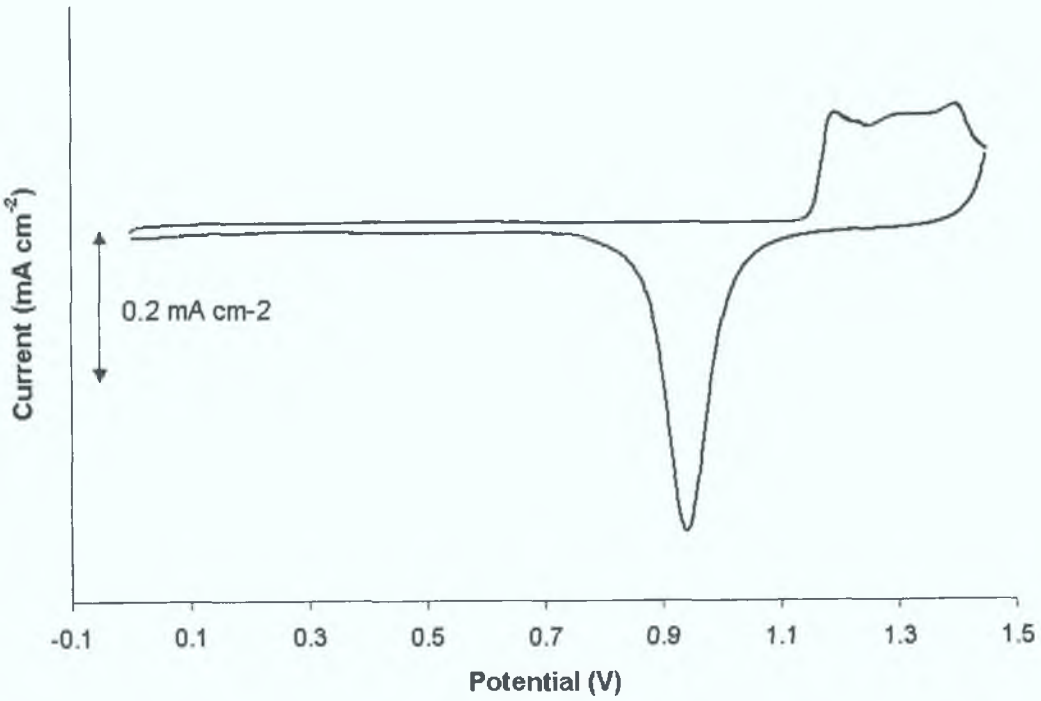

Fig. 3.17 Current potential curve of polycrystalline gold electrode in a deoxygenated 0.5M H_2SO_4 solution at a scan rate of 100 mV s^{-1}

3.12 Characterisation Using UV-Vis Spectrophotometry

Transmission UV-Vis spectrophotometry was performed on all nano-Au FTO electrodes in order to check for the presence of a surface-plasmon resonance band. Kalyuzhny et al.[13] reported a strong absorbance at 550nm on ultrathin gold island films formed by evaporation of gold onto quartz attributed to excitation of the surface plasmon. Continuous films of gold under similar conditions yielded only minimum absorbance sat 550nm, therefore evidence of strong absorbance at 550nm on the nano-Au FTO electrodes would suggest that the electrodes produced are successfully

displaying SPR effects Figure 3 18 contains some typical results from the scans performed

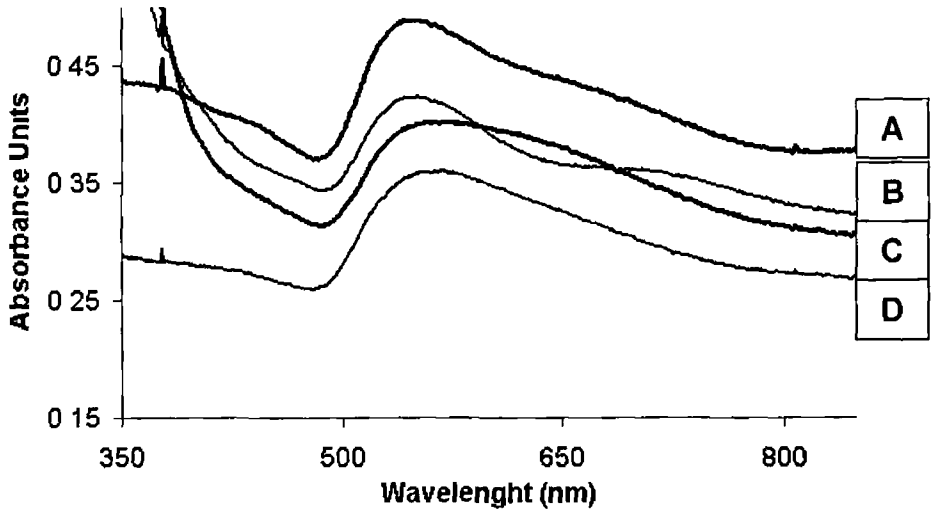

Fig 3 18 UV-Vis spectra of nano-Au FTO electrodes prepared from a 50 second deposition from $NaAuCl_4$ (A) with KI additive at –0 5V, (B) with no additive at –0 5V, (C) with lead acetate additive at –0 4V, (D) with mercapto-ethanol additive at –0 4V

It is clear from the spectra that there is a strong absorbance evident at 550nm, particularly on these thin gold films produced from a 50 second deposition This could be caused by a surface plasmon resonance signal

3.13 Characterisation of Type-B Substrates

From preliminary tests the optimal conditions for the production of high density, low particle size, high surface area type-B (irregular thick film) Au-nanostructures from $NaAuCl_4$ on FTO and on gold beads have been determined. These substrates are best produced using high deposition times ($\geq$200 sec), at a deposition potential of approximately –0.4V in a multipulse experiment, and using the additive potassium iodide. As optical transparency is not required of these substrates both FTO electrodes and gold bead electrodes have been investigated.

3.14 Determination of Electrode Surface Area

Table 3.19 Summary of Investigation of Gold Bead Surface Areas

Electrolyte	**Substrate**	**E_{DEP} (V)**	**Q_{DEP} ($C\ cm^{-2}$)**	**Area (cm^2) ± 0.001 cm^2**		**Roughness Factor[a]**
				Before	**After**	
$AuCl_4$+KCl	Bead 1	-0.4	0.250	0.11	0.32	2.94
$AuCl_4$+KCl	Bead 2	-0.4	0.500	0.09	0.57	6.46
$AuCl_4$+H_2SO_4+KI	Bead 3	-0.4	0.250	0.12	0.17	1.50
$AuCl_4$+H_2SO_4+KI	Bead 4	-0.4	0.500	0.09	0.33	3.55
Untreated	Bead	-		0.16	0.08	0.52
KCl	Roughened	-		0.16	0.13	0.86
KCl	Disk	-		0.11	0.13	1.25

The roughness factor of the gold bead electrodes used in this part of the project can be estimated, as gold is both the substrate and the deposited metal in the electrochemical depositions. The roughness factor is a measure of the increase in real surface area resulting from the electrochemical deposition/roughening procedure. The accuracy of this procedure in estimating the surface roughness factor is called into question by the

[a] Roughness factor = Area Before Roughening / Area After Roughening

estimation of a 0 52 roughness factor for the untreated bead This suggests that the surface area of the bead halved during the course of the experiment despite it not being modified electrochemically Possible sources of error in this measurement are changes in the depth of the bead in the electrolyte solution during surface area determination so that more or less of the bead was immersed each time

3.15 Characterisation using Raman Spectroscopy

Raman spectroscopy was performed on gold beads and FTO glass slides one had been electrodeposited in 0 01M $NaAuCl_4 \cdot 3H_2O$ + 0 5M H_2SO_4 + 5mM KI for 300 seconds at –0 5V deposition potential (Vs Ag/AgCl sat) The other FTO electrode had been deposited in 0 01M $NaAuCl_4 \cdot 3H2O$ + 0 5M H_2SO_4 (no additive) for 200 seconds at – 0 4V deposition potential (Vs Ag/AgCl sat) Raman spectroscopy was also performed on a roughened gold disk electrode All samples were immersed in 5mM trans-1,2-bis(4-pyridyl)ethylene (BPE) in methanol over three days in order to allow formation of a SAM on the gold surface according to the method used by Sauer et al [10] Before analysis using the Raman spectrometer samples were rinsed in fresh methanol so that only monolayer coverage of BPE on the gold surface was obtained The excitation wavelength used was 632nm In order to prevent damage to the sample the intensity of the excitation beam was kept low (<10mW) The spectrum was recorded between 200 cm^{-1} and 2200 cm^{-1} with each accumulation lasting 4 seconds and the average of 20 accumulations taken as the spectrum for each sample Each sample was scanned under the same conditions so that the relative SERS enhancement of each sample could be compared

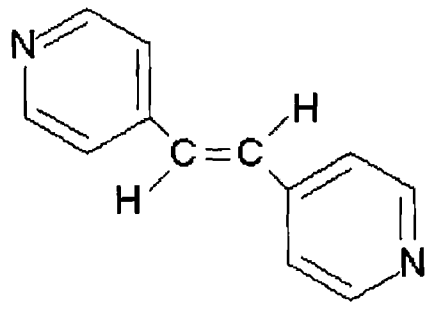

Fig 3 20 BPE molecule

The electrodeposited and roughened gold beads, a roughened gold disk electrode and two electrodeposited FTO electrodes were analysed using Raman spectroscopy Spectra were recorded for analysing the nano-Au modified gold beads that were modified in

0 01M $NaAuCl_4$ + 0 5M KCl at –0 4V (vs Ag/AgCl sat) as well as the gold disk electrode modified by electrochemical roughening in KCl electrolyte according to the procedure used by Stolberg et al [11] BPE has intense and characteristic Raman bands located at about 1200 cm^{-1}, 1340 cm^{-1}, 1610 cm^{-1}, and 1640 cm^{-1} due to in-plane ring modes The SERS enhancement factor was estimated by comparing the height of the band at 1640cm^{-1} for each sample to the height of the same band obtained from the analysis of a smooth (untreated) gold bead electrode (after an estimation of the baseline had been subtracted from each)

The Raman spectra proved that the roughened gold disk electrode was the most successful of the substrates in terms of SERS enhancement The estimated enhancement factor for this substrate was 271±1σ The intensity of the enhancement was found to be reproducible with a standard deviation σ of 10%

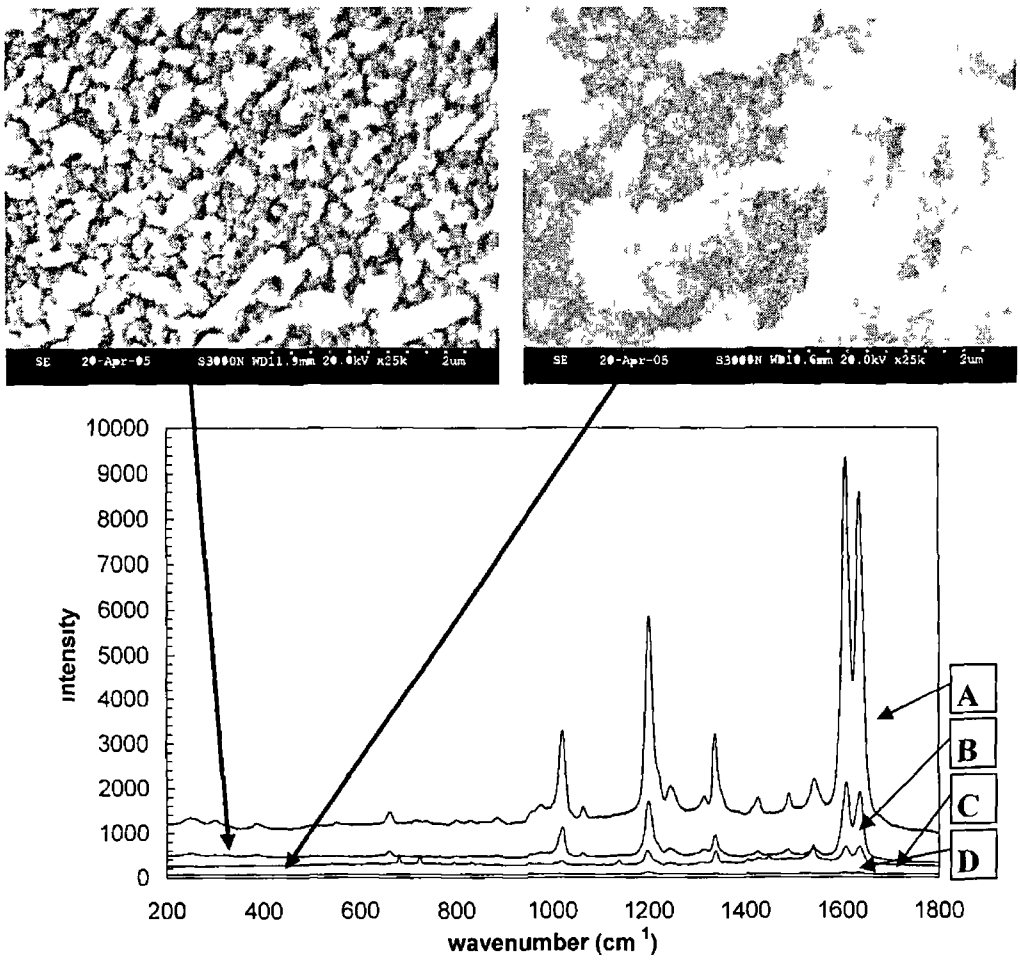

Fig 3 21 SEM images (25k magnification) and SERS spectra of Gold bead electrodes prepared (B) from $NaAuCl_4$ + KCl at –0 4V 250mC cm^2 deposition, (C) from $NaAuCl_4$ + KCl at –0 4V 500mC cm^2 deposition Compared against SERS spectrum of (A) roughened risk electrode and (D) smooth gold bead

The relative enhancement of the two beads modified by electrodeposition from tetrachloro-aurate + KCl solution is significantly smaller than that obtained from the roughened disk electrode (enhancement factors of 54±1σ and 15±1σ). It seems from this that the electrode produced with a deposition charge of 250mC cm^{-2} gave a much better SERS enhancement. This indicates that the deposition charge has a clear effect on the SERS enhancement therefore optimisation of deposition charge will be the next logical step in this area. Qualitatively the spectra are quite similar to each other and to the spectrum of the roughened disk electrode, although there is some variation of the relative intensity of bands within each spectrum. Examination of the SEM images of the SERS substrates reveals that it is the uniform height of the first gold bead that proved more successful at producing SERS effects compared with the large particle aggregates protruding from the surface seen in the second image. Perhaps it is the closely packed rough surface features of the first bead that contribute to the SERS enhancement compared to the more isolated aggregate features of the second bead. Apart from the large structures protruding from the surface on the second bead the size of the particles on the surface seems larger and they seem less dense compared to those on the bead that yielded greater SERS enhancements. This most likely also had an important influence on the SERS enhancement measured. It was considered if the surface roughness allowing for greater probe molecule loading was a factor in the enhancement obtained. However previously it was reported that the bead deposited with a charge of 250 mC cm^{-2} (enhancement factor 54±1σ) had a roughness approximately half that of the bead deposited with a charge of 500mC cm^{-2} (enhancement factor 15±1σ). It can be concluded therefore that if additional loading made possible by surface roughness influenced the measured enhancement factor then it was only to a very small extent, and particle size and density was more important. The intensity of the enhancement was found to be reproducible with a standard deviation σ of 10%.

Analysis of the beads modified by electrodepositing gold from 0.01M $NaAuCl_4$ + 0.5M H_2SO_4 + 0.5mM KI produced some similar trends as were found in the first samples. Again the enhancement factor was strongly influenced by the deposition charge, with the bead deposited at 250mC cm^{-2} yielding an enhancement factor of 39±1σ compared to an enhancement factor of 6±1σ when the deposition charge was 500mC cm^{-2}. Again it seems that when a greater charge was applied it reduced the enhancement factor significantly. These results suggest that the use of 0.1M KCl as the additive for deposition on gold beads yields better SERS substrates compared to those produced in

the presence of 0.5mM KI however further investigation is needed to confirm this as neither method has been optimised.

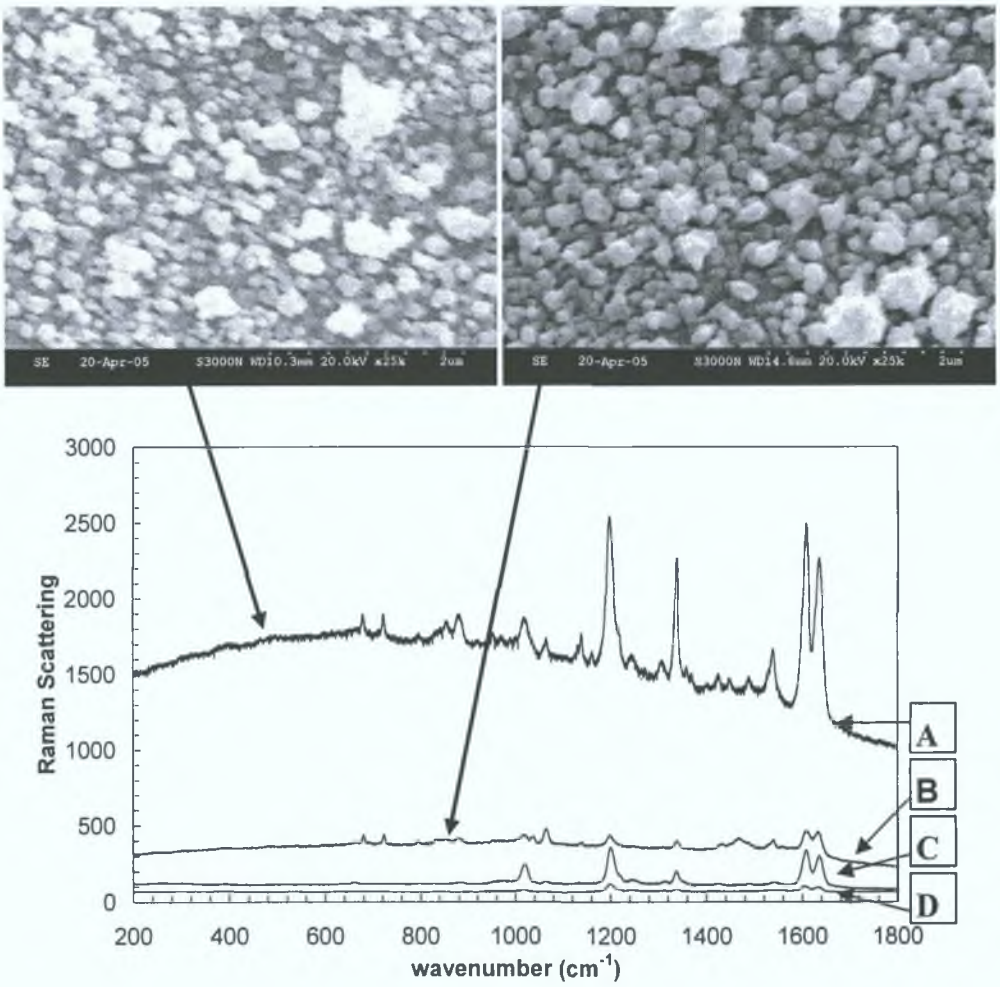

Fig. 3.22 SEM images (25k magnification) and SERS spectra of Gold electrodeposited on gold bead electrodes (A) from $NaAuCl_4$ + H_2SO_4 + KI at –0.4V 250mC cm^{-2} deposition, (B) from $NaAuCl_4$ + H_2SO_4 + KI at –0.4V 250mC cm^{-2} deposition. Compared against SERS spectrum of (C) roughened bead electrode and (D) smooth gold bead

The spectra obtained (Figure 3.22) yielded the same major bands as were found in the samples deposited with the additive KCl (1640cm^{-1}, 1600cm^{-1}, 1200cm^{-1}) however there were also some bands evident that were not seen in the previous samples, indicating that the samples may not have been sufficiently clean when immersed in the probe molecule, or that some component of the electrolyte solution was adsorbing or depositing on the surface. Qualitatively the spectra of the beads deposited from the same electrolytes have the same shape suggesting that the latter is more likely to be the case. The quality of the

baseline is significantly worse for the beads modified by electrodepositing gold from 0.01M $NaAuCl_4$ + 0.5M H_2SO_4 + 0.5mM KI. It is unclear what may have caused this, perhaps a longer electrochemical cleaning treatment needs to be applied to beads prepared in this manner.

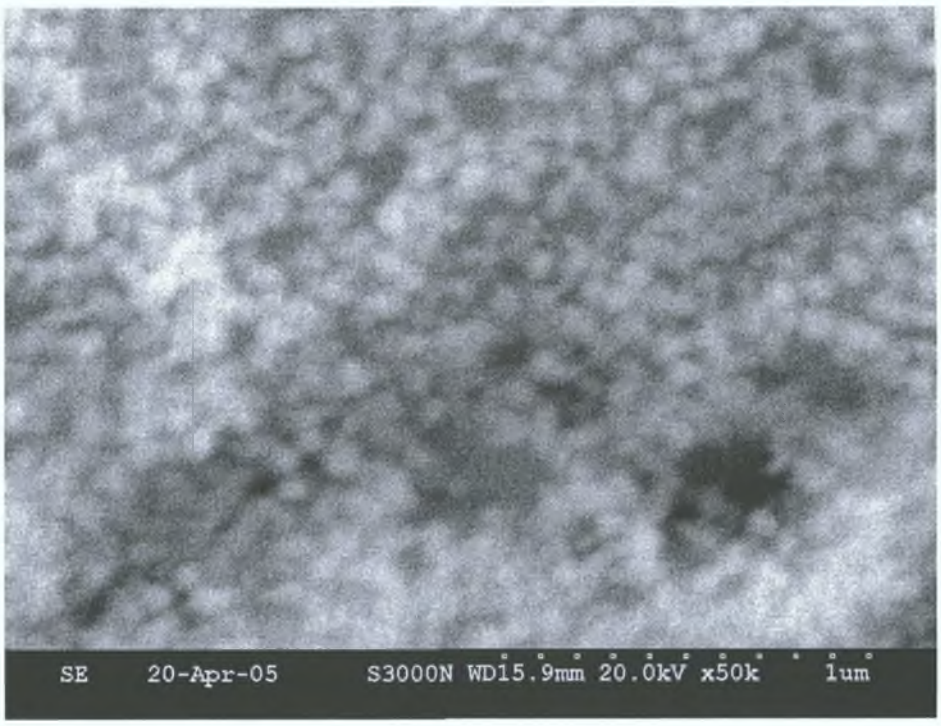

Fig. 3.23 SEM image of electrochemically roughened gold disk electrode (50k magnification)

The SEM images of the beads modified by electrodepositing gold from 0.01M $NaAuCl_4$ + 0.5M H_2SO_4 + 0.5mM KI (Figure 3.22) show again that the bead with lower particle size and higher particle density was the better SERS substrate. There was not an obvious difference in the depth of surface morphology of these samples as was seen in Figure 3.23 however this does not rule out this being an important factor. Comparing the SEM images of the two most successful bead SERS substrates (those modified with a deposition charge of 250mC cm^{-1}) when the additive was KCl (Figure 3.23) the particle size range[a] was 100nm-200nm yielding an enhancement factor of 54±1σ, while when the additive was KI (Figure 3.22) the particle size range was 125nm-250nm yielding an enhancement factor of 39±1σ. Comparing these results with the SEM image of the electrochemically roughened gold disk electrode (Figure 3.23) that had to be imaged at 50k magnification due to the small particle sizes the importance of particle

[a] determined by measuring the diameter of 20 randomly chosen particles from the SEM image

size of SERS enhancement is again clear With a particle size range of 40nm-80nm yielding an enhancement factor of 271±1σ it is clear that minimising the particle size of the gold bead electrodes is an important prerequisite to achieving strong SERS enhancements Of less importance it would seem is surface roughness, as the substrates with the greatest surface roughness were those with a deposition charge of 500mC cm^{2}, and these proved to give relatively poor SERS enhancements Importantly it has been demonstrated that nano-Au modified gold bead electrodes show SERS enhancements

Attempts to electrochemically roughen gold bead electrodes in the same manner as the mechanically polished gold disk electrode proved unsuccessful The bead did not turn dull brown in colour like the disk electrode had even after repeated attempts It is therefore likely that the electrochemical roughening procedure does not work very well on such a smooth surface This phenomenon might be rationalized with the fact that the spherical smooth surface of the beads is an extremely favourable morphology from a thermodynamic point of view and thus its electrochemical roughening is very difficult The gold disk electrode would have had many imperfections, scratches etc from the mechanical polishing process however the electrochemical polishing process would not cause this It seems likely that these imperfections are important for the electrochemical roughening to occur, possibly as initiation sites in the same way that electrodeposition occurs preferentially at imperfections on a smooth surface The gold bead on which roughening was attempted was analysed by Raman spectroscopy in the same way as the other samples however it yielded a poor SERS enhancement factor This indicated that although some roughening had occurred it was not very successful, and ways of introducing imperfections into the bead surface will have to be investigated if the roughening procedure is to prove successful in the future

Finally two nano-Au modified FTO substrates were analysed using Raman spectroscopy

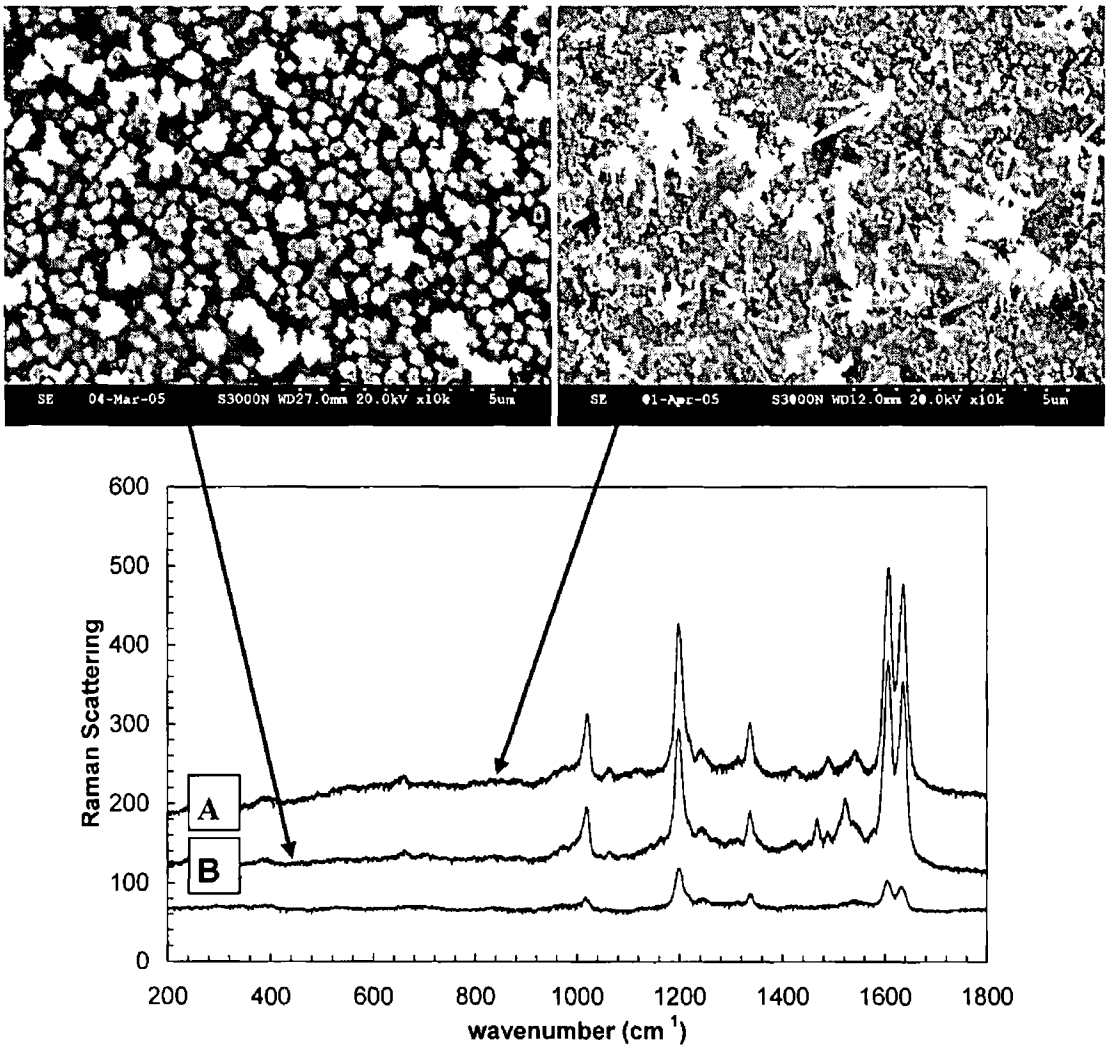

Fig 3 24 SEM images (10k magnification) and SERS spectra of FTO electrodes prepared (A) from $NaAuCl_4$ + H_2SO_4 + KI at –0 5V, 300 sec deposition, (B) from $NaAuCl_4$ + H_2SO_4 at –0 4V, 200 sec deposition Compared against SERS spectrum of smooth gold bead

The results of the analysis of the nano-Au modified FTO electrodes are presented in Figure 3 24 The enhancement factors of the substrates were 8±1σ when there was no additive in the deposition solution and 9±1σ when KI was the additive [d] The fact that these substrates yielded SERS enhancements proves that they have potential for use in this application and a more detailed investigation is required in order to establish if they have the potential to rival the gold bead and gold disk electrodes which have shown

[d] The enhancement factor was estimated by dividing the peak height (corrected for baseline) by the peak height of the untreated bead (corrected for baseline)

much better SERS enhancements From the SEM images in it is clear that these substrates are not densely packed, low particle size type-B films and therefore there is much scope for improvement of this method to yield substrates that could provide a better SERS enhancement None the less it has been proved in these experiments that nano-Au modified FTO electrodes show significant SERS enhancements

Table 3 25 Summary of SERS Enhancements

Substrate	**Treatment**	**Peak Height 1640cm^{-1}**	**Enhancement Factor[a]**
Bead	Untreated	27 5	1±1σ
Bead	Roughened	191	7±1σ
Bead 1	250mC cm^{2} Deposition from $NaAuCl_4$ +KCl	1496 8	54±1σ
Bead 2	500mC cm^{2} Deposition from $NaAuCl_4$ +KCl	411	15±1σ
Bead 3	500mC cm^{2} Deposition from $NaAuCl_4$ + $H2SO_4$ + KI	1059	39±1σ
Bead 4	250mC cm^{2} Deposition from $NaAuCl_4$ + $H2SO_4$ + KI	161	6±1σ
Disk	Roughened in KCl	7441	271±1σ
FTO 1	200s Deposition from $NaAuCl_4$ (No additive)	230	8±1σ
FTO 2	300s Deposition from $NaAuCl_4$ + KI	256	9±1σ

3.16 Optical characterisation

The transmittance of the nanoporous gold electrodes was measured using a Horiba Jobin-Yvon Uvisel spectroscopic ellipsometer. However, only the spectra of nanostructured gold obtained from 600 and 820 nm nanospheres were found to display definite peaks, while those belonging to 240 and 430 nm diameter nanocavities were completely unresolved. The reason for this anomaly is related to the size of the domains of 240 and 430 nm diameter nanostructured gold electrodes, which is much smaller with respect to 600 and 820 nm nanopores. The number of intrinsic defects increases with decreasing particle diameter. In the case of the smaller diameters, the microspot of the white-light laser beam of the ellipsometer irradiates more than one single domain. Therefore, the response results mediated on different domains with different packing (hcp or fcc) and is unresolved.

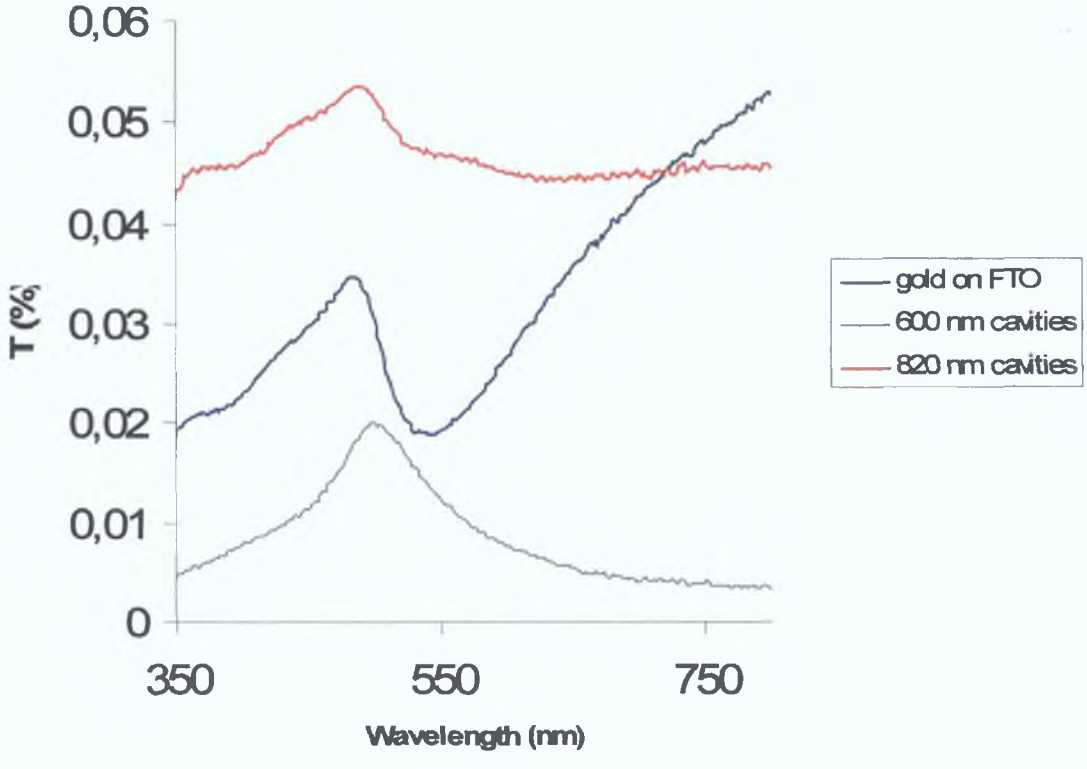

Fig. 3.26 Transmission spectra of nanoporous gold electrodes (600 and 820 nm cavity size) obtained using ellipsometry (microspot size=250μm^2)

The pore diameter affects the resonance peak position in the case of 820nm nanopores is slightly blue-shifted with respect to them band of 600 nm The position of the diffraction peaks is consistent with the Bragg's law and Snell's law, which can be employed to determine the transmission/reflection band gaps

3.17 Characterisation of gold nanoporous electrodes – surface area determination

The results are displayed in the following plot, in which the CVs of both nanoporous and bare gold electrodes are overlayed.

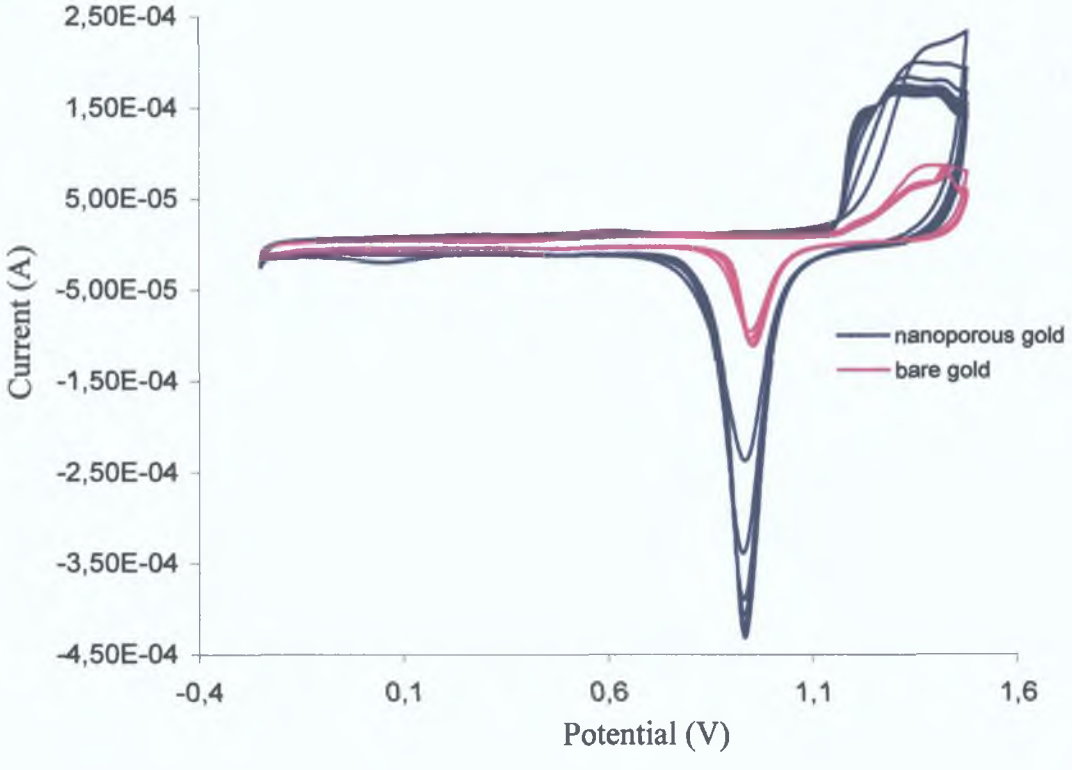

Fig. 3.27 Cyclic voltammograms of nanoporous and bare gold having the same geometric surface area in 0.5 H_2SO_4 vs Ag/AgCl; the ratio between the integrated reduction peaks of the nanoporous gold electrode and the bare gold is ~10^2 (the current decreases for 4 cycles due to impurities on the electrode surface and then is stable)

The real surface area of the nanoporous electrode can be estimated with respect to the real surface area of the bare gold (non-templated) by integrating the peak area corresponding to the reduction processes. The ratio between the integrated reduction peaks of the nanoporous gold electrode and the bare gold is ~10^2.

The surface area of the gold nanoporous electrodes is increased by two order of magnitude with respect to bare gold electrodes having the same geometric area the integration of the peak areas yielded an increase factor in the order of 10^2

3.18 Characterisation Using Scanning Electron Microscopy

In conclusion, the use of SEM has allowed to verify the morphology of the materials, both templated and not By comparing micrographs obtained by systematic variation of parameters to find out the best conditions for gold electrodeposition, especially in terms of choice of overpotential Furthermore, scanning electron microscopy has lead to discriminate among effects on nucleation and growth produced by different additives

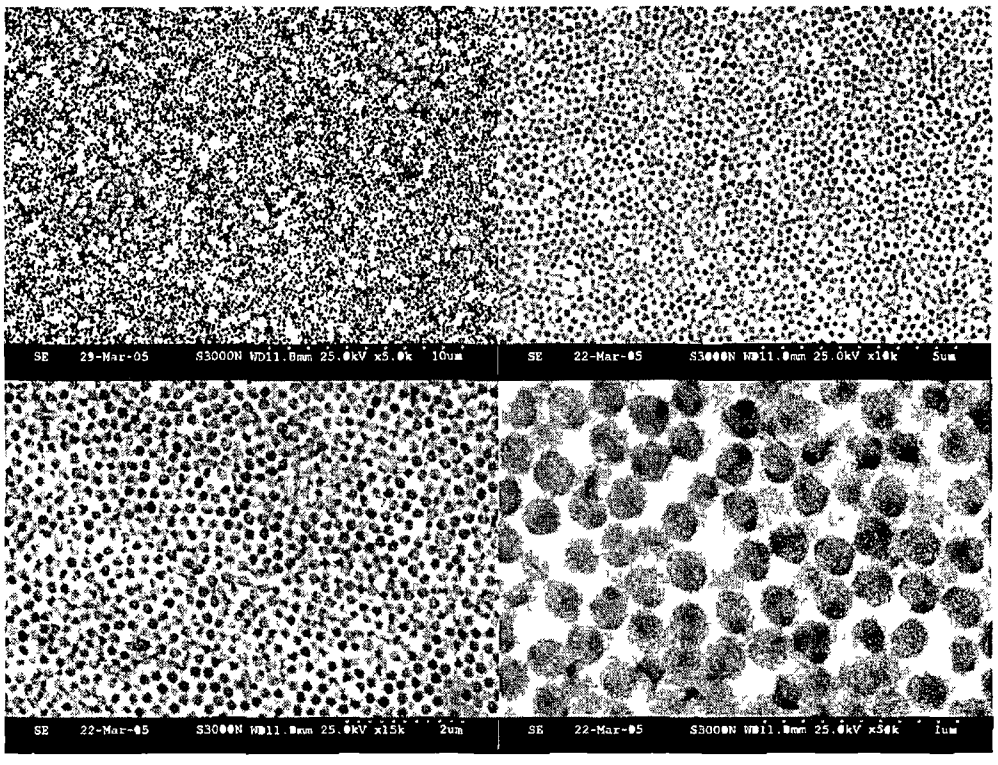

Fig 3 28 Micrographs of 240 nm gold porous electrodes at different magnifications (overpotential -1 0 V vs Ag/AgCl, electrodeposition time 50 s)

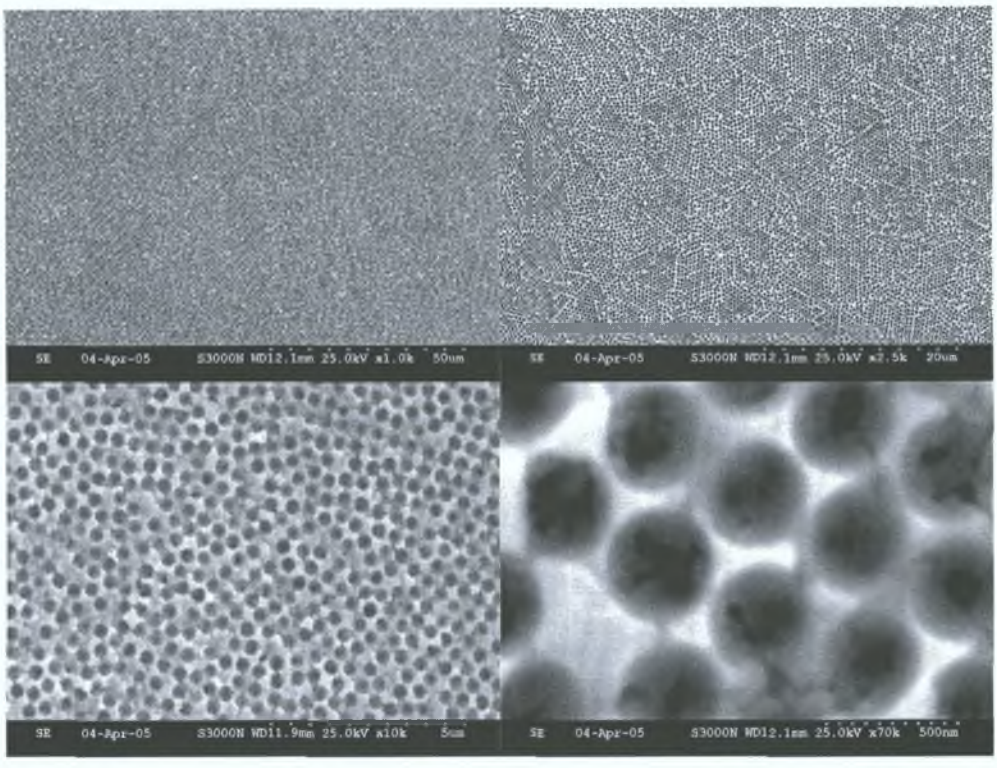

Fig. 3.29 Micrographs of 430 nm gold porous electrodes at different magnifications(overpotential: -1.0 V vs Ag/AgCl, electrodeposition time: 50 s)

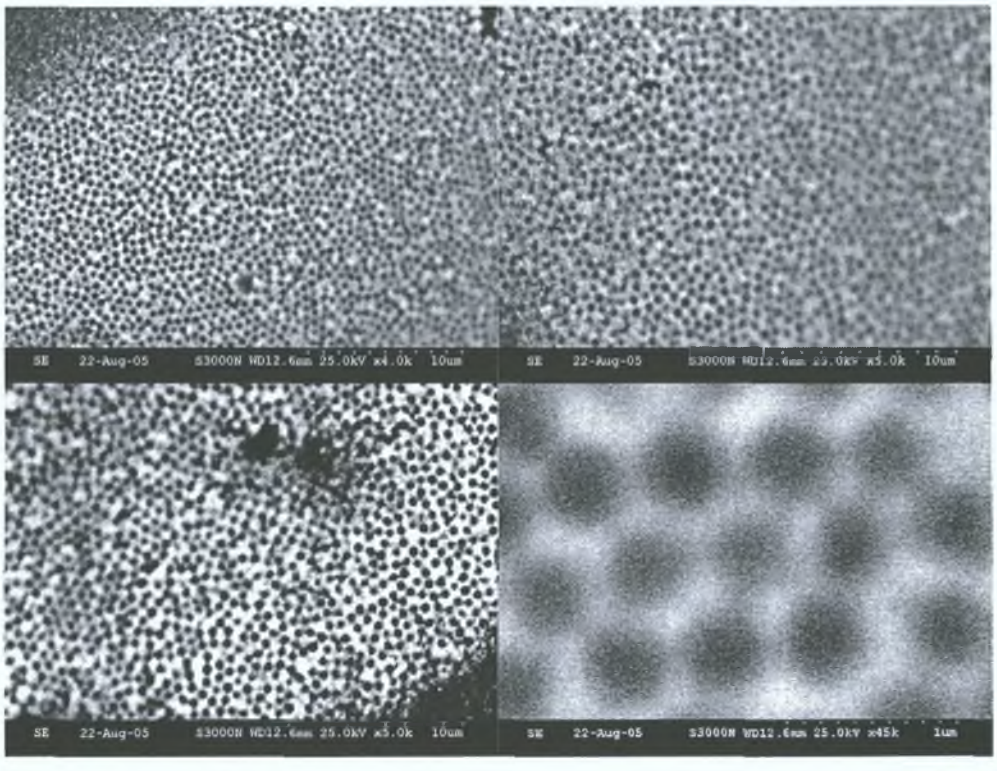

Fig. 3.30 Micrographs of 600 nm gold porous electrodes at different magnifications (overpotential: -1.0 V vs Ag/AgCl, electrodeposition time: 50 s)

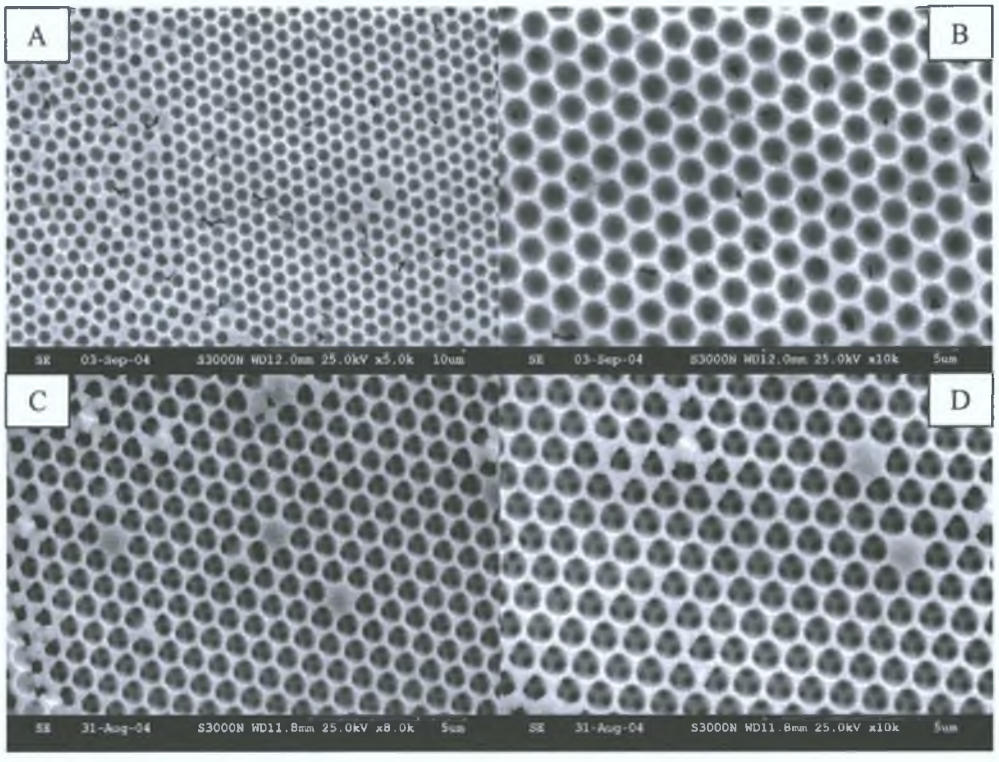

Fig. 3.31 Micrographs of 820 nm gold porous electrodes at different magnifications (A-B: monolayer, C-D: multilayer; overpotential: -1.0 V vs Ag/AgCl, electrodeposition time: 50 s (A-B) ,100 s (C-D))

3.19 Characterisation using Raman Spectroscopy

Gold nanopores[12] and spheroids [13-14] have been found to yield strong SERS effects using *trans*-1,2-two (4-pyridyl) ethylene (BPE) as test molecule.

Tessier et al.[12] (pores) and Felidj et al.[13-14] (spheroids) have observed a SERS effect for the molecule adsorbed on such arrays with a gain per molecule ranging from 10^4 to 10^5. Tessier et al. have utilized 630 nm nanospheres mixed together with concentrated gold nanoparticles (25 nm) and deposited on a microscope using a convective assembly process. The gold particles were trapped in the interstitial voids of the latex crystal and upon further evaporation assembled around the bottom latex layers. In the case the spheroids created by Felidj et al., the effect of the interparticle spacing and of the gold film thickness on Raman amplification was investigated at four excitation wavelengths (514, 633, 647, 674 nm). However, the method for creating nanostructures is

complicated and time-consuming while the approach used for fabricating spheroids requires an extremely expensive setup *On the contrary*, both techniques used in this project for producing the nanostructures, namely dip-coating and electrodeposition, are not time-consuming and do not need particularly expensive or complicated setup
The objectives of this project regarding SERS effects are

- testing the SERS response of gold nanostructures, reported by Tessier et al just for one cavity size and one excitation wavelength, to different pore sizes and wavelegths
- investigate the effect of gold film thickness (mono- and multilayer) on the enhancement intesity

Very recently Abdelsalam et al [15], using benzene thiol as test-molecule, have shown that structured gold surfaces formed by template electrodeposition can give strong surface enhanced Raman scattering, demonstrating the first use of these surfaces for in situ electrochemical SERS This enhancement is quite reproducible from place to place on the sample surface (unlike conventional roughened electrode surfaces) is stable and the surfaces can be cleaned and reused The order of magnitude of this enhancement is significantly weaker than that usually obtained on electrochemically roughened electrodes for which it can rise 10^7–10^8 the challenging problem of optimising the parameters for maximising the enhancement for these novel platforms (choice of the Raman-active biomolecule, radiation wavelength, nanopores size) is still far from being solved Raman spectroscopy has been used for studying SERS effects of molecules adsorbed on gold nanoporous electrodes with different cavity size (240, 430, 600, 820 nm), aiming to observe any variation in SERS signal intensities depending on the cavity size Preliminary investigation has lead to reasonably good results for nanostructures obtained from microsphers with 430 and 820 nm diameters (Figure 3 32)

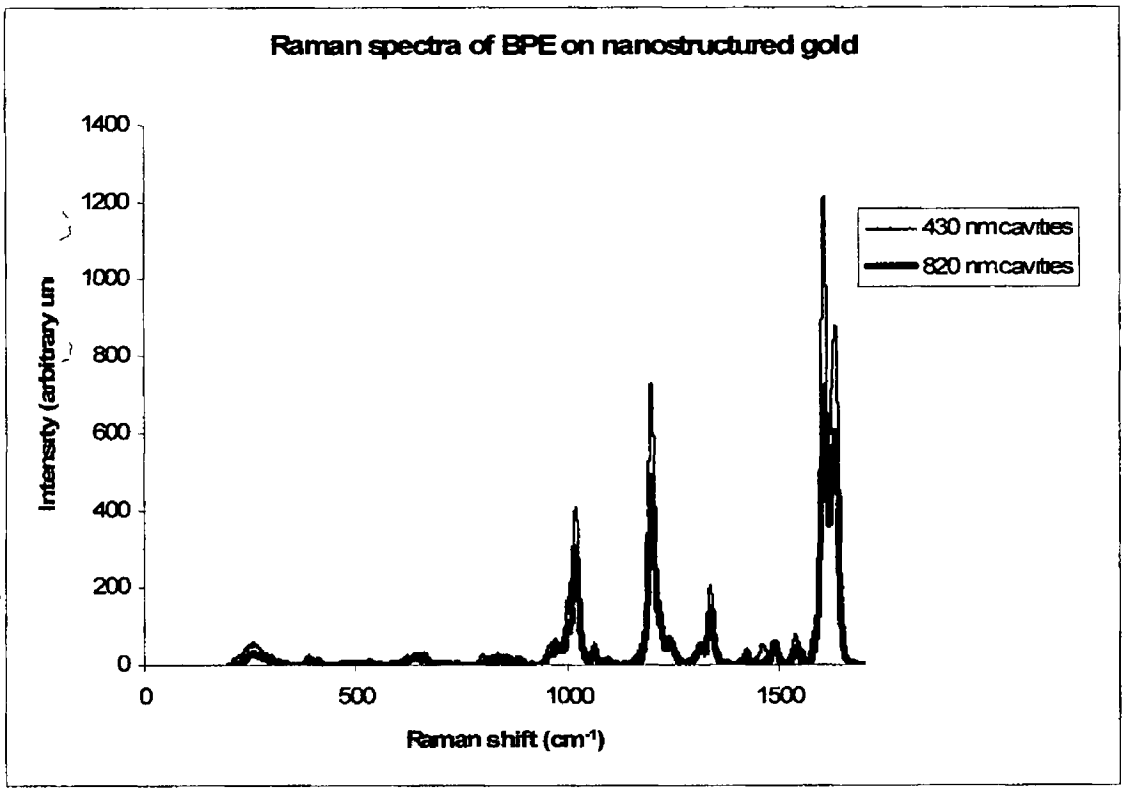

Fig. 3.32 Raman spectra of BPE on nanostructured gold (430 and 820 nm nanopores)

3.20 Conclusion

This work proves the usefulness of a "bottom-up" approach to produce nanoporous gold electrodes by self-assembling of colloidal nanospheres into closed-packed arrays, subsequently electrodepositing gold within the interstitial voids and removing the template

Electrochemical and photonic properties of these metal nanostructures have been investigated, demonstrating that structured gold surfaces formed by template electrodeposition can give strong surface enhanced Raman scattering This enhancement is reproducible from place to place on the sample surface, is stable and the surfaces can be cleaned and reused

The final material, a photonic crystal with an inverse opal morphology, is a potentially useful substrate since, thanks to the possibility to confine surface plasmons in its cavities, it could be used as platform for biodiagnostics (e g single molecule detection) as well as for electrocatalytic processes

3.21 Future work

A few challenging aims of future work could be

1 identify a suitable protocol to avoid the polystyrene beads re-suspension phenomenon, finding for instance a more effective method to etch the FTO glass substrates The choice of this protocol is essential, since the physico-chemical properties of FTO layer could be strongly and irreversibly altered by a too aggressive chemical treatment
2 test different Raman-active molecules with all nanopore sizes in order to observe stronger SERS intensities (10^7-10^8)
3 extend the creation of nanoporous electrodes to other metals

REFERENCES

[1] Chung, Y W Leub, I C Leea, J H Hon, M H *Journal of Crystal Growth* **2005**, *275*, e2389

[2] Fleischmann, M Hendra, P J Mcquillan, A J *Chem Phys Lett* **1974**, *16*, 163

[3] Jeanmarie, D L Van Duyne, R P *J Electroanal Chem* **1977**, *84*, 1

[4] Liu, S Li, J and Jiang, L *Colloids And Surfaces A-Physicochemical And Engineering Aspects*, **2005**, *257*, 57

[5] Pasquato, L Pengo, P Scrimin, P *Journal Of Materials Chemistry*, **2004** , *14*, 3481

[6] Scharifker, B Hills, G *Electrochim Acta* **1983**, *28*, 879

[7] Kalyuzhny, G Vaskevich, A Schnewweiss, M and Rubinstein, I *Chemistry A European Journal*, **2002**, *8*, 3849

[8] Schwartzberg, A Grant, C Wolcott, A Talley, C Huser, T Bogomolni, R Zhang, J *Journal of Physical Chemistry B* **2004**, *108*, 19191

[9] El-Deab, M Sotomura, T and Ohsaka, T *Journal of the Electrochemical society* **2005**, *152* (1), c1

[10] Sauer, G Brehm, G Schneider, S *Journal of Raman Spectroscopy*, **2004**, *35*, 568

[11] Stolberg, L Lipkowski, J and Irish, D *Journal Of Electroanalytical Chemistry* **1991**, *300*, 563

[12] Tessier, P M Velev, O D Kalambur, A T Rabolt, J F Lenhoff, A M Kaler E W *J Am Chem Soc* **2000**, *122*, 9554

[13] Felidj, N Aubard, J Levi, G Krenn, J R Schider, G Leitner, A and Aussenegg, F R *Phys Rev B* **2002**, *66*, 245407

[14] Felidj, N Aubard, J Levi, G Krenn, J R Hohenau, A Schider, G Leitner, A Aussenegg, F R *Appl Phys Lett* **2003**, *82*, 3095

[15] Abdelsalam , M E Bartlett, P N Baumberg , J J Cintra, S Kelf , T A Russell A E *Electrochemistry Communications* **2005**, *7*, 740